

**PROBING THE EARLY STEPS IN THE CATALYTIC REDUCTION OF  
NITRITE TO AMMONIA, CATALYZED BY CYTOCHROME C NITRITE  
REDUCTASE**

by

Mahbbat Ali

A Dissertation Submitted in  
Partial Fulfilment of the  
Requirement for the Degree of

Doctor of Philosophy  
in Chemistry

at

The University of Wisconsin-Milwaukee

December 2019

## ABSTRACT

# PROBING THE EARLY STEPS IN THE CATALYTIC REDUCTION OF NITRITE TO AMMONIA, CATALYZED BY CYTOCHROME *c* NITRITE REDUCTASE

by

Mahbbat Ali

The University of Wisconsin-Milwaukee, 2019  
Under the Supervision of Professor A. Andrew Pacheco

Cytochrome *c* Nitrite Reductase (ccNiR) is a periplasmic, decaheme homodimeric enzyme that catalyzes the six-electron reduction of nitrite to ammonia. Under standard assay conditions catalysis proceeds without detected intermediates, and it's been assumed that this is also true in vivo. However, this report demonstrates that in vitro it's possible to trap putative intermediates by controlling the electrochemical potential at which reduction takes place. Such experiments provide valuable insights regarding ccNiR-catalyzed nitrite ammonification.

UV/Vis spectropotentiometry showed that nitrite-loaded *Shewanella oneidensis* ccNiR is reduced in a concerted 2-electron step to generate an {FeNO}<sup>7</sup> moiety at the active site, with an associated midpoint potential of +246 mV vs SHE at pH 7. By contrast, cyanide-bound active site reduction is a one-electron process with a midpoint potential of 20 mV, and without a strong-field ligand the active site midpoint potential shifts 70 mV lower still. EPR analysis subsequently revealed that the {FeNO}<sup>7</sup> moiety possesses an unusual spectral signature, different from those normally observed for {FeNO}<sup>7</sup> hemes, that may indicate magnetic interaction of the active site with nearby hemes. Protein film voltammetry experiments previously showed that catalytic nitrite reduction to ammonia by *S. oneidensis* ccNiR requires an applied potential of at least -120 mV, well below

the midpoint potential for  $\{\text{FeNO}\}^7$  formation. Thus, it appears that an  $\{\text{FeNO}\}^7$  active site is a catalytic intermediate in the ccNiR-mediated reduction of nitrite to ammonia, whose degree of accumulation depends exclusively on the applied potential. At low potentials the species is rapidly reduced and doesn't accumulate, while at higher potentials it is trapped, thus preventing catalytic ammonia formation.

When the weak reductant ferrocyanide is used as the electron source, *S. oneidensis* ccNiR catalyzes the one-electron reduction of nitrite to nitric oxide. The reaction rate has hyperbolic dependence on nitrite concentration and linear dependence on ccNiR concentration.  $\text{NO}\cdot$  release is minimal compared to the rate of ammonia formation at lower applied potentials. Kinetic studies also show that the rate of  $\text{NO}\cdot$  production is pH-dependent, and that an amino acid with  $\text{pK}_a$  of 6.9, probably His268, needs to be protonated for the enzyme to be active.

# TABLE OF CONTENTS

CHAPTERS	PAGE NUMBER
1. Introduction	
1.1. Overview of nitrogen cycle.....	1
1.2. Ecological importance of reactive nitrogen balance.....	9
1.3. Overview of ccNiR.....	11
1.4. Nitric oxide in biology.....	15
1.4.1. Overview of free nitric oxide and its role in biology.....	16
1.4.2. Heme and non-heme nitrosyl complexes.....	19
1.5. References.....	22
2. Trapping of a putative intermediate in the cytochrome <i>c</i> nitrite reductase (ccNiR)-catalyzed reduction of nitrite: implications for the ccNiR reaction mechanism	
2.1. Overview.....	30
2.2. Experimental procedures.....	30
2.2.1. General materials.....	30
2.2.2. Protein purification and handling.....	31
2.2.3. General instrumentation.....	31
2.2.4. UV/Visible spectropotentiometric titrations of ccNiR.....	31
2.2.5. Time-resolved reduction of nitrite-loaded ccNiR by <i>N,N,N',N'</i> tetramethyl- <i>p</i> -phenylenediamine.....	32
2.2.6. Electron paramagnetic resonance (EPR) analysis of ccNiR.....	32

2.3. Results.....	34
2.3.1. Effect of nitrite on the electrochemical properties of <i>S. oneidensis</i> ccNiR.....	34
2.3.2. Reduction of nitrite-loaded <i>S. oneidensis</i> ccNiR by <i>N,N,N',N'</i> tetramethyl- <i>p</i> -phenylenediamine.....	40
2.3.3. Investigation of the <i>S. oneidensis</i> ccNiR {Fe <sub>H</sub> NO} <sup>7</sup> moiety by EPR spectroscopy.....	44
2.4. Discussion.....	47
2.4.1. Behavior of the nitrite-loaded ccNiR under weakly reducing condition.....	47
2.4.2. Implication of the results for the ccNiR reaction mechanism.....	50
2.4.3. Summary.....	55
2.5. References.....	57
3. A mechanistic study of ccNiR-catalyzed reduction of nitrite by ferrocyanide	
3.1. Overview.....	63
3.2. Experimental procedures.....	63
3.2.1. General materials.....	63
3.2.2. Catalase purification and handling.....	64
3.2.3. Buffer and stock solution preparation.....	64
3.2.4. Data collection.....	65
3.3. Results.....	66
3.3.1. NO· trapping experiments.....	66
3.3.2. Detection of ferrocyanide oxidation at higher ccNiR concentration.....	75
3.4. Discussion.....	80

3.5. References.....	82
4. Determination of the equilibrium constant for methyl viologen monocation radical dimerization	
4.1. Overview.....	83
4.2. Experimental methods.....	84
4.2.1. General materials and instrumentation.....	84
4.2.2. Data collection and processing.....	84
4.2.3. Equilibrium expression derivation.....	85
4.3. Results.....	86
4.3.1. Spectral changes as a function of $C_T$ .....	86
4.3.2. Extraction of $K_{eq}$ and of the extinction coefficient spectra for reduced methyl viologen monomer and dimer from the matrix of reduced spectra.....	89
4.4. Discussion.....	94
4.5. References.....	97
Appendices	
Appendix A: Supplementary materials for chapter 2.....	98
A.1. Verification of ccNiR purity by SDS-PAGE.....	98
A.2. Mediators used for spectropotentiometric experiments.....	98
A.3. Equilibrium expression for nitrite binding to the ccNiR active site.....	102
A.4. Dependence of nitrite-loaded ccNiR's electrochemical behavior on pH and nitrite concentration.....	103

A.5. Spin quantitation of the nitrite-loaded ccNiR EPR spectrum after reduction.....	107
A.6. Quantitation of adventitious iron in the EPR spectra.....	108
A.7. Absorbance changes upon reduction of nitrite-loaded ccNiR.....	109
A.8. References.....	110
Appendix B: Supplementary materials for chapter 3.....	111
B.1. Absorbance changes upon releasing of nitric oxide (NO·) from the reduction of nitrite.....	111
Appendix C: Supplementary materials for chapter 4.....	112
C.1. UV/Vis spectropotentiometric studies of methyl viologen (MV) monomer-dimer equilibrium.....	112
Curriculum Vitae.....	113

## LIST OF FIGURES

**Figure 1.1.** The nitrogen cycle, showing the five major pathways, and one minor pathway. Orange: nitrogen fixation; Red: nitrification; Purple: nitrate ammonification (nitrate to ammonia), and denitrification (nitrate to dinitrogen); Blue: the anammox process, comproportionation of ammonia and NO<sup>•</sup>; Green: comproportionation of hydroxylamine and NO<sup>•</sup>, a minor process that has been observed in some bacteria and fungi. The enzymes associated with each step are shown next to the corresponding arrows.....2

**Figure 1.2.** (a) Heme arrangement within the ccNiR dimer, showing the possible paths of electron flow. (b) Five hemes, and their associated axial ligands, from one of the *Shewanella oneidensis* ccNiR protomers (from the Protein Data Bank, accession number 3UBR; the heme arrangement is virtually identical in ccNiR from other organisms). The *S. oneidensis* heme midpoint potentials previously obtained in the presence of the strong-field (SF) ligand cyanide are shown in red, while those obtained in the presence of only weak-field (WF) ligands such as water are shown in blue (ref.). The dashed vertical line represents the dimer interface.....12

**Figure 1.3.** Active site region of *S. oneidensis* ccNiR. The figure shows the active site heme 1, its unusual proximal ligand Lys123, three conserved active site residues proposed to be catalytically important, the water coordinated to the distal site of heme a in the resting enzyme, and a water that hydrogen bonds to Lys123. The blue structure was obtained at 110K (PDB 6P73, 1.66 Å resolution), while the orange structure was obtained at room temperature using the Laue method (PDB 3UBR, 2.59 Å resolution).....13

**Figure 1.4.** Molecular orbital diagram for NO<sup>•</sup>. Oxidation of the neutral molecule removes a  $\pi$ -antibonding electron thus increasing the bond order, whereas reduction adds a  $\pi$ -antibonding electron, making a di radical and decreasing the bond order.....17

**Figure 2.1.** (a) UV/Vis spectral changes obtained upon exposing a solution initially containing 76  $\mu$ M of fully oxidized ccNiR, 100  $\mu$ M 1, 2-naphthoquinone-4-sulfonic acid and 5 mM nitrite to progressively lower potentials. Solid blue lines show the experimentally obtained data, whereas the dashed red lines were calculated from least-squares fitting with a Nernstian 2-electron reduction and one spectral component (Scheme 2.1 and Appendix A). The fit yields a midpoint potential of  $\varepsilon_m^o = 0.246$  V. (b) Blue circles: an absorbance difference vs. applied potential slice taken at 424 nm from the spectra of part (a); solid red line: least-squares best fit obtained from global analysis of the data with  $n$  fixed at 2 electrons transferred in the Nernstian equation; dotted green line: same as the red line, but with  $n$  fixed at 1 electron transferred in the Nernstian equation.....36

**Figure 2.2.** Blue circles: dependence on nitrite concentration of the apparent midpoint potential obtained by fitting UV/Vis spectropotentiometric data to the empirical Nernst equation (Scheme 2.1, Eq. 2.1). Red squares, green triangles and purple diamonds: predicted values of the apparent midpoint potential at a given nitrite concentration, calculated as described in Appendix A, using

$\varepsilon^{\circ} = 0.246 \text{ V}$ ; the red square values were obtained by varying  $K$  to yield the least-squares best fit ( $K = 2600 \text{ M}^{-1}$ ), while the green triangle values were obtained with  $K$  fixed at  $5000 \text{ M}^{-1}$ , and the purple diamond values with  $K$  fixed at  $1400 \text{ M}^{-1}$  (see text for details).....39

**Figure 2.3.** (a) Blue traces: spectral changes seen at 120 s intervals after mixing 11  $\mu\text{M}$  oxidized ccNiR with 1 mM each of nitrite and TMPD. Red dashed traces: least-squares best fits using Eq. 2.2. Green trace: spectrum of the solution containing 11  $\mu\text{M}$  oxidized ccNiR and 1 mM TMPD, but prior to addition of nitrite; purple dashed trace: least-squares best fit obtained with the independently known oxidized ccNiR extinction coefficient spectrum. (b) Absorbance vs. time slice from the Fig. 2.3a spectrum, obtained at 611 nm.....41

**Figure 2.4.** Spectral components  $\Lambda_0$ (a) and  $\Lambda_1$ (b) generated by fitting the SVD-processed Fig.2.3 data to Eq. 2.2 (blue traces).  $\Lambda_0$  was in turn fit with the extinction coefficient spectra of reduced nitrite-loaded ccNiR (obtained as described in Appendix A), and of the blue  $\text{TMPD}^+$  radical, while  $\Lambda_1$  was fit using only the  $\text{TMPD}^+$  extinction coefficient spectrum. The red dashed traces show the calculated spectra in each case.....43

**Figure 2.5.** Green trace: X-band EPR spectrum obtained for fully oxidized ccNiR in the presence of 5 mM nitrite. Blue trace: spectrum obtained for a solution initially containing 64 $\mu\text{M}$  of fully oxidized ccNiR and 500  $\mu\text{M}$   $^{14}\text{NO}_2^-$ , after exposing it to an applied potential of 160 mV vs SHE. Red trace: same as blue trace, but using 500  $\mu\text{M}$   $^{15}\text{NO}_2^-$ .....45

**Figure 2.6.** Cartoon representation of the ccNiR-catalyzed nitrite reduction reaction path, proposed on the basis of the results reported herein. The standard free energies are per mole of product formed, and where applicable, are calculated relative to the standard hydrogen electrode. The question mark denotes an as-yet uncharacterized putative 4-electron reduced intermediate, for which there is some preliminary evidence. We propose that weak reductants can't provide the overpotential necessary to overcome the depicted high activation barrier, thus allowing intermediates to accumulate. Only when a strong reductant such as methyl viologen monocation radical is used does nitrite get reduced directly to ammonia, without accumulation of detectable intermediates.....54

**Figure 3.1.** (a) Blue traces: spectral changes observed at 500 s intervals in a pH 7.0 solution initially containing 75 nM ccNiR, 4  $\mu\text{M}$  catalase, 2 mM nitrite and 20 mM ferrocyanide. Dashed red traces: least-squares best fits obtained using Eq. 3.1. (b) Absorbance vs time slice from the spectra in (a), obtained at 433 nm.....67

**Figure 3.2.** Spectral component  $\Lambda$  generated by fitting the SVD-processed Fig. 3.1 data to Eq. 3.1 (blue trace).  $\Lambda$  was in turn fit with the extinction coefficient difference spectrum  $\Delta\epsilon_{\text{CatNO}} = \epsilon_{\text{CatNO}} - \epsilon_{\text{Cat}}$ , where  $\epsilon_{\text{Cat}}$  and  $\epsilon_{\text{CatNO}}$  are the independently known extinction coefficient spectra for catalase and nitrosylated catalase, respectively.....68

**Figure 3.3.** Initial rate of NO· release is directly proportional to the concentration of ccNiR. Small blue circles are the experimentally observed initial rates at the corresponding ccNiR concentration. The red line is the linear least-squares best fit to the data. This data set was collected at pH 7.0, with a nitrite concentration of 2 mM, a ferrocyanide concentration of 20 mM and a catalase concentration 4 μM. The slope of the line gives an apparent second-order rate constant,  $k_{app} = (2.0 \pm 0.1) \times 10^4 \text{ M}^{-1} \text{ s}^{-1}$ . The intercept of  $(1.2 \pm 0.7) \times 10^{-4} \text{ s}^{-1}$  indicates that some NO· was generated without any ccNiR.....70

**Figure 3.4.** Dependence on pH of the parameter  $k_{app}$  obtained from (initial rate/free catalase) vs [ccNiR] plots (e.g. Fig 3.3). For all the experiments nitrite, ferrocyanide and catalase were held constant at 2 mM, 20 mM and 4 μM, respectively. Blue circles: experimentally obtained values at each pH; red line: least-squares best fit to the sigmoidal equation 3.3. The fit yielded a  $pK_a$  value of  $6.9 \pm 0.1$ .....71

**Figure 3.5.** Dependence of initial rate of NO· release on nitrite concentration. Blue circles are the experimentally obtained values at each nitrite concentration, while the red curve is the least-squares fit of the data to the rectangular hyperbola, Eq. 3.4. This set of experiments was performed at pH 7.0 in the presence of 100 nM ccNiR, 4 μM catalase, 10 mM ferrocyanide and varying nitrite concentration. The least-squares fit yielded the parameter values  $K_{m1} = (4.5 \pm 0.9) \times 10^{-4} \text{ M}$  and  $M_1 = (2.0 \pm 0.1) \times 10^{-3} \text{ s}^{-1}$ .....72

**Figure 3.6.** Dependence of initial rate of NO· release on ferrocyanide concentration. Blue circles are the experimentally obtained values at each ferrocyanide concentration, while the red curve is the least-squares fit of the data to the rectangular hyperbola, Eq. 3.5. This set of experiments was performed at pH 7.0 in the presence of 100 nM ccNiR, 4 μM catalase, 8 mM nitrite and varying ferrocyanide concentration. The least-squares fit yielded the parameter values  $K_{m2} = (7 \pm 2) \times 10^{-4} \text{ M}$  and  $M_2 = (1.9 \pm 0.1) \times 10^{-3} \text{ s}^{-1}$ .....74

**Figure 3.7.** Effect of varying ammonium sulfate concentrations on ccNiR-catalyzed reduction of nitrite to nitric oxide by ferrocyanide. The concentrations of ccNiR, catalase and ferrocyanide were 100 nM, 4 μM and 20 mM, respectively in all experiments. Symbols: experimentally derived initial rate values; lines: least-squares fits to rectangular hyperbolas of initial rate vs  $[\text{NO}_2^-]$  plots for the varying ammonium sulfate concentrations.....74

**Figure 3.8.** Blue traces: SVD-treated spectral changes observed at selected time intervals over the course of one hour in a pH 7.0 solution initially containing 1 μM ccNiR, 8 mM nitrite and 20 mM ferrocyanide. Red traces: least-squares best fit to Eq. 3.6. The first six spectra are at 60 s intervals starting at 60 s, the next two are at 360 s intervals, and the final two at 1000 s intervals.....76

**Figure 3.9.** Spectral components (a)  $\Lambda_1$  and (b)  $\Lambda_2$  generated by fitting the SVD-processed Fig. 3.8 data to Eq. 3.6 (blue traces). The two components were in turn fit with the independently obtained extinction coefficient spectra for  $\Delta \epsilon_{ccNiR} = \epsilon(\{\text{Fe}_{HI}\text{NO}\}^7) - \epsilon[\text{Fe}_{HI}^{\text{III}}(\text{NO}_2^-)]$  and for ferricyanide (spectral changes due to ferrocyanide were negligible in the region analyzed). The

insets show that the first component grows in exponentially over approximately 10 minutes, whereas the second increases linearly with time; roughly 12  $\mu\text{M}$  ferricyanide and an equivalent amount of  $\text{NO}\cdot$  are generated over the course of one hour, and the ccNiR is completely reduced to the  $\{\text{Fe}_{\text{HI}}\text{NO}\}^7$  form.....78

**Figure 3.10.** Dependence of initial rate of ferrocyanide oxidation, adjusted for ccNiR concentration, on ferrocyanide concentration. Blue circles are the experimentally obtained values at each ferrocyanide concentration, while the red curve is the least-squares fit of the data to the rectangular hyperbola Eq. 3.7. This set of experiments was performed at pH 7.0 in the presence of approximately 0.8  $\mu\text{M}$  ccNiR, 8 mM nitrite and varying ferrocyanide concentration. The least-squares fit yielded the parameter values  $K_{m3} = (7 \pm 3) \times 10^{-4} \text{ M}$  and  $k_{cat} = (2.7 \pm 0.3) \times 10^{-3} \text{ s}^{-1}$  .....80

**Figure 4.1.** Example of an  $\text{MV}_{\text{ox}}$  spectrum fit, using the independently obtained extinction coefficient spectrum to calculate the  $\text{MV}_{\text{ox}}$  concentration. For this sample the  $\text{MV}_{\text{ox}}$  concentration was determined to be 1.21 mM. Oxidized methyl viologen has no absorbance above 350 nm.....87

**Figure 4.2.** (a) UV/Vis spectrum of the methyl viologen sample from Fig. 4.1 after complete reduction at an applied potential of  $-603 \text{ mV vs SHE}$ . (b) Apparent extinction coefficient spectrum calculated by dividing spectrum 4.2a by the total methyl viologen concentration obtained from analysis of the oxidized spectrum (Fig. 4.1).....88

**Figure 4.3.** Apparent extinction coefficient spectra obtained at varying concentrations of total reduced methyl viologen,  $C_T$ . The arrows show how key features change as  $C_T$  increases. The data set was first subjected to singular value decomposition (SVD) to reduce noise. The SVD process also verified that only two spectral components contribute the collection of spectra, presumably those of the monomer and dimer.....89

**Figure 4.4.** Extinction coefficient spectra for the reduced methyl viologen monomer and dimer species, as calculated by least-squares fit of the Fig. 4.3 data set with Eq. 4.6.....92

**Figure 4.5.** (a) Least-squares fit of the SVD-processed apparent extinction coefficient spectra of reduced methyl viologen at varying  $C_T$ . (b) Change in apparent extinction coefficient with  $C_T$  at 600 nm.....93

**Figure 4.6.** (a) Typical results of a ccNiR assay analyzed using the extinction coefficient spectra of Fig. 4.4. The spectral changes with time were monitored in the range from 540 nm to 700 nm as reduced methyl viologen reacted with nitrite; the calculated values of  $C_{\text{mono}}$ ,  $C_{\text{dim}}$  and  $C_T$  are shown. (b) Linear least-squares fit of the  $C_T$  vs time curve.....95

**Figure A.1.** Typical SDS-PAGE for pure ccNiR samples used in the experiments described herein.....98

**Figure A.2.** (a) Extinction coefficient difference spectrum for reduced – oxidized *N,N,N',N'*-tetramethyl-*p*-phenylenediamine ( $\Delta$ TMPD; only the oxidized form absorbs in the region from 350 nm – 800 nm) . (b)Spectral contribution expected from 25  $\mu$ M  $\Delta$ TMPD, contained in a 0.02 cm pathlength cuvette.....100

**Figure A.3.** (a) Extinction coefficient difference spectrum for reduced – oxidized 1,2-naphthoquinone – 2-sulfonic acid ( $\Delta$ NPSA; only the oxidized form absorbs in the region from 350 nm – 500 nm, neither form absorbs above 500 nm). (b) Spectral contribution expected from 100  $\mu$ M  $\Delta$ NPSA, contained in a 0.02 cm pathlength cuvette.....100

**Figure A.4.** (a) Extinction coefficient difference spectrum for reduced – oxidized Phenazine methosulfate ( $\Delta$ PMS; only the oxidized form absorbs in the region from 350 nm – 500 nm, and neither form absorbs above 500 nm). (b) Spectral contribution expected from 25  $\mu$ M  $\Delta$ PMS, contained in a 0.02 cm pathlength cuvette.....101

**Figure A.5.** Extinction coefficient difference spectra obtained by fitting data collected in the presence of 5 mM (blue trace) and 20 mM (green trace) to Eq. A12. The red trace is the average of the other two, and was used to determine the extent of ccNiR reduction in experiments where this was not known apriori.....104

**Figure A.6.** Red trace: extinction coefficient spectrum of  $\{Fe_{HI}NO\}^7$  ccNiR. Blue trace: spectrum of fully oxidized ccNiR.....104

**Figure A.7.** Blue trace: plot of  $\{Fe_{HI}NO\}^7$  vs  $\epsilon_{app}$  calculated using Eqs A18 and A19, when  $Fe_T$  and  $N_T$  are both 70  $\mu$ M. The midpoint potential is taken as the value of  $\epsilon_{app}$  at which 50% of  $Fe_T$  has been reduced. Red trace: plot obtained with  $N_T = 5$  mM, when virtually all ccNiR is nitrite-loaded.....106

**Figure A.8.** (a) Solid blue trace: X-band EPR spectrum of the nitrite-loaded ccNiR solution from Fig. 8 after reduction at  $\epsilon_{app} = 160$  mV vs SHE; dashed red trace: simulated spectrum of the rhombic signal arising from ccNiR heme 2; purple trace: simulation of the  $S = 3/2$   $\{FeNO\}^7$  signal. (b) Integration of the signals from (a). (c) Double integration.....107

**Figure A.9.** Blue trace: X-band EPR spectrum of the nitrite-loaded ccNiR solution from Fig. 8 after reduction at  $\epsilon_{app} = 160$  mV vs SHE; Red trace: filtrate from ultrafiltration of a solution that initially contained the same species as those of Fig. 8, plus 25  $\mu$ M  $Cu^{2+}$ , after adding approximately 60  $\mu$ M  $NO\cdot$ , and subjecting it to an applied potential of 160 mV vs SHE.....108

**Figure A.10.** Blue trace: filtrate from ultrafiltration of a solution that initially contained the same components as those of Fig. 8, plus 25  $\mu$ M  $Cu^{2+}$ , after adding approximately 60  $\mu$ M  $NO\cdot$ , but before subjecting to a reducing potential. Red trace: same as red trace in Fig. A11.....108

**Figure A.11.** UV/Vis spectra obtained upon exposing a solution initially containing 76  $\mu\text{M}$  of fully oxidized ccNiR, 100  $\mu\text{M}$  1,2-naphthoquinone-4-sulfonic acid and 5 mM nitrite to progressively lower potentials.....109

**Figure B.1.** UV/Vis spectral changes obtained from  $\text{NO}\cdot$  binding with catalase. A solution containing 75 nM ccNiR, 20 mM ferrocyanide, 2 mM nitrite and 4  $\mu\text{M}$  catalase at pH 7.0 was taken to run the steady state reaction for 1 hour. ccNiR catalyzed the reduction of nitrite by 1-electron to  $\text{NO}\cdot$  by the weak reducing agent ferrocyanide.....111

**Figure C.1.** The spectral change obtained when  $\text{MV}_{\text{ox}}$  was reduced to  $\text{MV}_{\text{red}}$  by applying progressively lower potential.....112

## LIST OF TABLES

<b>Table 1.1.</b> A representation of prokaryotes that are known to carry out nitrogen-fixation....	3
<b>Table 1.2.</b> Variations in N-O bond length and stretching frequency in NO <sup>n</sup> species.....	18
<b>Table A.1.</b> Mediators used for spectropotentiometry.....	98

## LIST OF SCHEMES

- Scheme 1.1.** The half reaction for nitrogen fixation. The overall reaction is catalyzed by nitrogenase (NiF in Fig. 1.1).....3
- Scheme 1.2.** The half reactions for nitrification. The first step is catalyzed by the enzyme ammonia monooxygenase (AMO, Fig. 1.1), the second by hydroxylamine oxidase (HAO, Fig. 1.1), and the third by nitrite oxidoreductase (NXR, Fig. 1.1).<sup>3</sup> The first two steps are carried out by ammonia oxidizing bacteria and archaea (AOB, AOA), the final one by nitrite oxidizers...4
- Scheme 1.3.** The half reactions for denitrification. The first step is catalyzed by a variety of enzymes, depending on the organism, the second step is catalyzed by various types of nitrite reductase (NiR, Fig. 1.1), the third by nitric oxide reductases (NorB, Fig. 1.1), and the fourth by nitrous oxide reductase (NosZ, Fig. 1.1).....5
- Scheme 1.4.** The half reactions for nitrate ammonification. The first step is catalyzed by a variety of enzymes, depending on the organism. In bacteria the second step is catalyzed by the enzyme cytochrome *c* nitrite reductase (ccNiR), which is the major topic of this thesis. Plants also have nitrite reductases capable of reducing nitrite directly to ammonia, but these enzymes are structurally quite different from the bacterial ones.....6
- Scheme 1.5.** The reactions for the anammox (anaerobic ammonia oxidation) process.<sup>26, 27, 29</sup> NO<sub>2</sub><sup>-</sup> is generated from nitrite by specialized nitrite reductases.....8
- Scheme 1.6.** Reactions catalyzed by ccNiR under standard assay conditions. The strong reductant methyl viologen monocation radical, MV<sub>red</sub>, is used as the electron donor, typically in concentrations of 80 – 100 μM.....14
- Scheme 1.7.** Ambiguity associated with electronic structures in iron nitrosyl complexes, and the Enemark-Feltham notation used to deal with it (see text for details).....20
- Scheme 2.1.** Nernst equation used to fit the Fig. 2.1 data. Here  $C_{ox}$  refers to fully oxidized ccNiR, and  $C_{red}$  to the enzyme after a single reduction by  $n$  electrons. The remaining parameters are as defined in the main text.....35
- Scheme 2.2.** Chemical interpretation of the nitrite-loaded ccNiR 2-electron reduction. Fe<sub>H1</sub> represents the active site heme center in various states of oxidation and ligation; see text for details.....38

**Scheme 2.3.** Here  $\text{Fe}_{\text{H1}}$  represents the active site heme center in various states of oxidation and ligation. The solid arrows show the net reduction observed experimentally, while the dashed ones show the steps that likely underlie the observed process; see text for details.....51

**Scheme 2.4.** In the experiments described herein active site reduction in the presence of nitrite appears to proceed via Path 1. Under physiological conditions it will likely proceed via Path 2. In either case free  $\text{NO}\cdot$  release from substitutionally labile  $\{\text{Fe}_{\text{H1}}\text{NO}\}^6$  will be minimized if the standard reduction potential for reduction of  $\{\text{Fe}_{\text{H1}}\text{NO}\}^6$  to  $\{\text{Fe}_{\text{H1}}\text{NO}\}^7$  is much higher than that for reduction of  $\text{Fe}_{\text{H1}}^{\text{III}}(\text{NO}_2^-)$  to  $\{\text{Fe}_{\text{H1}}\text{NO}\}^6$ .....52

**Scheme 3.1.** CcNiR-catalyzed reduction of nitrite to  $\text{NO}\cdot$  by ferrocyanide.....63

**Scheme 4.1.** Methyl viologen accepts an electron to produce  $\text{MV}_{\text{red}}$ , a powerful reductant.....83

**Scheme 4.2.** Monomer-dimer equilibrium of methyl viologen.....85

**Scheme A1.** Equilibrium for nitrite binding with ccNiR.....102

## ACKNOWLEDGEMENTS

I would first and foremost like to acknowledge and thank my supervisor, Professor Andy Pacheco, for his endless support and supervision to prepare me as a scientist and as a better person. I am grateful not only for his guidance in my research, but also for his motivation, comfort and support during my very difficult time in graduate school.

I would like to extend my gratitude and thank to all the professors in my graduate committee; Professor Brian Bennett, Professor Graham Moran, Professor Marius Schmidt and Professor Nicholas Silvaggi for their time, direction and suggestions. I am really grateful to Professor Brian Bennett who helped me a lot taking EPR spectra and analyzing the data, and Professor Marius Schmidt who helped me to obtain critical crystallography results. Professor Moran and Professor Silvaggi helped me to perform stopped-flow experiments. I also want to thank Professor Dennis Bennett who served in my graduate committee for the first two years.

Without the support and help of my lab mates it wouldn't be an easy journey for me to achieve this accomplishment. I especially want to mention my predecessor Dr. Natalia Stein and Dan Pauli, who directly supervised my different experiments in my early time in the PhD program. Dr. Karl Koebke and Dr. Jennifer McGarry also helped me a lot, and I thank them both. My other lab mates over the years, Steve Reinhardt, Shahid, David Koltermann, Victoria Mandella, Alex Drena and Shahama Alam have always made the working environment friendly, enjoyable and cooperative, for which I am very grateful.

Over the years I got the opportunity to supervise some passionate, hard-working undergraduate researchers who contributed to my various research projects. In this regard the greatest contributions were made by Yingxi Mao and Desiree Legaspi-Humiston. Yingxi helped me in

the spectropotentiometric experiments of Chapters 2 and 4, and Desiree contributed to the steady state experiments of Chapter 3. Three other undergraduate students, Kaleb Keefe, Nicholas Robinson and Andrew Niepow, also contributed to this project. Together, the undergraduate research contributions surely enriched my dissertation.

Finally, I wish to gratefully acknowledge the support I got from the National Science Foundation (grants MCB-1330809 and MCB-1616824) throughout my time as a graduate student.

# Chapter 1

## Introduction

### 1.1. Overview of the nitrogen cycle

Although nitrogen is very abundant on earth, almost 80% of the atmosphere consists of dinitrogen gas ( $N_2$ ), it is largely inaccessible in this form to most organisms. This makes nitrogen a scarce resource that often limits primary productivity in many ecosystems.<sup>1-3</sup> Only when nitrogen is converted from dinitrogen gas into ammonia does it become available to primary producers, such as plants.<sup>3-6</sup> In addition to ammonia, nitrogen exists in many different bioavailable forms, including both inorganic (e.g., ammonia, nitrate) and organic (e.g., amino and nucleic acids) that are conveniently referred to as “reactive nitrogen” species.<sup>4-6</sup> Living things interconvert these various forms of reactive nitrogen for two primary reasons.<sup>3, 6, 7</sup> First, nitrogen is a major constituent of biomolecules such as amino and nucleic acids; it is incorporated into biomolecules at the oxidation state of ammonia, which in turn can be generated biologically from dinitrogen or from nitrate. Second, nitrogen interconversion can be coupled to energy transduction. In such cases nitrogen molecules can act as electron donors or acceptors in aerobic or anaerobic respiration, respectively. The major transformations of nitrogen are nitrogen fixation, nitrification, denitrification, anammox (anaerobic ammonia oxidation), and nitrite ammonification (Fig.1.1). These transformations are key to productivity in the biosphere and are highly dependent on the activities of a diverse assemblage of microorganisms, such as bacteria, archaea, and fungi.<sup>3, 6, 8-10</sup>

## Figures

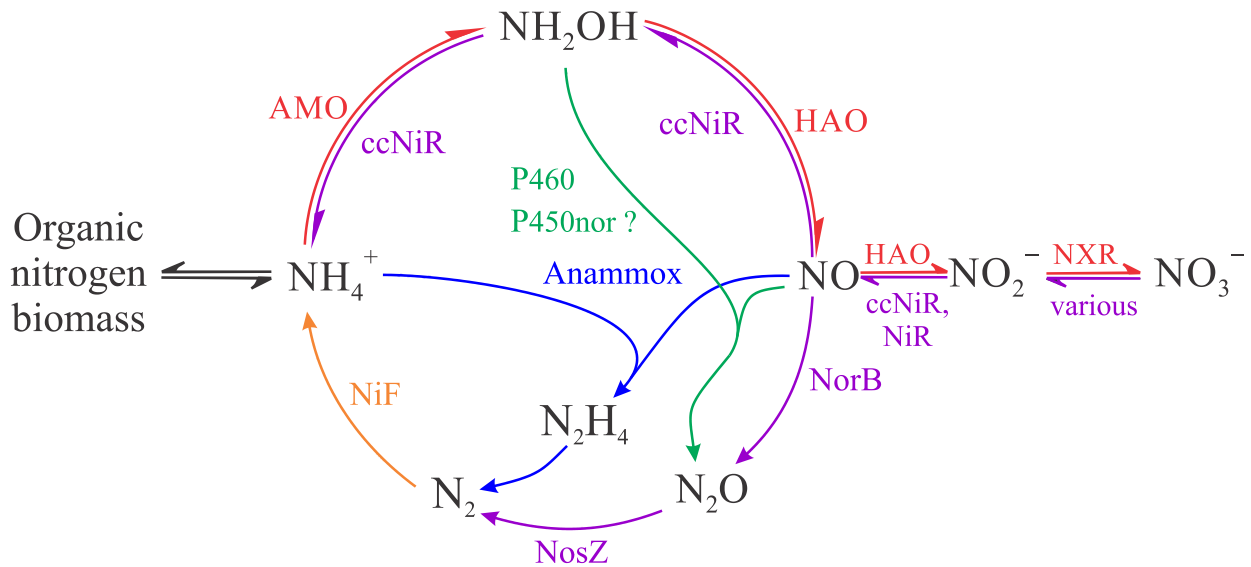
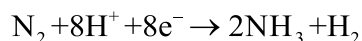


**Figure 1.1.** The nitrogen cycle, showing the five major pathways, and one minor pathway. Orange: nitrogen fixation; Red: nitrification; Purple: nitrate ammonification (nitrate to ammonia), and denitrification (nitrate to dinitrogen); Blue: the anammox process, comproportionation of ammonia and NO. Green: comproportionation of hydroxylamine and NO, a minor process that has been observed in some bacteria and fungi.<sup>11, 12</sup> The enzymes associated with each step are shown next to the corresponding arrows.

Nitrogen fixation is a very energetically expensive process, requiring eight electrons and at least sixteen ATP molecules (Scheme 1.1).<sup>2</sup> Besides a small group of prokaryotes, which do most of the naturally occurring fixation, some nitrogen can be fixed abiotically by lightning. For the last several years though a majority of fixed nitrogen has come from the industrial Haber process, which requires the combustion of fossil fuels.<sup>2</sup>



**Scheme 1.1.** The half reaction for nitrogen fixation. The overall reaction is catalyzed by nitrogenase (NiF in Fig. 1.1).

Nitrogen-fixing genes are found globally in many aerobic habitats such as oceans, lakes and soils, and also in some habitats that are anaerobic or microaerophilic, such as termite guts, sediments, hypersaline lakes, microbial mats, and planktonic crustaceans.<sup>2, 13</sup> Table 1.1 provides some examples of how broadly nitrogen fixing organisms are distributed throughout the biosphere. This broad distribution highlights the importance of the nitrogen fixation process to all life on earth.

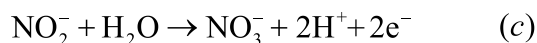
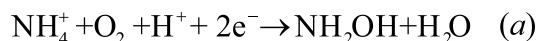
**Table 1.1:** A representation of prokaryotes that are known to carry out nitrogen-fixation (adapted from ref.).

Genus	Phylogentic affiliation	Lifestyle
<i>Nostoc, Anabaena</i>	Bacteria	Free-living, Aerobic, phototrophic
<i>Pseudomonas, Azotobacter, Methylomonas</i>	Bacteria	Free-living, Aerobic, Chemoorganotrophic
<i>Alcaligenes, Thiobacillus</i>	Bacteria	Free-living, Aerobic, Chemolithotrophic
<i>Methanosarcina, Methanococcus</i>	Bacteria	Free-living, Aerobic, Chemolithotrophic
<i>Chromatium, Chlorobium</i>	Bacteria	Free-living, Anaerobic, phototrophic
<i>Desulfovibrio, Clostridium</i>	Bacteria	Free-living, Anaerobic, Chemoorganotrophic
<i>Rhizobium, Frankia</i>	Bacteria	Symbiotic, Aerobic, Chemoorganotrophic

Nitrification is the process by which ammonia is oxidized to nitrate through nitrite and is an aerobic respiration process. For the most part separate organisms oxidize ammonia to nitrite and nitrite to nitrate, though very recently two *Nitrospira* species were identified that may be capable of oxidizing ammonia all the way to nitrate by themselves.<sup>14, 15</sup> More commonly the

oxidation of ammonia to nitrite is carried out by two groups of autotrophic organisms, the ammonia oxidizing bacteria (AOB) and ammonia oxidizing archaea (AOA),<sup>16</sup> while the further oxidation of nitrite to nitrate is performed by nitrite oxidizing bacteria (NOB).<sup>14, 15, 17</sup> The best studied AOB belong to the genus *Nitrosomonas*, while *Nitrobactor* and *Nitrospira* provide archetypal examples of nitrite oxidizers. The importance of AOA has only been realized in the past 20 years, but it is now recognized that these microorganisms dominate some environments, such as oceans.<sup>16, 18</sup>

The oxidation of ammonia to nitrate is a net 8-electron process that is catalyzed stepwise by different enzymes. In the first step (Scheme, 1.2a) 2-electron oxidation of ammonia to hydroxylamine is coupled to the 4-electron reduction of oxygen to water. This step is catalyzed by the enzyme ammonia monooxygenase (AMO, Fig. 1.1).

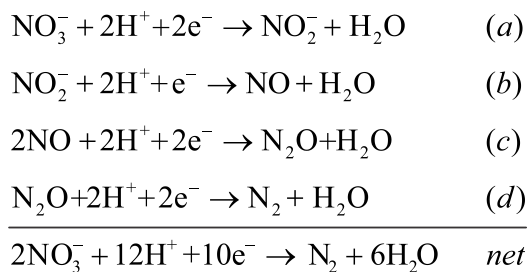


**Scheme 1.2.** The half reactions for nitrification. The first step is catalyzed by the enzyme ammonia monooxygenase (AMO, Fig. 1.1), the second by hydroxylamine oxidase (HAO, Fig. 1.1), and the third by nitrite oxidoreductase (NXR, Fig. 1.1).<sup>3</sup> The first two steps are carried out by ammonia oxidizing bacteria and archaea (AOB, AOA), the final one by nitrite oxidizers.

The second step (Scheme, 1.2b), catalyzed by hydroxylamine oxidase (HAO, Fig. 1.1) is the 4-electron oxidation of hydroxylamine to nitrite. Finally, the 2-electron oxidation of nitrite to nitrate (Scheme, 1.2c) is catalyzed by nitrite oxidoreductase (NXR, Fig. 1.1).<sup>3</sup> Taking into

account the oxygen reduction of the first step, overall nitrification is a net 4-electron oxidation (net equation, Scheme 1.2). Nitrifying organisms are chemoautotrophs, which means that they extract energy for ATP synthesis from chemical sources rather than light (i.e., ammonia and nitrite oxidation), and they can grow with carbon dioxide as their only carbon source.<sup>2</sup>

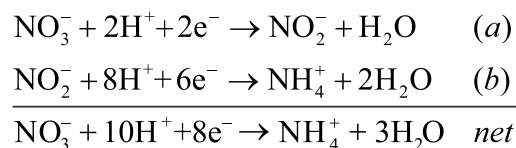
Denitrification is the microbially facilitated reduction of nitrite to dinitrogen through a series of nitrogen oxide intermediates, and it is an anaerobic respiration or dissimilatory process (Scheme 1.3; see also below).<sup>3, 19-21</sup> Several fungi and yeasts can also catalyze dinitrification in mitochondria, but different enzymes are usually involved, and nitrous oxide is the end product instead of dinitrogen.<sup>12, 20</sup> Even in bacteria and algae nitrous oxide is a significant byproduct of denitrification because, as different metalloenzymes catalyze each step of the reduction, the nitrous oxide intermediate has the opportunity to escape.<sup>20</sup>



**Scheme 1.3.** The half reactions for denitrification. The first step is catalyzed by a variety of enzymes, depending on the organism, the second step is catalyzed by various types of nitrite reductase (NiR, Fig. 1.1), the third by nitric oxide reductases (NorB, Fig. 1.1), and the fourth by nitrous oxide reductase (NosZ, Fig. 1.1).

Detailed analysis has also shown that NO· is a compulsory intermediate in the denitrification process. Notice from Fig. 1.1 that this makes NO· a branch-point for many processes in the nitrogen cycle; this point will be further explored below.

Nitrate/nitrite ammonification is a process whereby nitrate is reduced to nitrite, which is then further reduced to ammonia (Scheme 1.4).<sup>21</sup> In this process bioavailable nitrogen is conserved by producing soluble ammonium ion which can be incorporated into biomass. This is in contrast to denitrification (above), where the end product is unreactive dinitrogen gas. Nitrate/nitrite ammonification can be used specifically to generate ammonia needed for biomolecule synthesis (assimilatory nitrate ammonification), it can simply be a byproduct of anaerobic respiration (respiratory nitrate ammonification), or it can be used primarily to dissipate excess reducing power in the cell (dissimilatory nitrate ammonification).<sup>21, 22</sup> Note that there is a subtle difference between respiratory nitrate ammonification and dissimilatory nitrate ammonification that is often ignored in the literature.<sup>22</sup> In respiratory nitrate ammonification the nitrate reduction is coupled to generation of proton motive force or proton potential ( $\Delta p$ ) across a membrane. ATP synthase uses this  $\Delta p$  to catalyze ADP phosphorylation to produce ATP. In dissimilatory nitrate ammonification there need be no coupling to generation of proton motive force.<sup>22</sup>



**Scheme 1.4.** The half reactions for nitrate ammonification. The first step is catalyzed by a variety of enzymes, depending on the organism. In bacteria the second step is catalyzed by the enzyme cytochrome *c* nitrite reductase (ccNiR), which is the major topic of this thesis. Plants also have nitrite reductases capable of reducing nitrite directly to ammonia, but these enzymes are structurally quite different from the bacterial ones.

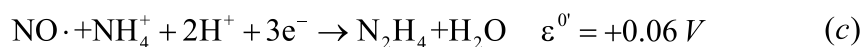
In all types of nitrate ammonification the reduction of nitrate to nitrite and nitrite to ammonia are discrete steps, catalyzed by two separate enzymes. Different enzymes are used by different organisms. Assimilatory nitrate ammonification takes place in plants, fungi and microorganisms. Nitrate reduction is carried out by Euk-NR nitrate reductase in eukaryotes and

by NaS nitrate reductase in prokaryotes,<sup>3</sup> while nitrite reduction is carried out by a cytoplasmic siroheme-containing nitrite reductase.<sup>21</sup> Respiratory nitrate ammonification is carried out by the periplasmic molybdoenzyme NapA which reduces nitrate to nitrite, and by the multi-heme containing cytochrome *c* nitrite reductase (ccNiR, also called NrfA).<sup>21, 23</sup> The latter enzyme is the focus of this thesis, and will be discussed in much greater depth below.

The electron donor for assimilatory nitrite reduction is either NAD(P)H or ferredoxin, and it has been noted that this makes the process dissimilatory as well as assimilatory because it consumes reducing equivalents.<sup>21, 22</sup> In a similar vein ccNiR has been found in bacteria that are incapable of respiratory ammonification. In these organisms ccNiR is believed to help mitigate nitrosative stress and to dissipate excess reducing power, which again is dissimilatory nitrite ammonification.<sup>24, 25</sup> In light of these findings Moreno-Vivian and Ferguson argue persuasively that one should not label specific enzymes as being assimilatory, dissimilatory or respiratory, as has been done in the past. Since these enzymes can sometimes play different roles under different metabolic conditions, the role of each given enzyme should be described for the specific context in which it is being used.<sup>22</sup>

Of the two other nitrogen cycle pathways shown in Fig. 1.1 anaerobic ammonium oxidation (anammox) deserves a brief mention. This is a process in which anammox bacteria catalyze the conversion of ammonium and nitrite to dinitrogen gas through the toxic intermediate hydrazine (N<sub>2</sub>H<sub>4</sub>). Thus, anammox is an alternative to denitrification for returning reactive nitrogen to inert dinitrogen gas. Unlike denitrification, which has been known for about a century, anammox was discovered only recently, and significant advances in understanding the process have only occurred over the past ten years.<sup>26-29</sup>

The net anammox reaction is given in Scheme 1.5*a*. Anammox bacteria have specialized uptake and trafficking systems for both ammonium and nitrite, and isotope labeling confirms that the dinitrogen product contains one nitrogen from nitrite and one from ammonia.<sup>27</sup> Nitric oxide is an obligate intermediate in anammox, and its synthesis is catalyzed by species-dependent NO reductases (Scheme 1.5*b*).<sup>27</sup> It is the NO· that then reacts with ammonium in a partial comproportionation that requires addition of three electrons from other sources, and generates hydrazine (Scheme 1.5*c*); this reaction is catalyzed by hydrazine synthase.<sup>29</sup>



**Scheme 1.5.** The reactions for the anammox (anaerobic ammonia oxidation) process.<sup>26, 27, 29</sup> NO· is generated from nitrite by specialized nitrite reductases.

Finally, hydrazine is oxidized to dinitrogen by hydrazine dehydrogenase in a highly exergonic reaction; indeed, hydrazine is the most powerful biologically available reducing agent known.<sup>27</sup> The ammonium catabolic process takes place in a specialized compartment called the anammoxosome; an electron transport chain within the anammoxosome membrane generates a proton gradient that is coupled to production of ATP.<sup>27</sup>

## 1.2. Ecological importance of reactive nitrogen balance

On the geological timescale microbially-driven processes such as nitrogen fixation, nitrification, and denitrification have been the primary drivers of nitrogen transformations on earth. However over the past hundred years, as human populations have continued to increase, human activities have started to significantly perturb the global nitrogen cycle.<sup>3, 30-32</sup> The biggest nitrogen cycle alteration has come from the invention of the Haber-Bosch process, which produces ammonia industrially from the reaction of H<sub>2</sub> and N<sub>2</sub> at high pressure. This artificial nitrogen fixation has significantly increased the amount of reactive nitrogen available in the biosphere at any given time. Indeed, the use of nitrogen fertilizer increased by about 800% from 1960-2000,<sup>3, 32</sup> and now about 80% of nitrogen found in human tissue at any given moment originated from the Haber-Bosch process.<sup>1, 2</sup> The anthropogenic increase in reactive nitrogen is leading to significant unexpected problems. For example, the increase in reactive nitrogen appears to be leading to nutrient imbalances in trees, changing forest health and declining the biodiversity. Moreover, some have argued that alterations in nitrogen cycle balance may ultimately contribute to an increased risk of parasitic and infectious diseases.<sup>33</sup> Two nitrogen cycle species, nitrate and nitrous oxide, deserve special attention because of the ecological problems that they pose.

Reactive nitrogen in the form of nitrate can readily leach out of the soil and into rivers, where it contaminates drinking water. Furthermore, in marine systems and lakes nitrate-rich water can promote algal blooms that lower the water's oxygen level (algal bloom-induced hypoxia), which is detrimental to life forms low in the water column.<sup>1, 2, 34</sup> One of the famous examples of a persistent algal bloom is the oceanic "dead zone" near the mouth of Mississippi river in the Gulf of Mexico.<sup>34-36</sup>

In addition to nitrate in aquifers, nitrous oxide concentration increases in the atmosphere are also causing problems. Unlike nitrate  $N_2O$  is not a viable fertilizer, and so isn't considered a reactive nitrogen species. It is a comparatively inert byproduct of denitrification and is eventually converted to dinitrogen by a subset of denitrifying bacteria. However, because of its comparative inertness,  $N_2O$  can persist in the atmosphere for prolonged periods of time. This is concerning because  $N_2O$  is a potent greenhouse gas (about 300× more potent than  $CO_2$ ).<sup>3</sup> Furthermore, a recent study showed that  $N_2O$  may now also be the single most important ozone depleting emission on the planet, and is likely to remain as such throughout the 21<sup>st</sup> century.<sup>37, 38</sup>

Many of today's problems with nitrogen cycle imbalance could be alleviated by more efficient use of fertilizer. Over 40% of fertilizer washes out of the root zone as nitrate, or is lost to the atmosphere through denitrification, before it has a chance to be assimilated into biomass.<sup>3</sup> Not only is this a terrible waste of energy, it also leads to the eutrophication, greenhouse effect increase and ozone depletion described above. Clearly a better understanding of the interplay between the various chemical processes in the nitrogen cycle could greatly aid in the search for more efficient and ecologically friendly ways of using fertilizer. To that end, this dissertation presents a mechanistic study of the enzyme cytochrome *c* nitrite reductase (ccNiR) from *Shewanella oneidensis*, which the bacteria use to catalyze nitrite reduction to ammonia for anaerobic respiration (Fig. 1.1).

### 1.3. Overview of ccNiR

CcNiR is a soluble periplasmic bacterial protein. Though the ccNiR used in this study is extracted from *S. oneidensis*, it's been found in several other bacterial species as well. Nitrite ammonifying bacteria use ccNiR as a terminal electron acceptor in anaerobic respiration.<sup>21, 39, 40</sup> The enzyme is a homodimer, and the molecular weight of each protomer is 52-65 kDa depending on the organism from which it's been extracted. Each protomer contains five *c*-type hemes, four of which are six-coordinate *bis*-histidine ligated and low spin (Fig. 1.2). The fifth heme, the active site, is high spin, and instead of histidine it has an unusual lysine ligand in the proximal axial position; its distal axial position is occupied by a labile water in the resting enzyme (Fig. 1.2).<sup>24, 41-46</sup> During catalysis the active site labile water is readily displaced, allowing substrate nitrite to bind. Along with the five hemes, a six-coordinate  $\text{Ca}^{2+}$  ion is also found in each protomer.<sup>44</sup>

Figure 1.2a shows schematically the heme arrangement within the ccNiR dimer, while Fig. 1.2b shows the heme coordination geometry within one protomer in more detail. The hemes are closely packed, with the iron centers of adjacent hemes being roughly 13 Å apart, and the heme edges being in vander Waals contact. In Fig. 1.2 the red heme is the active site where nitrite is reduced, while the purple one, which is solvent-exposed, is the entry-point for electrons coming from the physiological electron donor. The remaining hemes act as a conduit that can shuttle electrons from the entry point to the active site.<sup>41, 45, 47</sup> Notice that the heme arrangement is such that electrons can also hop from one protomer to the other. Thus, electrons entering one protomer can in principle end up at either active site.

## Figures

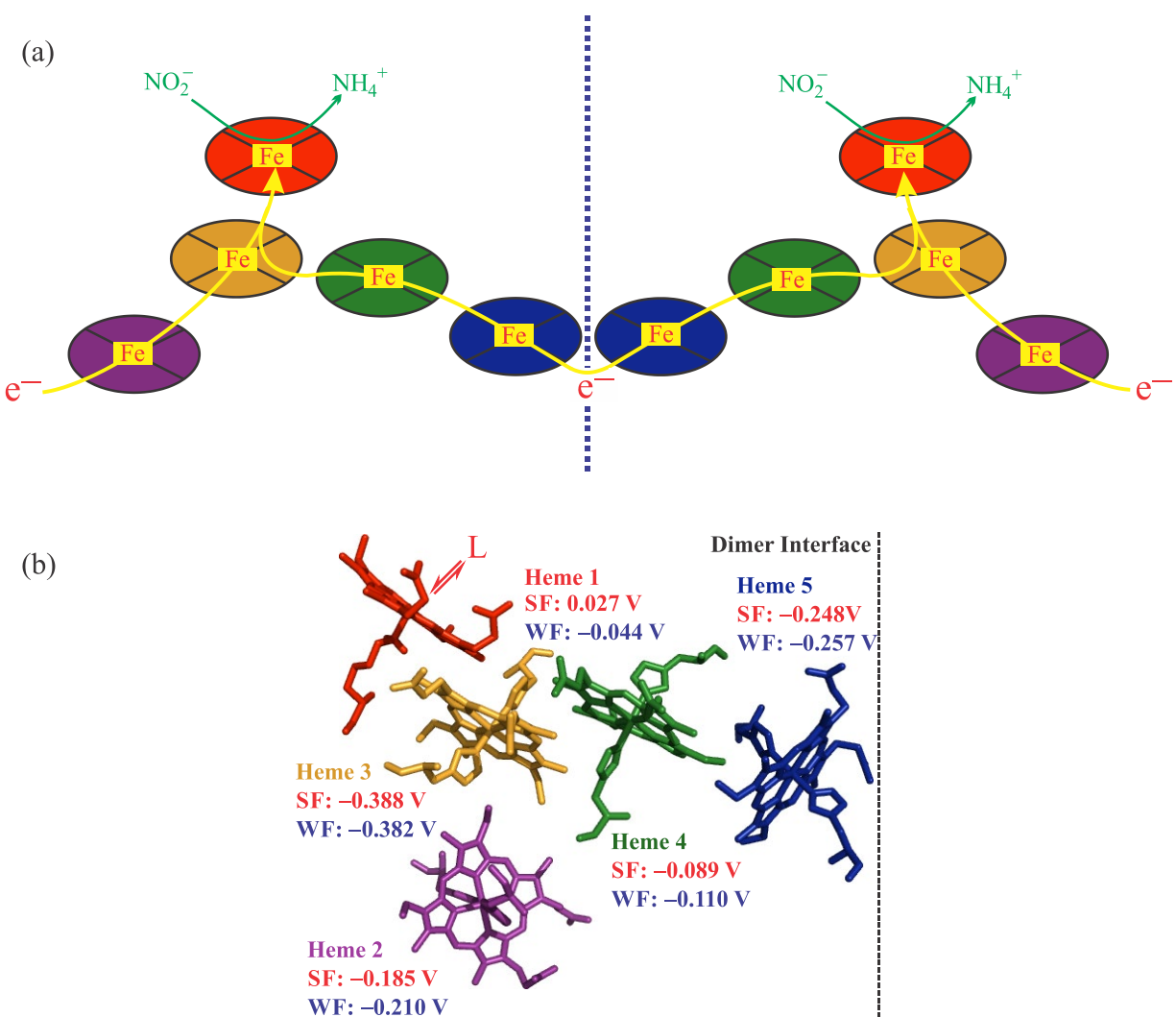


**Figure 1.2.** (a) Heme arrangement within the ccNiR dimer, showing the possible paths of electron flow. (b) Five hemes, and their associated axial ligands, from one of the *Shewanella oneidensis* ccNiR protomers (from the Protein Data Bank, accession number 3UBR; the heme arrangement is virtually identical in ccNiR from other organisms). The *S. oneidensis* heme midpoint potentials previously obtained in the presence of the strong-field (SF) ligand cyanide are shown in red, while those obtained in the presence of only weak-field (WF) ligands such as water are shown in blue (ref.). The dashed vertical line represents the dimer interface.

As seen in Scheme 1.4, the six-electron reduction of nitrite to ammonia concomitantly requires the addition of eight protons. How these protons are supplied during catalysis is therefore a very important question. Three amino acids located close to the active site, His257, Arg103 and Tyr206 in the *S. oneidensis* enzyme (Fig. 1.3), are believed to play important roles in proton handling.<sup>41, 49</sup> Chapter 3 of this thesis will present evidence for His257's role in the first reduction step of nitrite.

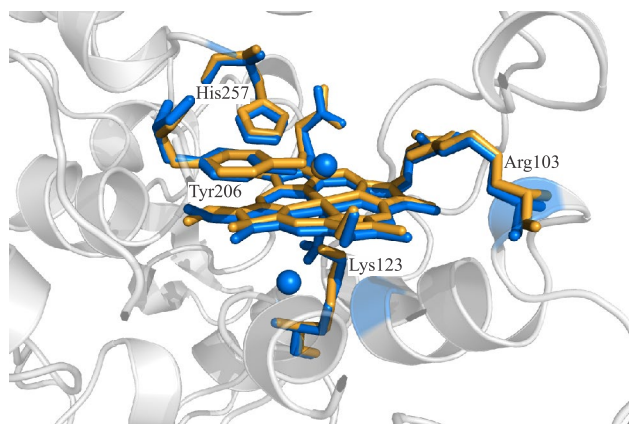
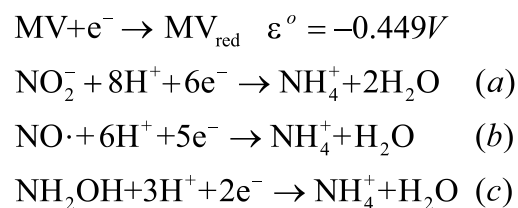


**Figure 1.3.** Active site region of *S. oneidensis* ccNiR. The figure shows the active site heme 1, its unusual proximal ligand Lys123, three conserved active site residues proposed to be catalytically important, the water coordinated to the distal site of heme a in the resting enzyme, and a water that hydrogen bonds to Lys123. The blue structure was obtained at 110K (PDB 6P73, 1.66 Å resolution),<sup>50</sup> while the orange structure was obtained at room temperature using the Laue method (PDB 3UBR, 2.59 Å resolution).<sup>46</sup>

CcNiR's physiological electron donor varies depending on the phylogenetic branch to which the source bacteria belong.  $\delta$ - and  $\epsilon$ -proteobacteria such as *Desulfovibrio desulfuricans* and *Wollinella succinogenes* use a membrane-anchored quinol dehydrogenase called NrfH, whereas  $\gamma$ -proteobacteria typically use a soluble periplasmic tetraheme protein called

NrfB.<sup>41, 45-47</sup> Both *Escherichia coli* and *S. oneidensis* are  $\gamma$ -proteobacteria, but while *E. coli* does in fact use the soluble NrfB, *S. oneidensis* is unusual in utilizing a tetraheme membrane-anchored electron transport protein called CymA as electron donor.<sup>46, 47</sup>

In vitro the standard assay for ccNiR uses methyl viologen monocation radical ( $MV_{\text{red}}$ ) as the nitrite reducing agent (Scheme 1.6). CcNiR also catalyzes the reduction of nitric oxide and hydroxylamine by  $MV_{\text{red}}$ , based on which ccNiR-bound nitric oxide and hydroxylamine have long been assumed to be intermediates in the reduction process (Scheme 1.6). However, ammonia is the sole product in the  $MV_{\text{red}}$  assay, and moreover no enzyme intermediate has ever been detected with this standard assay.<sup>42, 43, 46, 51, 52</sup>



**Scheme 1.6.** Reactions catalyzed by ccNiR under standard assay conditions. The strong reductant methyl viologen monocation radical,  $MV_{\text{red}}$ , is used as the electron donor, typically in concentrations of 80 – 100  $\mu\text{M}$ .

Up until now it has been assumed that ccNiR-catalyzed nitrite reduction in vivo likewise proceeds in one step to generate ammonia exclusively. This would appear to pose a challenge for mechanistic studies, which require intermediate detection as a means of tracking the path of the reaction under study. However recently our group showed that when the strong-field ligand cyanide binds to the active site of *S. oneidensis* ccNiR it has a significant effect on the active site midpoint potential, shifting it by nearly 70 mV in the positive direction, to +27 mV vs SHE (Fig. 1.2b).<sup>48</sup> CcNiR's physiological substrate nitrite is also a strong-field ligand when it binds a metal

via the nitrogen atom, and might be expected to have a similar effect on heme 1's midpoint potential. This is important because *S. oneidensis* ccNiR-catalyzed nitrite reduction to ammonia does not proceed appreciably at potentials higher than about  $-120$  mV vs SHE,<sup>53, 54</sup> so if nitrite-bound heme 1 were to reduce at a potential well above  $-120$  mV vs SHE it would effectively generate a stalled catalytic intermediate. The results presented in Chapter 2 confirm that, like cyanide-bound heme 1, nitrite-bound heme 1 also reduces at a potential that is much too high for ammonia generation, thus allowing a reduced nitrite-loaded heme 1 species to be trapped and studied. The electrochemical behavior of the *S. oneidensis* enzyme in the presence of nitrite is also found to differ in important ways from its behavior in the presence of cyanide. Chapter 3 shows that, in the presence of the weak reductant ferrocyanide, ccNiR catalyzes the one-electron reduction of nitrite to nitric oxide instead of the six-electron reduction seen when the more potent  $MV_{red}$  is used. The results of Chapters 2 and 3 have mechanistic implications that extend beyond the chemistry of ccNiR, to encompass overall nitrogen cycle chemistry.

#### 1.4. Nitric oxide in biology

Enzymatic species that formally contain nitric oxide bound to metal centers (“metal nitrosyls”) play very important roles in nitrogen cycle chemistry. This is because, as seen in Fig. 1.1,  $NO\cdot$  sits at a branch point of sorts within the nitrogen cycle. All processes involving nitrate reduction initially generate  $NO\cdot$  at least formally, after which the  $NO\cdot$  can be further reduced either to ammonia or to dinitrogen, or it can comproportionate with ammonia or with hydroxylamine (Fig. 1.1). Similarly, ammonia oxidation to nitrate passes through  $NO\cdot$ . Metal nitrosyl chemistry has been extensively studied over the past forty years, both in biological

systems and in simple transition metal complexes. Given the important place of metal nitrosyls in the nitrogen cycle, this section provides a brief review of their chemistry.

**1.4.1. Overview of free nitric oxide and its role in biology.** Until the 1980s nitric oxide had been deemed nothing more than a smog producing and toxic material. This view changed abruptly when it was found that nitric oxide is endogenously produced in humans, and moreover is an important signaling molecule in the cardiovascular and central nervous system.<sup>55-57</sup> Nitric oxide is now known to be involved in diverse physiological processes that include smooth muscle relaxation, platelet inhibition, immune regulation, neurotransmission and penile erection.<sup>58, 59</sup> It should be noted that though “nitric oxide” properly refers to the neutral free radical  $\text{NO}\cdot$ , in the literature it is common to call  $\text{NO}^+$  and  $\text{NO}^-$  nitric oxide as well, though the proper names for these species are nitrosonium cation and nitroxyl anion, respectively.<sup>58, 60</sup> Herein the name nitric oxide is used only to refer to the neutral radical  $\text{NO}\cdot$ .

After the initial discovery of nitric oxide’s role in human physiology during the ‘80s most  $\text{NO}\cdot$  research continued to focus on mammalian systems. Very recently though some studies have turned to the role of  $\text{NO}\cdot$  in green plant cells, and it’s now widely accepted that  $\text{NO}\cdot$  is produced endogenously in plants as well.<sup>61</sup> Nitric oxide appears to be involved in many plant physiology processes including seed generation, root growth, flowering, fruit ripening, defense responses, abiotic stress, and plant-microbial interactions.<sup>61-64</sup>

Figure 1.4 shows a molecular orbital diagram that makes clear why nitric oxide is a radical. It has an odd number of electrons, with the highest energy one occupying a  $\pi$ -antibonding orbital.<sup>65</sup> Notice that oxidation of  $\text{NO}\cdot$  will remove the  $\pi$ -antibonding electron thus

increasing the bond order, whereas reduction will add a second  $\pi$ -antibonding electron, making a di radical and decreasing the bond order.

## Figures

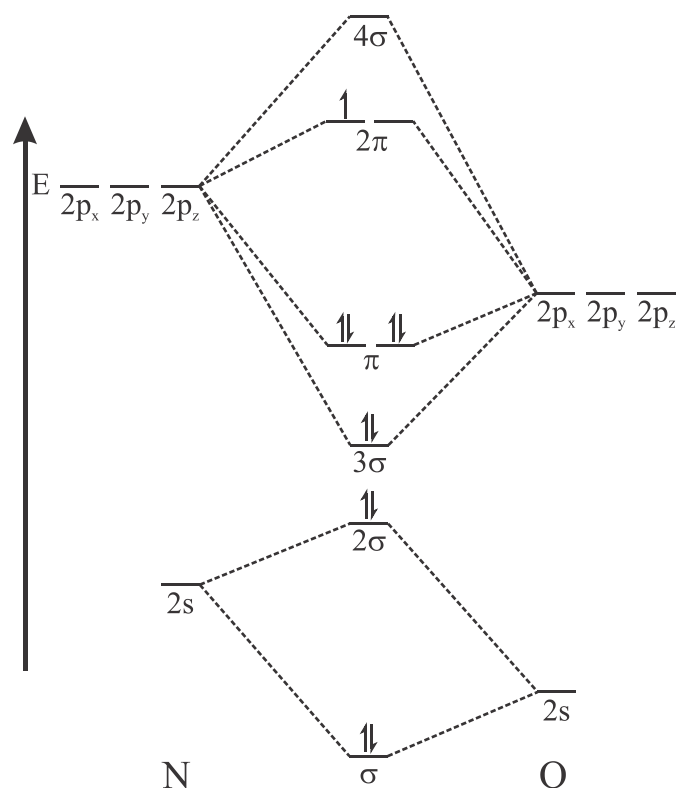


**Figure 1.4.** Molecular orbital diagram for  $\text{NO}\cdot$ . Oxidation of the neutral molecule removes a  $\pi$ -antibonding electron thus increasing the bond order, whereas reduction adds a  $\pi$ -antibonding electron, making a di radical and decreasing the bond order.

These theoretical predictions are confirmed by experiment; the nitrosonium cation  $\text{NO}^+$  has a shorter N-O bond length and higher N-O stretching frequency than  $\text{NO}\cdot$ , whereas the nitroxyl anion  $\text{NO}^-$  has a longer bond length and lower N-O stretching frequency (Table 1.2).<sup>58</sup> The

oxidation state of the NO fragment, both free and metal-bound, is conveniently monitored by infrared or electron paramagnetic resonance (EPR) spectroscopy; the former reports on the N-O stretching frequency, the latter on the number of unpaired electrons associated with the NO fragment.<sup>58, 66</sup>

**Table 1.2.** Variations in N-O bond length and stretching frequency in NO<sup>n</sup> species\*

NO Species	Nitrogen Oxidation Number	Bond Length	N-O stretch (cm <sup>-1</sup> )
NO <sup>+</sup>	3+	0.95	2300
NO·	2+	1.15	1840
NO <sup>-</sup>	1+	1.26	1290

\* Adapted from ref.

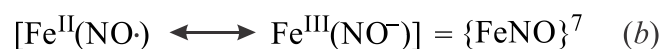
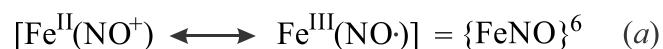
In vivo nitric oxide is synthesized from L-arginine in a two-step process catalyzed by a class of enzymes called nitric oxide synthases (NOS), of which there are two major types.<sup>67, 68</sup> The isoforms eNOS (“endothelial”) and nNOS (“neuronal”) generate small quantities of NO· that are then used for signaling, whereas a third isoform, iNOS (“inducible”) is used by the immune system to generate large and toxic quantities of NO· for antiseptic use. As the name iNOS implies, this isoform is inducible and only synthesized when needed.<sup>67-69</sup>

A variety of bioassays show that biosynthesized NO· is rapidly captured by metals and cysteine thiols so that free NO· is actually quite short lived.<sup>70-73</sup> This is an important feature of its signaling role because it limits its effects both spatially and temporally. The primary recipient of the NO· signal is a heme enzyme called soluble guanylate cyclase (sGC).<sup>74</sup> When NO· binds to sGC it enhances the rate at which the enzyme catalyzes cyclic GMP formation by several

hundred fold,<sup>75</sup> thus starting a signaling cascade. In addition to sGC NO· interacts with many other heme and non-heme metal centers, and with cysteine thiol groups. The best studied example is the interaction of NO· with hemoglobin (Hb).<sup>58</sup> Nitric oxide can interact with both the Hb heme iron and with an accessible cysteine thiol, and both of these interactions appear to be physiologically important.<sup>70-73</sup> Given the importance of metal-nitrosyls in the handling of nitric oxide, the following section provides a brief review of these species.

**1.4.2. Heme and non-hemenitrosyl complexes.** The study of metal nitrosyls poses an interesting electron counting challenge. For example, for iron nitrosyl complexes one might anticipate encountering the following formal ligand and metal electronic states: NO<sup>+</sup> ( $S=0$ ), NO· ( $S=1/2$ ), <sup>1</sup>NO<sup>-</sup> ( $S=0$ ), <sup>3</sup>NO<sup>-</sup> ( $S=1$ ), Fe(II) ( $S= 0, 1, 2$ ), Fe(III) ( $S= 1/2, 3/2$  or  $5/2$ ), Fe (IV) ( $S= 1, 2$ ).<sup>60</sup> However, it is often difficult to decide a priori which ligand and metal electronic states go together. Scheme 1.7 illustrates the challenge for the two most commonly observed iron nitrosyls and shows how it is typically tackled using the “Enemark-Feltham” notation.<sup>76</sup> Scheme 1.7a shows a species that could be equally well represented by resonance forms in which a nitrosonium cation is bound to a ferrous center or neutral nitric oxide is bound to a ferric center. In the Enemark-Feltham shorthand this species is written as {FeNO}<sup>6</sup>, meaning that it has six valence electrons.<sup>76</sup> Thus, in the nitrosonium-ferrous resonance form you have NO<sup>+</sup> with no electrons in the antibonding orbital together with Fe(II) which is d<sup>6</sup>, for a total of six valence electrons, while in the (NO·)-ferric resonance form you have NO· with one electron in the antibonding orbital together with Fe(III) which is d<sup>5</sup>, again for a total of six valence electrons. Similarly for the species in Scheme 1.7b, which is written as {FeNO}<sup>7</sup>. Now the resonance

forms are NO· bound to a ferrous center (one ligand antibonding electron plus six metal d electrons give a total of seven valence electrons) and nitroxyl bound to a ferric center (two ligand antibonding electrons plus five metal d electrons also give a total of seven valence electrons). In addition to the two iron nitrosyl species shown in Scheme 1.7 there is a third that is biologically relevant. In Enemark-Feltham notation this species is {FeNO}<sup>8</sup>, which can formally be thought of as being a ferrous nitroxyl species (Fe(II) – NO<sup>-</sup>).<sup>60, 77, 78</sup> The nitroxyl moiety in biological {FeNO}<sup>8</sup> species is typically protonated at the nitrogen, and this is represented as {Fe(HNO)}<sup>8</sup> using an extension of the Enemark-Feltham notation.<sup>77</sup>



**Scheme 1.7.** Ambiguity associated with electronic structures in iron nitrosyl complexes, and the Enemark-Feltham notation used to deal with it (see text for details).<sup>76</sup>

The Enemark-Feltham notation has two big advantages. The first is that it is compact, and the second is that it does not immediately bias the reader towards one or another resonance form. This is important because all the resonance forms seen in Scheme 1.7 are possible, and one can only determine which is most appropriate in a given case by carefully combining structural, spectroscopic and computational studies.<sup>60, 78-81</sup> By far the best studied iron nitrosyl systems are porphyrin complexes, and much has been learned from model systems; a recent review by Hunt and Lehnert provides an excellent summary of twenty years of research into these systems.<sup>78</sup> One example from the review is a study of five-coordinate (5C) and six-coordinate (6C) synthetic ferrous porphyrin complexes, which have significantly different

spectroscopic properties despite all being  $\{\text{FeNO}\}^7$  species. In the 5C species the unpaired electron is in a molecular orbital that spreads the unpaired spin density fairly evenly between the nitrogen and the iron centers, to the point where a third resonance form for Scheme 1.7b becomes appropriate:  $\text{Fe(I)} - \text{NO}^+$ . When an axial ligand is bound *trans* to the  $\text{NO}\cdot$  moiety the  $\sigma$ -bonds of both the  $\text{NO}\cdot$  and *trans* ligand are substantially weakened (a ground state  $\sigma$ -*trans* effect),<sup>78</sup> and this has the knock-on effect of localizing the unpaired electron more on the nitrogen. Now the most appropriate resonance form from Scheme 1.7b will be  $\text{Fe(II)} - \text{NO}\cdot$ , with the  $\text{Fe(II)}$  in a low-spin configuration with d electrons paired.

In this dissertation the Enemark-Feltham notation will be used extensively to discuss the putative catalytic intermediates of ccNiR. The physical characterization of intermediate species will be presented in Chapter 2, while the chemical properties of the intermediates will be described in Chapter 3.

## 1.5. References

- [1] Howarth, R. W. (2008) Coastal nitrogen pollution: a review of sources and trends globally and regionally, *Harmful Algae* 8, 14-20.
- [2] Bernhard, A. E. (2010) The nitrogen cycle: processes, players and human impact, *Nat. Educ. Knowl.*, 2(2):12.
- [3] Canfield, D. E., Glazer, A. N., and Falkowski, P. G. (2010) The Evolution and Future of Earth's Nitrogen Cycle, *Science* 330, 192-196.
- [4] Likens, G. E., Bormann, F. H., and Johnson, N. M. (1981) Interactions between major biogeochemical cycles in terrestrial ecosystems, In *Some perspectives of the major biogeochemical cycles* (Likens, G. E., Ed.), pp 93-112, Wiley, New York, NY.
- [5] Falkowski, P. G. (1997) Evolution of the nitrogen cycle and its influence on the biological sequestration of CO<sub>2</sub> in the ocean, *Nature* 387, 272-275.
- [6] Falkowski, P. G., and Godfrey, L. V. (2008) Electrons, life and the evolution of earth's oxygen cycle, *Phil. Trans. R. Soc. B.* 363, 2705-2716.
- [7] Lam, P., and Kuypers, M. M. M. (2011) Microbial nitrogen cycling processes in oxygen minimum zones, *Annu. Rev. Mar. Sci.* 3, 317-345.
- [8] Raymond, J., Siefert, J. L., Staples, C. R., and Blankenship, R. E. (2004) The natural history of nitrogen fixation, *Mol. Biol. Evol.* 21, 541-554.
- [9] Fennel, K., Follows, M., and Falkowski, P. G. (2005) The co-evolution of the nitrogen, carbon and oxygen cycles in the proterozoic ocean, *Am. J. Sci.* 305, 526-545.
- [10] Godfrey, L. V., and Falkowski, P. G. (2009) The cycling and redox state of nitrogen in the archaean ocean, *Nat. Geosci.* 2, 725-729.
- [11] Caranto, J. D., Vilbert, A. C., and Lancaster, K. M. (2016) *Nitrosomonas europaea* cytochrome P460 is a direct link between nitrification and nitrous oxide emission, *PNAS* 113, 14704-14709.
- [12] Shoun, H., Fushinobu, S., Jiang, L., Kim, S.-W., and Wagaki, T. (2012) Fungal denitrification and nitric oxide reductase cytochrome P450nor, *Phil. Trans. R. Soc. B.* 367, 1186-1194.
- [13] Zehr, J. P., Jenkins, B. D., Short, S. M., and Steward, G. F. (2003) Nitrogenase gene diversity and microbial community structure: a cross-system comparison, *Environ. Microbiol.* 5, 539-554.

- [14] Daims, H., Lebedeva, E. V., Pjevac, P., Herbold, C., Albertsen, M., Jehmlich, N., Palatinszky, M., Vierheilig, J., Kirkegaard, R. H., von Bergen, M., Rattei, T., Bendinger, B., Nielsen, P. H., and Wagner, M. (2015) Complete nitrification by *Nitrospira* bacteria, *Nature* 528, 504-509.
- [15] van Kessel, M. A. H. J., Speth, D. R., Albertsen, M., Nielsen, P. H., Op den Camp, H. J., Kartal, B., Jetten, M. S. M., and Lucker, S. (2015) Complete nitrification by a single microorganism, *Nature* 528, 555-559.
- [16] Hatzenpichler, R. (2012) Diversity, physiology, and niche differentiation of ammonia-oxidizing archaea, *Appl. Environ. Microbiol.* 78, 7501-7510.
- [17] Marsh, K. L., Sims, G. K., and Mulvaney, R. L. (2005) Availability of urea to autotrophic ammonia-oxidizing bacteria as related to the fate of <sup>14</sup>C- and <sup>15</sup>N-labeled urea added to soil, *Biol. Fertil. Soils* 42, 137-145.
- [18] Qin, W., Amin, S. A., Martens-Habbena, W., Walker, C. B., Urakawa, H., Devol, A. H., E., I. A., Moffett, J. W., Armbrust, E. V., and Stahl, D. A. (2014) Marine ammonia-oxidizing archaeal isolates display obligate mixotrophy and wide ecotypic variation, *Proc. Natl. Acad. Sci. USA* 111, 12504-12509.
- [19] Shiro, Y. (2012) Structure and function of bacterial nitric oxide reductases, *Biochim. Biophys. Acta* 1817, 1907-1913.
- [20] Wasser, I. M., de Vries, S., Moenne-Loccoz, P., Schroder, I., and Karlin, K. D. (2002) Nitric Oxide in Biological Denitrification: Fe/Cu Metalloenzyme and Metal Complex NOx Redox Chemistry, *Chemical Reviews* 102, 1201-1234.
- [21] Simon, J. (2002) Enzymology and bioenergetics of respiratory nitrite ammonification, *FEMS Microbiol. Rev.* 26, 285-309.
- [22] Moreno-Vivian, C., and Ferguson, S. J. (1998) Definition and distinction between assimilatory, dissimilatory and respiratory pathways, *Mol. Microbiol.* 29, 661-669.
- [23] Cruz-Garcia, C., Murray, A. E., Klappenbach, J. A., Stewart, V., and Tiedje, J. M. (2007) Respiratory nitrate ammonification by *Shewanella oneidensis* MR-1, *J. Bacteriol.* 189, 656-662.
- [24] Pereira, I., LeGall, J., Xavier, A., and Teixeira, M. (2000) Characterization of a heme c nitrite reductase from a non-ammonifying microorganism, *Desulfovibrio vulgaris* Hildenborough, *Biochim. Biophys. Acta* 1481, 119-130.

- [25] Tikhonova, T., Tikhonov, A., Trofimov, A., Polyakov, K., Boyko, K., Cherkashin, E., Rakitina, T., Sorokin, D., and Popov, V. (2012) Comparative structural and functional analysis of two octaheme nitrite reductases from closely related *Thioalkalovibrio* species, *FEBS J.* 279, 4052-4061.
- [26] Kartal, B., Maalcke, W. J., de Almeida, N. M., Cirpus, I., Gloerich, J., Geerts, W., Op den Camp, H. J., Harhangi, H. R., Janssen-Megens, E. M., K-J., F., Stunnenberg, H. G., Keltjens, J. T., Jetten, M. S. M., and Strous, M. (2011) Molecular mechanism of anaerobic ammonium oxidation, *Nature* 479, 127-132.
- [27] Kartal, B., Almeida, N. M., Maalcke, W. J., Op den Camp, H. J., Jetten, M. S. M., and Keltjens, J. T. (2013) How to make a living from anaerobic ammonium oxidation, *FEMS Microbiol. Rev.* 37, 428-461.
- [28] Maalcke, W. J., Dietl, A., Marritt, S. J., Butt, J. N., Jetten, M. S. M., Keltjens, J. T., Barends, T. R. M., and Kartal, B. (2014) Structural basis of biological NO generation by octaheme oxidoreductases, *J. Biol. Chem.* 289, 1228-1242.
- [29] Dietl, A., Ferousi, C., Maalcke, W. J., Menzel, A., de Vries, S., Keltjens, J. T., Jetten, M. S. M., Kartal, B., and Barends, T. R. M. (2015) The inner workings of the hydrazine synthase multiprotein complex, *Nature* 527, 394-397.
- [30] Vitousek, P. M., Mooney, H. A., Lubchenko, J., and Melillo, J. M. (1997) Human domination of earth's ecosystems, *Science* 277, 494-499.
- [31] Holland, E. A., Dentener, F. J., Brasswell, B. H., and Sulzman, J. M. (1999) Contemporary and pre-industrial global reactive nitrogen budgets, *Biogeochemistry* 46, 7-43.
- [32] Fixen, P. E., and West, F. B. (2002) Nitrogen fertilizers: meeting contemporary challenges, *Ambio* 31, 169-176.
- [33] Johnson, P. T. J., Townsend, A. R., Cleveland, C. C., Glibert, P. M., Howarth, R. W., McKenzie, V. J., Rejmankova, E., and Ward, M. H. (2010) Linking environmental nutrient enrichment and disease emergence in humans and wildlife, *Ecol. Appl.* 20, 16-29.
- [34] Rabalais, N. N., Turner, R. E., and Wiseman, W. J. (2002) Gulf of Mexico hypoxia, a.k.a "the dead zone", *Annu. Rev. Ecol. Syst.* 33, 235-263.
- [35] Dybas, C. L. (2005) Dead zones spreading in world oceans, *BioSci* 55, 552-557.

- [36] Camargo, J. A., and Alonso, A. (2006) Ecological and toxicological effects of inorganic nitrogen pollution in aquatic ecosystems: a global assesment, *Env. Internat.* 32, 831-849.
- [37] Ravishankara, A. R., Daniel, J. S., and Portmann, R. W. (2009) Nitrous oxide (N<sub>2</sub>O): the dominant ozone-depleting substance emitted in the 21st century, *Science* 326, 123-125.
- [38] Wuebbles, D. J. (2009) Nitrous oxide: no laughing matter, *Science* 326, 56-57.
- [39] Ehrlich, H. L. (2002) *Geomicrobiology*, 4th ed., Marcel Dekker, Inc, New York, NY.
- [40] Fenchel, T., King, G. M., and Blackburn, T. H. (1998) *Bacterial Biogeochemistry*, 2nd ed., Academic Press, London.
- [41] Einsle, O., Stach, P., Messerschmidt, A., Simon, J., Kroger, A., Huber, R., and Kroneck, P. M. H. (2000) Cytochrome c nitrite reductase from *Wolinella succinogenes* - Structure at 1.6 angstrom resolution, inhibitor binding, and heme-packing motifs, *J. Biol. Chem.* 275, 39608-39616.
- [42] Einsle, O., Messerschmidt, A., Stach, P., Bourenkov, G. P., Bartunik, H. D., Huber, R., and Kroneck, P. M. H. (1999) Structure of cytochrome c nitrite reductase, *Nature* 400, 476-480.
- [43] Bamford, V. A., Angove, H. C., Seward, H. E., Thomson, A. J., Cole, J. A., Butt, J. N., Hemmings, A. M., and Richardson, D. J. (2002) Structure and spectroscopy of the periplasmic cytochrome c nitrite reductase from *Escherichia coli*, *Biochemistry* 41, 2921-2931.
- [44] Cunha, C. A., Macieira, S., Dias, J. M., Almeida, G., Goncalves, L. L., Costa, C., Lampreia, J., Huber, R., Moura, J. J. G., Moura, I., and Romao, M. J. (2003) Cytochrome c nitrite reductase from *Desulfovibrio desulfuricans* ATCC 27774 - The relevance of the two calcium sites in the structure of the catalytic subunit (NrfA), *J. Biol.Chem.* 278, 17455-17465.
- [45] Rodrigues, M. L., Oliveira, T., Matias, P. M., Martins, C., Valente, F. M., Pereira, I. A., and Archer, M. (2006) Crystallization and preliminary structure determination of the membrane-bound complex cytochrome c nitrite reductase from *Desulfovibrio vulgaris* Hildenborough, *Acta Cryst. F* 62, 565-568.
- [46] Youngblut, M., Judd, E. T., Srajer, V., Sayyed, B., Goelzer, T., Elliott, S. J., Schmidt, M., and Pacheco, A. A. (2012) Laue crystal structure of *Shewanella oneidensis* cytochrome c nitrite reductase from a high-yield expression system, *J. Biol. Inorg. Chem.* 17, 647-662.

- [47] Gao, H., Yang, Z. K., Barua, S., Reed, S. B., Romine, M. F., Nealson, K. H., Fredrickson, J. K., Tiedje, J. M., and Zhou, J. (2009) Reduction of nitrate in *Shewanella oneidensis* depends on atypical NAP and NRF systems with NapB as a preferred electron transport protein from CymA to NapA, *ISME Journal* 3, 966-976.
- [48] Stein, N., Love, D., Judd, E. T., Elliott, S. J., Bennett, B., and Pacheco, A. A. (2015) Correlations between the electronic properties of *Shewanella oneidensis* cytochrome *c* nitrite reductase (ccNiR) and its structure: effects of heme oxidation state and active site ligation, *Biochemistry* 54, 3749-3758.
- [49] Clarke, T. A., Kemp, G. L., Van Wonderen, J. H., Doyle, R. A. S., Cole, J. A., Tovell, N., Cheesman, M. R., Butt, J. N., Richardson, D. J., and Hemmings, A. M. (2008) Role of a conserved glutamine residue in tuning the catalytic activity of *Escherichia coli* Cytochrome *c* nitrite reductase, *Biochemistry* 47, 3789-3799.
- [50] Ali, M., Stein, N., Mao, Y., Shahid, S., Schmidt, M., Bennett, B., and Pacheco, A. A. (2019) Trapping of a putative intermediate in the cytochrome *c* nitrite reductase (ccNiR)-catalyzed reduction of nitrite: implications for the ccNiR reaction mechanism *J. Am. Chem. Soc.* 141, 13358-13371.
- [51] Einsle, O., Messerschmidt, A., Huber, R., Kroneck, P. M. H., and Neese, F. (2002) Mechanism of the six-electron reduction of nitrite to ammonia by cytochrome *c* nitrite reductase, *J. Am. Chem. Soc.* 124, 11737-11745.
- [52] Poock, S., Leach, E., Moir, J., Cole, J., and Richardson, D. (2002) Respiratory Detoxification of Nitric Oxide by the Cytochrome *c* Nitrite Reductase of *Escherichia coli*, *J. Biol. Chem.* 277, 23664-23669.
- [53] Judd, E. T., Youngblut, M., Pacheco, A. A., and Elliott, S. J. (2012) Direct Electrochemistry of *Shewanella oneidensis* Cytochrome *c* Nitrite Reductase: Evidence of Interactions across the Dimeric Interface, *Biochemistry* 51, 10175-10185.
- [54] Judd, E. T., Stein, N., Pacheco, A. A., and Elliott, S. J. (2014) Hydrogen bonding networks tune proton-coupled redox steps during the enzymatic six-electron conversion of nitrite to ammonia, *Biochemistry* 53, 5638-5646.
- [55] Ignarro, L. J., Byrns, R. E., Buga, G. M., and Wood, K. S. (1987) Endothelium-derived relaxing factor from pulmonary artery and vein possesses pharmacologic and chemical properties identical to those of nitric oxide radical, *Circ. Res.* 61, 866-879.

- [56] Palmer, R. M. J., Ferrige, A. G., and Moncada, S. (1987) Nitric oxide release accounts for the biological activity of endothelium-derived relaxing factor, *Nature* 327, 524-526.
- [57] Lancaster, J., (Ed.) (1996) *Nitric Oxide, Principles and Actions*, Academic Press, San Diego.
- [58] Stamler, J. S., Singel, D. J., and Loscalzo, J. (1992) Biochemistry of nitric oxide and its redox-activated forms, *Science* 258, 1898-1902.
- [59] Hill, B. G., Dranka, B. P., Bailey, S. M., Lancaster, J. R., and Darley-Usmar, V. M. (2010) What part of NO don't you understand? Some answers to the cardinal questions in nitric oxide biology, *J. Biol. Chem.* 285, 19699-19704.
- [60] Serres, R. G., Grapperhaus, C. H., Bothe, E., Bill, E., Weyhermuller, T., Neese, F., and Wieghardt, K. (2004) Structural, spectroscopic, and computational study of an octahedral, Non-Heme {Fe-NO}<sup>6-8</sup> series: [Fe(NO)(cyclam-ac)]<sup>2+/<sup>+</sup>/<sup>0</sup></sup>, *J. Am. Chem. Soc.* 126, 5138-5153.
- [61] Corpas, F. J., and Barroso, J. B. (2015) Nitric oxide from a green perspective, *Nitric oxide* 45, 15-19.
- [62] Valderrama, R., Corpas, F. J., Carreras, A., Fernandez-Ocana, A., Chaki, M., Luque, F., Gomez-Rodriguez, M. V., Colmenero-Varea, P., del Rio, L. A., and Barroso, J. B. (2007) Nitrosative stress in plants, *FEBS Lett.* 581, 453-461.
- [63] Besson-Bard, A., Pugin, A., and Wendehenne, D. (2008) New insights into nitric oxide signalling in plants, *Annu. Rev. Plant Biol.* 59, 21-39.
- [64] Chaki, M., Valderrama, R., Fernandez-Ocana, A., Carreras, A., Gomez-Rodriguez, M. V., Lopez-Jaramillo, J., Begara-Morales, J. C., Sanchez-Calvo, B., Luque, F., Leterrier, M., Corpas, F. J., and Barroso, J. B. (2011) High temperature triggers the metabolism of S-nitrosothiols in sunflower mediating a process of nitrosative stress which provokes the inhibition of ferredoxin-NADP reductase by tyrosine nitration, *Plant, Cell, Environ.* 34, 1803-1818.
- [65] McCleverty, J. A. (2004) Chemistry of nitric oxide relevant to biology, *Chem. Rev.* 104, 403-418.
- [66] Westcott, B. L., and Enemark, J. H. (1999) Transition Metal Nitrosyls, In *Inorganic Electronic Structure and Spectroscopy* (Solomon, E. I., and Lever, A. B. P., Eds.), pp 435-439, John Wiley and Sons, Inc., New York, NY.

- [67] Moncada, S., Palmer, R. M. J., and Higgs, E. A. (1991) *Pharmacol. Rev.* *43*, 109-142.
- [68] Roman, L. J., Martasek, P., and Masters, B. S. S. (2002) Intrinsic and extrinsic modulation of nitric oxide synthase activity, *Chem. Rev.* *102*, 1179-1189.
- [69] Bogdan, C. (2001) Nitric oxide and the immune response, *Nat. Immunol.* *2*, 907-916.
- [70] McMahon, T. J., Moon, R. E., Lusching, B. P., Carraway, M. S., Stone, A. E., W., S. B., Gow, A. J., Pawloski, J. R., Watke, P., Singel, D. J., Piantadosi, C. A., and Stamler, J. S. (2002) Nitric oxide in the human respiratory cycle, *Nat. Med.* *8*, 711-717.
- [71] Stamler, J. S., Toone, E. J., Lipton, S. A., and Sucher, N. J. (1997) (S)NO signals: translocation, regulation, and a consensus motif, *Neuron* *18*, 691-696.
- [72] Jia, L., Bonaventura, C., Bonaventura, J., and Stamler, J. S. (1996) S-nitrosohaemoglobin: a dynamic activity of blood involved in vascular control, *Nature* *380*, 221-226.
- [73] Gow, A. J., and Stamler, J. S. (1998) Reactions between nitric oxide and haemoglobin under physiological conditions, *Nature* *391*, 169-173.
- [74] Arnold, W. P., Mittal, C. K., Katsuki, S., and Murad, F. (1977) Nitric oxide activates guanylate cyclase and increases guanosine 3':5'-cyclic monophosphate levels in various tissue preparations, *Proc. Natl. Acad. Sci. USA* *74*, 3203-3207.
- [75] Bellamy, T. C., Wood, J., and Garthwaite, J. (2002) On the activation of soluble guanylyl cyclase by nitric oxide, *Proc. Natl. Acad. Sci. USA* *99*, 507-510.
- [76] Enemark, J. H., and Feltham, R. D. (1974) Principles of Structure, Bonding and Reactivity for Metal Nitrosyl Complexes, *Coord. Chem. Rev.* *13*, 339-406.
- [77] Sulc, F., Imoos, C. E., Pervitsky, D., and Farmer, P. J. (2004) Efficient trapping of HNO by deoxymyoglobin, *J. Am. Chem. Soc.* *126*, 1096-1101.
- [78] Hunt, A. P., and Lehnert, N. (2015) Heme nitrosyls: electronic structure implications for function in biology, *Acc. Chem. Res.* *48*, 2117-2125.
- [79] Wyllie, G. R. A., Schultz, C. E., and Scheidt, W. R. (2003) Five- to six-coordination in (nitrosyl)iron(II) porphyrinates: effects of binding the sixth ligand, *Inorg. Chem.* *42*, 5722-5734.
- [80] Praneeth, V. K. K., Neese, F., and Lehnert, N. (2005) Spin density distribution in five- and six-coordinate iron(II)-porphyrin NO complexes evidenced by magnetic circular dichroism spectroscopy, *Inorg. Chem.* *44*, 2570-2572.

[81] Amanullah, S., Saha, P., Saha, R., and Dey, A. (2019) Synthetic iron porphyrins for probing the differences in the electronic structures of heme  $a_3$ , heme  $d$ , and heme  $d_1$  *Inorg. Chem.* 58, 152-164.

## Chapter 2

# Trapping of a putative intermediate in the cytochrome *c* nitrite reductase (ccNiR)-catalyzed reduction of nitrite: implications for the ccNiR reaction mechanism

### 2.1. Overview

As mentioned in Chapter 1 it had long been assumed that ccNiR-catalyzed nitrite reduction invariably proceeds in one step to generate ammonia exclusively. This assumption was based on assessment of the standard ccNiR assay, which uses the strong reductant methyl viologen monocation radical as the electron source; in this assay reduction of nitrite to ammonia does indeed proceed in one six-electron step, without detection of any intermediates.<sup>1, 2</sup> However, the results presented in this chapter will demonstrate that it's possible to trap a putative ccNiR catalytic intermediate by using more weakly reducing conditions than are available when using methyl viologen monocation radical. The possible mechanistic implications of these results are considered.

### 2.2. Experimental Procedures

**2.2.1. General Materials.** Reagents were obtained from Fisher Scientific, Acros Organics or Sigma-Aldrich, unless specified otherwise, and used without additional purification. The pH-jump activated NO· precursor 1-(*N*, *N*-diethylamino) diazene-1-ium-1,2-diolate (DEANO) was prepared as described by Drago and Paulik.<sup>3, 4</sup>

**2.2.2. Protein purification and handling.** *S. oneidensis* ccNiR was purified from a high yield expression system using a protocol described previously,<sup>5</sup> but with one modification. After ammonium sulfate fractionation of the cell lysate, followed by hydrophobic interaction and anion-exchange chromatographies at pH 7 (ccNiR is un-retained in the anion-exchange step), the sample was equilibrated in 20 mM bis-tris pH 6.5 and loaded onto a SP-Sepharose cation exchange column (GE), to which ccNiR bound. The ccNiR was then eluted with a 20 mM HEPES pH 7 buffer, and shown to be of high purity by SDS PAGE gel electrophoresis (Appendix A). The pure protein was stored in aliquots at  $-80^{\circ}$  C.

**2.2.3. General instrumentation.** Routine and time-resolved UV/vis spectra were obtained using one of three Cary 50 (Varian) spectrophotometers. Two of these spectrophotometers are housed in nitrogen-filled anaerobic gloveboxes for obtaining spectra of air-sensitive samples. UV/Vis and EPR spectropotentiometric experiments were carried out in the gloveboxes using BASi Epsilon EC potentiostats to set the appropriate potential. An Ag/AgCl electrode was used as a reference (BASi model RE-5B), and was periodically standardized by comparison with the methyl viologen couple ( $\varepsilon_m^{\circ} = -0.449$  V vs. the standard hydrogen electrode, SHE).<sup>7</sup>

**2.2.4. UV/Visible spectropotentiometric titrations of ccNiR.** UV/Visible spectropotentiometry experiments were performed using a BASi Epsilon EC potentiostat to set the potential, and one of the glovebox-housed spectrophotometers to obtain the spectra at each applied potential. Controlled potential electrolysis of each solution was performed in an optically transparent thin-layer electrode cell similar to one used in earlier work by this group,<sup>5</sup> and elsewhere.<sup>8,9</sup> A solution containing ccNiR (50 – 70  $\mu$ M protomer),<sup>10</sup> varying concentrations of nitrite, and 100  $\mu$ M of the redox mediator 1,2-naphthoquinone-4-sulfonic acid ( $\varepsilon_m^{\circ} = 168$  mV

vs SHE, and negligible absorbance in the visible range {Appendix A}), was prepared in an appropriate buffer that also contained 200 mM NaCl, and was adjusted to the desired pH. A 50 mM HEPES buffer was used for pH 7.0, and a 50 mM tris buffer for pH 8.0. UV/Visible spectra in the range 300 – 800 nm were collected at 10 mV intervals between +160 mV and +300 mV vs. SHE, after it was clear that the spectral changes of interest occurred in this potential range.<sup>6</sup> The data sets were analyzed using programs written within the commercially available software package Mathcad 15 (PTC Software). Data analysis broadly followed the methodology used previously by this group;<sup>5</sup> details specific to this work are provided in the Results, and Appendix A.

**2.2.5. Time-resolved Reduction of nitrite-loaded ccNiR by *N, N, N', N'*-tetramethyl-*p*-phenylenediamine.** Initially ccNiR and *N,N,N',N'*-tetramethyl-*p*-phenylenediamine (TMPD) were mixed anaerobically into a solution of 50 mM HEPES buffer, pH 7, with a total volume of 974  $\mu$ L, such that the ccNiR and TMPD concentrations would come to  $\sim$ 10  $\mu$ M and  $\sim$ 1 mM, respectively, when diluted to 1 mL. The solution was monitored by UV/Vis spectroscopy at 30 s intervals for 5 min using one of the glovebox-housed spectrophotometers, after which a 26  $\mu$ L aliquot of nitrite stock was added to the reaction mixture, giving a solution containing 1 mM nitrite. The full reaction mixture was then monitored by UV/Vis spectroscopy every 30 s for another 20 min. The time-resolved data were analyzed using a previously described global fitting routine written within the commercially available software package Mathcad 15 (PTC Software).<sup>11, 12</sup>

**2.2.6. Electron paramagnetic resonance (EPR) analysis of ccNiR.** All experiments were carried out in 50 mM HEPES buffer, pH 7, which also contained 200 mM NaCl for electrochemical experiments. Typical ccNiR concentrations for EPR experiments were

50 – 60  $\mu\text{M}$ ;<sup>10</sup> 1,2-naphthoquinone-4-sulfonic acid (100  $\mu\text{M}$ ) was used as the mediator when enzyme reduction was required. For EPR analysis of the 2-electron reduced nitrite-loaded ccNiR the samples were prepared in a glovebox using a bulk electrolysis cell with platinum mesh as the working electrode. In a typical experiment 4 mL of ccNiR solution were added to the bulk electrolysis cell, and a potential of 160 mV vs SHE was applied for approximately 3 min intervals with no stirring.<sup>13</sup> After each interval the solution was gently mixed by drawing it in and out of a plastic syringe three or four times through a 0.75 mm id PEEK tube. Reduction progress was assessed from the current measured at the end of each interval, and by periodically removing subsamples from the cell and checking their UV/Vis spectrum using a 0.02 cm demountable cuvette. When no further changes were detected in the current and UV/Vis spectrum, a 250  $\mu\text{l}$  subsample was removed from the electrolysis cell and transferred into an EPR tube. The EPR tube was then placed into a test tube, which was stoppered with a butyl rubber stopper, removed from the glove box, and immediately submerged in liquid nitrogen. Samples were subsequently stored at  $-80\text{ }^\circ\text{C}$  until needed; they were kept on dry ice during transportation to the EPR facility.

EPR spectroscopy was carried out at 9.47 GHz on a Bruker EMX-TDU/L E4002501 spectrometer equipped with E532LX digital acquisition, an ER4112 SHQ resonator, a Cold-Edge/Bruker ER4112HV-S5-L Stinger cryogen-free 5–100 K closed cycle helium cryocooler, an HP 5350B microwave counter, and an Oxford Instruments ESR900 cryostat and Mercury-ITC temperature controller. Spectra were typically recorded at 10 K, 5.2 milliwatts of microwave power, 12 G (1.2 mT) magnetic field modulation amplitude at 100 kHz, and 1.2 G (0.12 mT) digital field resolution. Other acquisition parameters were chosen such that the spectral resolution was limited by the modulation amplitude. Background signals were recorded on a

frozen water sample and subtracted (Xepr) following field adjustment for precise microwave frequency.

## 2.3. Results

### 2.3.1. Effect of nitrite on the electrochemical properties of *S. oneidensis* ccNiR.

Figure 2.1 shows the UV/Visible spectral changes observed upon decreasing the potential applied to a solution initially containing 76  $\mu\text{M}$  of fully oxidized ccNiR, 100  $\mu\text{M}$  1,2-naphthoquinone-4-sulfonic acid and 5 mM nitrite.<sup>10</sup> The absorbance increase at 424 nm and decrease at 402 nm are typical of low-spin ferric *c*-heme reduction;<sup>14, 15</sup> however, the increases ca. 525 nm and 550 nm that are also characteristic of low-spin ferric *c*-heme reduction are absent, and a single broad increase centered at 555 nm is seen instead. Slices taken in the applied potential domain (Fig. 2.1b) clearly show a reduction event centered near 240 mV vs SHE. This is much higher than the midpoint potential obtained for the first reduction step of *S. oneidensis* ccNiR in the absence of strong-field ligands, and much higher even than that obtained in the presence of the strong-field ligand cyanide (20 mV vs NHE).<sup>16</sup> Singular value decomposition (SVD) analysis,<sup>16-18</sup> and the presence of tight isosbestic points at 341 nm and 415.5 nm in Fig. 2.1a, reveal only a single spectral component attributable to *c*-heme reduction.

The Fig. 2.1 data were well fit with a single Nernstian equation (Scheme 2.1, Eq. 1), in which  $\Delta A_{\lambda, \varepsilon_{app}}$  is the absorbance change observed at wavelength  $\lambda$  upon application of potential  $\varepsilon_{app}$ ,  $\varepsilon_m^0$  is the midpoint potential associated with the reduction event,  $\Delta A_{max(\lambda)}$  is the limiting absorbance change at wavelength  $\lambda$  observed at sufficiently low applied potentials, and  $n$  is the number of electrons transferred in the Nernstian step. In Eq. 2.1  $\varepsilon_{app}$  and  $\Delta A_{\lambda, \varepsilon_{app}}$  are the

independent and dependent variables, respectively, while  $\varepsilon_m^0$  and  $\Delta A_{\max(\lambda)}$  are parameters obtained by non-linear least-squares fitting of the Fig. 2.1 data set. The fitting process was performed twice, once with  $n$  fixed at 1, and the second time with  $n$  fixed at 2.

$$C_{ox} + ne^- \longrightarrow C_{red}$$

$$\Delta A_{\lambda, \varepsilon_{app}} = \frac{\Delta A_{\max(\lambda)} \cdot \exp\left[\frac{nF}{RT}(\varepsilon_m^0 - \varepsilon_{app})\right]}{1 + \exp\left[\frac{nF}{RT}(\varepsilon_m^0 - \varepsilon_{app})\right]} \quad \text{Eq. 2.1}$$

**Scheme 2.1.** Nernst equation used to fit the Fig. 2.1 data. Here  $C_{ox}$  refers to fully oxidized ccNiR, and  $C_{red}$  to the enzyme after a single reduction by  $n$  electrons. The remaining parameters are as defined in the main text.

From the least-squares fit the midpoint potential was calculated to be  $\varepsilon_m^0 = 0.246$  V, and the number of electrons transferred was  $n = 2$ . The latter is unusual given that in all previous studies ccNiR heme reductions invariably proceeded via one-electron steps ( $n = 1$  in Eq. 2.1);<sup>16</sup> however, the least-squares fit with  $n$  fixed at 2 (red trace in Fig. 2.1b) is clearly superior to that obtained with  $n$  fixed at 1 (dotted green trace in Fig. 2.1b).

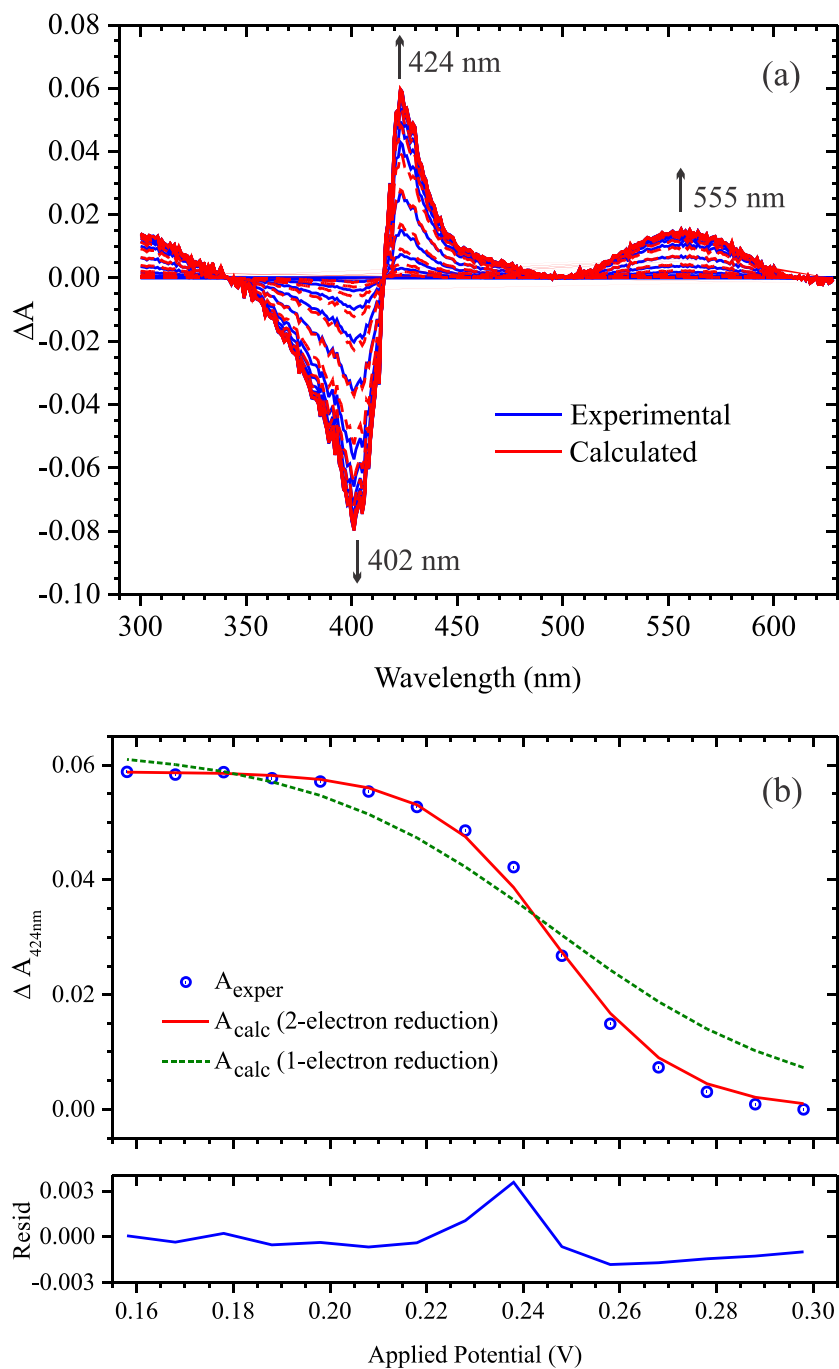
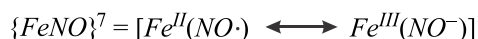
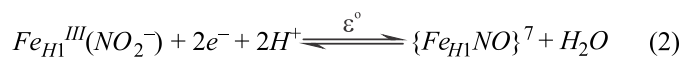
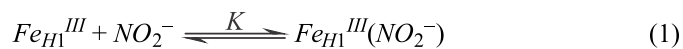


**Figure 2.1.** (a) UV/Vis spectral changes obtained upon exposing a solution initially containing  $76 \mu\text{M}$  of fully oxidized ccNiR,  $100 \mu\text{M}$  1,2-naphthoquinone-4-sulfonic acid and  $5 \text{ mM}$  nitrite to progressively lower potentials.<sup>10</sup> Solid blue lines show the experimentally obtained data, whereas the dashed red lines were calculated from least-squares fitting with a Nernstian 2-electron reduction and one spectral component (Scheme 2.1 and Appendix A). The fit yields a midpoint potential of  $\varepsilon_m^o = 0.246 \text{ V}$ . (b) Blue circles: an absorbance difference vs. applied potential slice taken at 424 nm from the spectra of part (a); solid red line: least-squares best fit obtained from global analysis of the data with  $n$  fixed at 2 electrons transferred in the Nernstian equation; dotted green line: same as the red line, but with  $n$  fixed at 1 electron transferred in the Nernstian equation.

Scheme 2.2 provides a chemical interpretation for the two-electron reduction seen in Fig. 2.1. In the first step of Scheme 2.2 nitrite binds to the ccNiR heme 1 active site. Using the binding constant  $K = (5.0 \pm 0.1) \times 10^3 \text{ M}^{-1}$  obtained from independent EPR experiments<sup>6</sup> one can estimate that, in the presence of 5 mM nitrite, the heme 1 active site will be ~96% occupied in the fully oxidized enzyme. Two-electron reduction of the nitrite-loaded active site will then give a species formally referred to as  $\{\text{FeNO}\}$ <sup>7</sup> using the Enemark-Feltham notation (see Section 1.4.2).<sup>19</sup> The parameter  $\varepsilon^o$  associated with step 2 of Scheme 2.2 represents the true standard reduction potential for the process. Thus it appears that, when nitrite is bound at the ccNiR active site, the first enzyme reduction event proceeds via a concerted 2-electron process that to some extent distributes the electrons between the iron and nitrogen moieties (Scheme 2.2).

Scheme 2.2 predicts that the apparent midpoint potential  $\varepsilon_m^o$  measured by using the empirical Scheme 2.1 Nernst equation should be pH-dependent, shifting  $-59 \text{ mV}$  per pH unit at  $25^\circ \text{ C}$  (Appendix A). In two spectropotentiometric titrations carried out at pH 8 instead of pH 7 the observed midpoint potential for ccNiR 2-electron reduction was  $0.207 \pm 0.002 \text{ V}$ , a negative shift of  $39 \text{ mV}$  from the value obtained at pH 7. This is less than the predicted shift, but a significant shift nonetheless. Scheme 2.2 also predicts that the apparent midpoint potential obtained by fitting spectropotentiometric data with the empirical Nernstian of Scheme 2.1 should decrease if the nitrite concentration is lowered to the point where a significant fraction of the ccNiR active sites are vacant instead of nitrite-loaded. The relationship between  $\varepsilon_m^o$  and nitrite concentration is complex, but it can be readily modeled theoretically by combining the equilibrium expression associated with nitrite binding to heme 1 with the Nernst equation 2.1 (Appendix A). The relationship depends on the two parameters shown in Scheme 2.2: the standard reduction potential  $\varepsilon^o$  (adjusted for pH), and the binding constant  $K$ .



**Scheme 2.2.** Chemical interpretation of the nitrite-loaded ccNiR 2-electron reduction.  $Fe_{H1}$  represents the active site heme center in various states of oxidation and ligation; see text for details.

Figure 2.2 shows how the apparent midpoint potential varies with nitrite concentration. The blue circles show the experimental data obtained with the empirical Nernst equation (Scheme 2.1 Eq. 2.1), while the red squares show the theoretical values calculated as described in Appendix A. The theoretical calculations assumed a standard reduction potential  $\varepsilon^o$  of 0.246 V, which is the  $\varepsilon_m^o$  value obtained at pH 7 using Eq. 2.1, when most of the heme 1 sites were nitrite-occupied (5 – 20 mM nitrite). However, to obtain the red square data, the value of  $K$  was treated as an adjustable parameter in a least-squares fitting routine. The fitting routine yielded the best fit with  $K = 2600 \text{ M}^{-1}$ . This value is about half that obtained from EPR titrations of *S. oneidensis* ccNiR,<sup>6</sup> but close to the value obtained by Lockwood et al. for *E. coli* ccNiR ( $2500 \pm 300 \text{ M}^{-1}$ ).<sup>20</sup> Moreover, given the scatter in the Fig. 2.2 data, and the small range within which  $\varepsilon_m^o$  changes with nitrite concentration, even the agreement with the EPR titration of the *S. oneidensis* enzyme is reasonable. Indeed, modelling the Fig. 2.2 data with  $K$  fixed at  $5000 \text{ M}^{-1}$ , the value obtained by EPR,<sup>6</sup> shifts the calculated  $\varepsilon_m^o$  values at each nitrite concentration by at most 7 mV, and generates a theoretical curve that retains the shape of the one obtained by least-squares fit (Fig. 2.2, green triangles). For completeness Fig. 2.2 also shows a curve obtained by fixing  $K$  at  $1400 \text{ M}^{-1}$  (purple diamonds), which gave the same sum of squares as obtained with  $K = 5000 \text{ M}^{-1}$ .

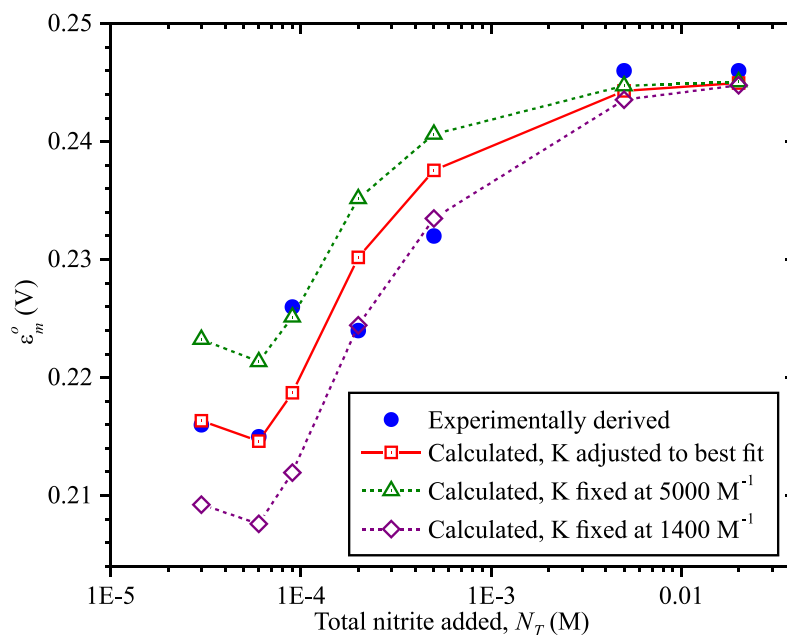


**Figure 2.2.** Blue circles: dependence on nitrite concentration of the apparent midpoint potential obtained by fitting UV/Vis spectropotentiometric data to the empirical Nernst equation (Scheme 2.1, Eq. 2.1). Red squares, green triangles and purple diamonds: predicted values of the apparent midpoint potential at a given nitrite concentration, calculated as described in Appendix A, using  $\varepsilon^o = 0.246$  V; the red square values were obtained by varying  $K$  to yield the least-squares best fit ( $K = 2600$   $\text{M}^{-1}$ ), while the green triangle values were obtained with  $K$  fixed at  $5000$   $\text{M}^{-1}$ , and the purple diamond values with  $K$  fixed at  $1400$   $\text{M}^{-1}$  (see text for details).

Again the shape of the curve is similar to that of the least-squares fit. Together, the green and purple curves provide a measure of the sensitivity of the fits to the  $K$  value. Most importantly, the midpoint potential calculated using the empirical Nernst equation 2.1 is seen to vary as predicted theoretically when the nitrite concentration decreases to the point where a significant fraction of the ccNiR active sites are vacant. Finally it is important to note that, in the absence of a strong field ligand such as nitrite, none of the ccNiR hemes reduce at applied potentials greater than 0 V vs SHE,<sup>5, 16</sup> so only nitrite-loaded ccNiR can reduce at the high potentials monitored in these experiments.

**2.3.2. Reduction of nitrite-loaded *S. oneidensis* ccNiR by *N, N, N', N'*-tetramethyl-*p*-phenylenediamine.** The blue traces in Fig. 2.3a show the UV/Vis spectral changes observed after mixing *S. oneidensis* ccNiR with large excesses of nitrite, and the weak reductant *N,N,N',N'*-tetramethyl-*p*-phenylenediamine (TMPD,  $\varepsilon_m^o = 260$  mV vs SHE), at pH 7. Initially ccNiR and 1 mM TMPD were mixed into a solution with a total volume of 974  $\mu$ L. The green trace in Fig. 2.3a shows the UV/Vis spectrum of this solution, scaled for future dilution to 1 mL. The purple dotted trace that overlays the green one was obtained by least-squares fitting of the green trace with the independently obtained extinction coefficient spectrum of oxidized ccNiR. The fit shows that the solution, once diluted to 1 mL, would contain 11  $\mu$ M of fully oxidized ccNiR. The ccNiR-TMPD solution was monitored by UV/Vis at 30 s intervals for 5 min and remained unchanged. After 5 min a 26  $\mu$ L aliquot of nitrite stock was added to the reaction mixture, giving a solution containing 1 mM nitrite. The first blue trace above the green one was obtained within 30 s of adding the nitrite and was set as the  $t = 0$  spectrum. Subsequently spectra were collected every 30 s, but for clarity the blue traces in Fig 2.3a are at 120 s intervals; Figure 2.3b shows an absorbance vs time slice taken at 611 nm. SVD analysis<sup>17, 18</sup> showed that only two components were needed to faithfully reconstruct a noise-reduced absorbance matrix. The SVD-treated data were then fit to Eq. 2.2 using a global fitting routine (red traces, Fig. 2.3a).<sup>11, 12</sup>

$$A_{\lambda,t} = \Lambda_{0(\lambda)} + \Lambda_{1(\lambda)}(t + q \cdot t^2) \quad \text{Eq. 2.2}$$

In Eq. 2.2  $A_{\lambda,t}$  is the absorbance obtained at wavelength  $\lambda$  and time  $t$ , the spectral component  $\Lambda_0$  is present immediately after adding nitrite (taken as  $t = 0$ ), and component  $\Lambda_1$  grows in almost linearly with time (the manually-adjusted parameter  $q$  in Eq. 4 allows small admixture, 0.016%, of a quadratic term that improves the empirical fit).

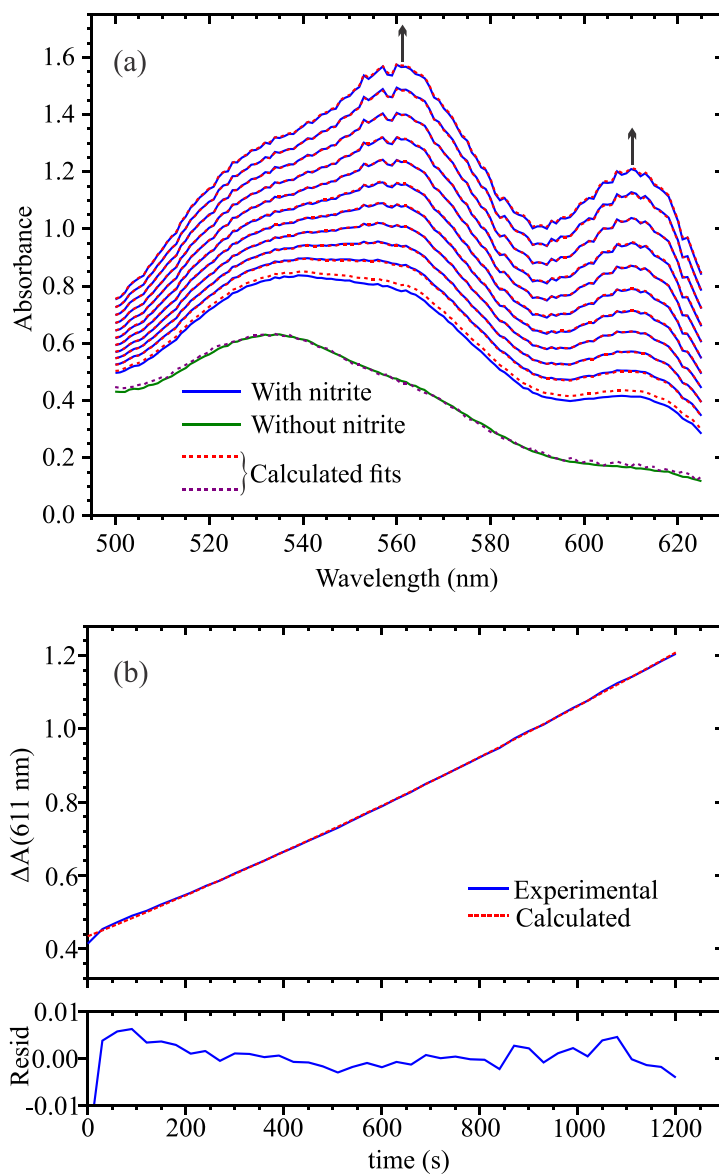


**Figure 2.3.** (a) Blue traces: spectral changes seen at 120 s intervals after mixing 11  $\mu\text{M}$  oxidized ccNiR with 1 mM each of nitrite and TMPD. Red dashed traces: least-squares best fits using Eq. 2.2. Green trace: spectrum of the solution containing 11  $\mu\text{M}$  oxidized ccNiR and 1 mM TMPD, but prior to addition of nitrite; purple dashed trace: least-squares best fit obtained with the independently known oxidized ccNiR extinction coefficient spectrum. (b) Absorbance vs. time slice from the Fig. 2.3a spectrum, obtained at 611 nm.

Figure 2.4 shows the spectral components obtained from the fitting process. The component  $\Lambda_0$  (Fig. 2.4a) was in its turn fit with the extinction coefficient spectrum of reduced

nitrite-loaded ccNiR (obtained from spectropotentiometric titrations, as described in Appendix A), and that of the blue  $\text{TMPD}^+$  radical.<sup>21</sup> The fit shows that immediately after mixing the solution contained 11.0  $\mu\text{M}$  reduced ccNiR and 22.1  $\mu\text{M}$   $\text{TMPD}^+$ , a ratio of 2.03  $\text{TMPD}^+$ :1 ccNiR. This experiment thus provides independent confirmation that, under weakly reducing conditions, nitrite-loaded ccNiR is reduced in a concerted 2-electron process as proposed in Scheme 2.2; in the present case the two electrons are supplied by two equivalents of TMPD.

The spectral component  $\Lambda_1$  that grows in approximately linearly (Fig. 2.4b) was fit with the extinction coefficient spectrum of the  $\text{TMPD}^+$  radical,<sup>21</sup> and shows that TMPD continued to oxidize at a rate of  $\sim 4.3 \times 10^{-8} \text{ Ms}^{-1}$  after the initial oxidation burst. In separate studies (chapter 3) we have found that ccNiR catalyzes the 1-electron reduction of nitrite to nitric oxide by weak reductants such as ferrocyanide, TMPD and  $\text{Ru}(\text{NH}_3)_6^{2+}$ . CcNiR-catalyzed 1-electron reduction of nitrite to nitric oxide will be the topic of Chapter 3; for the moment one need note only that TMPD oxidation during the linear phase is quite slow compared to that associated with the initial reduction of  $\text{Fe}_{\text{HI}}^{\text{III}}(\text{NO}_2^-)$  to  $\{\text{Fe}_{\text{HI}}\text{NO}\}^7$ , allowing the two processes to be readily deconvoluted by conventional time-resolved spectroscopy. Thus, Figs. 2.3 and 2.4 show that ccNiR-catalyzed reduction of free nitrite by TMPD yields  $\sim 1.3 \mu\text{M}$   $\text{TMPD}^+$  in the first 30 s after reaction initiation, during which time reduction of  $\text{Fe}_{\text{HI}}^{\text{III}}(\text{NO}_2^-)$  to  $\{\text{Fe}_{\text{HI}}\text{NO}\}^7$ , which generates  $\sim 22 \mu\text{M}$   $\text{TMPD}^+$ , is virtually complete. Preliminary stopped-flow data show that the half-life for  $\{\text{Fe}_{\text{HI}}\text{NO}\}^7$  formation is about 6 s (data not shown).

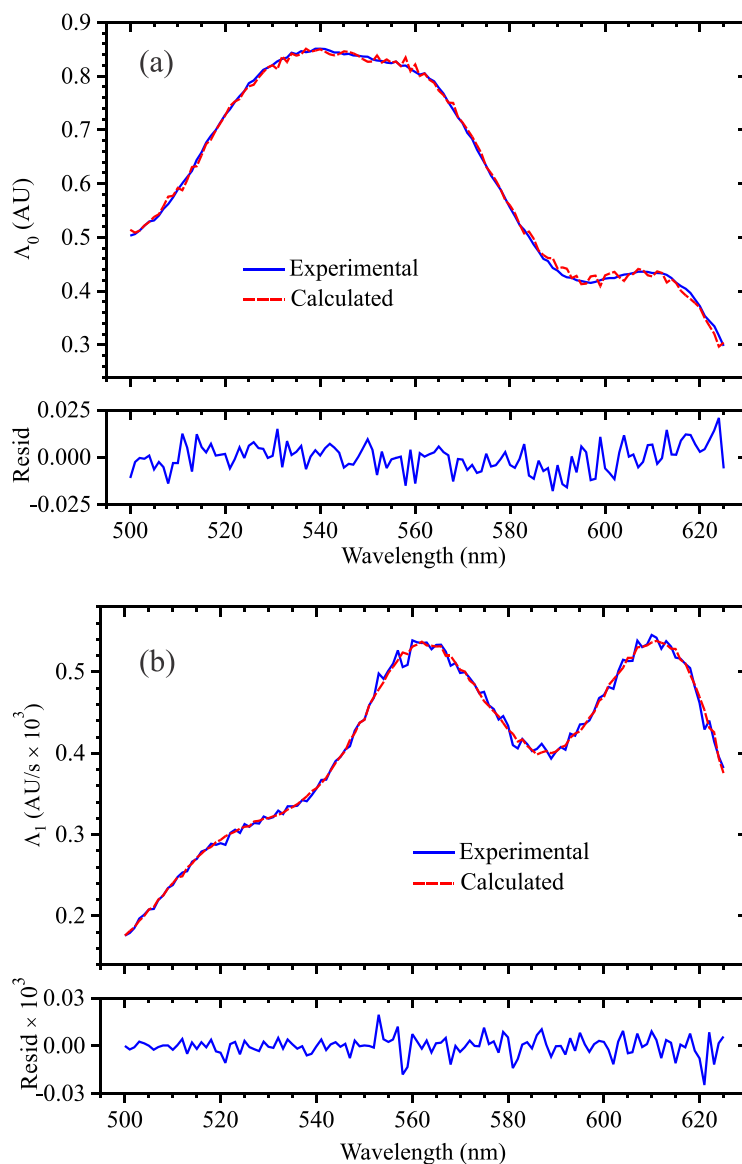


**Figure 2.4.** Spectral components  $\Lambda_0$  (a) and  $\Lambda_1$  (b) generated by fitting the SVD-processed Fig. 2.3 data to Eq. 2.2 (blue traces).  $\Lambda_0$  was in turn fit with the extinction coefficient spectra of reduced nitrite-loaded ccNiR (obtained as described in Appendix A), and of the blue  $\text{TMPD}^+$  radical,<sup>21</sup> while  $\Lambda_1$  was fit using only the  $\text{TMPD}^+$  extinction coefficient spectrum. The red dashed traces show the calculated spectra in each case.

### 2.3.3. Investigation of the *S. oneidensis* ccNiR {Fe<sub>H1</sub>NO}<sup>7</sup> moiety by EPR

**spectroscopy.** To generate ccNiR containing the {Fe<sub>H1</sub>NO}<sup>7</sup> active site for characterization by EPR, a sample was prepared by poisoning the enzyme at 160 mV vs SHE in the presence of a large excess of nitrite. EPR spectroscopy subsequently revealed two hitherto unobserved sets of features (Fig. 2.5). The first set exhibited turning points at  $g = 2.18, 2.12$  and  $2.05$ , with a resolved inflection on the crossover feature and a "truncated" trough feature at  $g = 2.05$ . The overall line shape was evocative of a low-spin  $S = \frac{1}{2}$  {FeNO}<sup>7</sup> species, but the  $g$ -values and spectral envelope width were not quite consistent with literature values.<sup>22-27</sup> Interpretation was further complicated by the presence of an equally broad overlapping signal, clearly of different origin, that was observed without poisoning the potential (Fig. 2.5, top), and by a sharp feature at  $g = 2.0$ . Attempts to detect <sup>14</sup>N<sub>I=1</sub> superhyperfine splittings using lower modulation amplitude (5 G, 0.5 mT) and higher derivatives were unconvincing. Samples were generated using <sup>15</sup>NO<sub>2</sub><sup>-</sup> in an attempt to at least detect differences in the  $g \sim 2$  region due to the differences in  $\mu_N$  (<sup>15</sup>N > <sup>14</sup>N) and the line multiplicity [ $2$  (<sup>15</sup>N<sub>I=1/2</sub>) vs.  $3$  (<sup>14</sup>N<sub>I=1</sub>)], but the <sup>14</sup>NO and <sup>15</sup>NO spectra were indistinguishable within the signal-to-noise obtainable with 64  $\mu$ M ccNiR (Fig. 2.5, bottom). Spin integration showed that the  $g = 2.2 - 2.0$  region contributes a substantial fraction to the total spin envelope, at least twice that contributed by the rhombic heme 2 signal (Appendix A). We conjecture that the  $g = 2.2 - 2.0$  features arise from the low-spin {FeNO}<sup>7</sup> active site interacting magnetically with nearby hemes, which would explain why they are atypical. To our knowledge there has been only one prior report of heme-heme magnetic interaction that involved an {FeNO}<sup>7</sup> species;<sup>28</sup> however, such an interaction in ccNiR is plausible given that the active site is known to interact with heme 3, and possibly also heme 4, in the resting enzyme.<sup>2, 16, 20, 29, 30</sup>

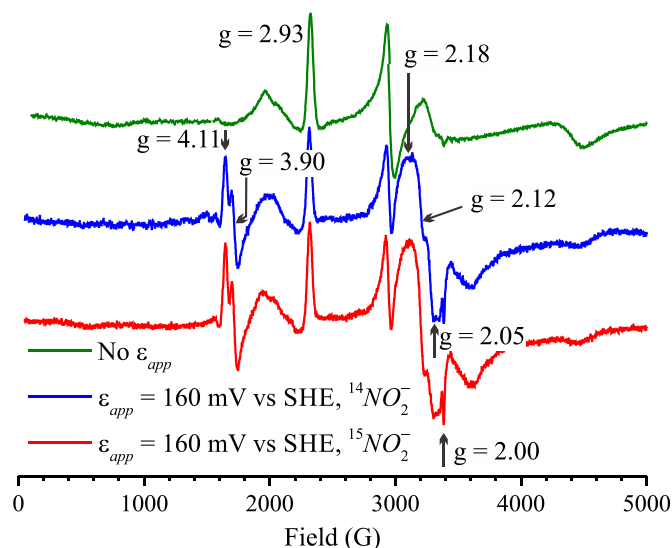


**Figure 2.5.** Green trace: X-band EPR spectrum obtained for fully oxidized ccNiR in the presence of 5 mM nitrite. Blue trace: spectrum obtained for a solution initially containing 64  $\mu\text{M}$  of fully oxidized ccNiR and 500  $\mu\text{M}$   $^{14}\text{NO}_2^-$ , after exposing it to an applied potential of 160 mV vs SHE.<sup>10</sup> Red trace: same as blue trace, but using 500  $\mu\text{M}$   $^{15}\text{NO}_2^-$ .

The second set of features that appears with 2-electron reduction of nitrite-loaded ccNiR is far easier to assign. The co-appearance of a sharp peak with  $g' = 4.1$ ,<sup>31</sup> a sharp crossover at  $g' = 3.9$ , and a sharp inverted peak at  $g' = 2.0$  (Fig. 2.5 middle and bottom spectra) are diagnostic for the  $M_S = \pm 1/2$  doublet of an  $S = 3/2$  spin system with  $|D| \gg g\mu_B B_0 S$ , and a very small rhombic zero-field splitting ( $E/D \approx 0.015$ ). This signal was observed with multiple batches of ccNiR, using concentrations of nitrite from 500  $\mu\text{M}$  – 5 mM and, in each case, the intensity of the  $S = 3/2$  signal measured by EPR correlated with the extent of heme *c* (i.e. heme 1) reduction determined by electronic absorption spectrophotometry. Under conditions of maximum expression, the  $S = 3/2$  signal's contribution to the spin envelope is approximately 20% that of the rhombic heme 2 signal (Appendix A). The only plausible origin for a signal of this type in the ccNiR preparations is a high-spin  $\{\text{FeNO}\}^7$  system, likely arising predominantly from antiferromagnetic coupling of high-spin ferric iron to a bound triplet-state  $\text{NO}^-$  moiety,<sup>22, 32</sup> though the rhombicity allows for some ( $S = 2, \text{Fe}^{II}$ )–( $S = 1/2, \text{NO}\cdot$ ) character.<sup>33</sup> Such species are relatively common in both protein

complexes and model compounds, but only in non-heme iron systems. As mentioned above, all known hemoprotein {FeNO}<sup>7</sup> complexes are low-spin with  $S = 1/2$ , and are generally described as predominantly low-spin ferroheme ( $S = 0$ ) with  $S = 1/2$  NO· bound.<sup>22-27, 34-37</sup>

Upadhyay et al. reported an  $S = 3/2$  {FeNO}<sup>7</sup> signal in the EPR spectrum of the tetraheme protein cytochrome *c*<sub>554</sub> when this was nitrosylated and 2-electron reduced,<sup>28</sup> but attributed it to a minority non-heme impurity in their preparations. The  $S = 3/2$  signals in Fig. 2.5 may also be due to a non-heme impurity, but two considerations argue against such an assignment. First, SDS-PAGE analysis showed that the ccNiR used in the EPR experiments was of very high purity (Appendix A), making it unlikely that the  $S = 3/2$  signal arises from a non-heme protein. The  $S = 3/2$  {FeNO}<sup>7</sup> signal could still arise from adventitious iron in the preparation. To test for this possibility a ccNiR sample identical to the ones used to generate the Fig. 2.5 spectra but containing 25 μM Cu<sup>2+</sup> as internal standard, was subjected to ultrafiltration to generate a protein-free filtrate. The filtrate was then treated with enough of the NO· precursor DEANO to add 60 μM NO· to the solution, after which it was immediately reduced electrochemically at an applied potential of 160 mV vs SHE. EPR analysis of the oxidized and reduced filtrates showed that the total adventitious iron in the preparations was minimal compared to the Cu<sup>2+</sup> internal standard (~0.7%), and that the  $S = 3/2$  {FeNO}<sup>7</sup> signal arising from the filtrate was substantially smaller than that seen in the ccNiR-containing precursor samples (Appendix A). It is still possible that the  $S = 3/2$  {FeNO}<sup>7</sup> signal associated with the ccNiR-containing sample arises from adventitious iron strongly adsorbed to the protein, though there is no evidence of such iron in a high-resolution *S. oneidensis* ccNiR crystal structure obtained independently.<sup>6</sup>

## 2.4. Discussion

**2.4.1. Behavior of nitrite-loaded ccNiR under weakly reducing conditions.** The UV/Vis spectropotentiometric results of this study (Figs. 2.1 and 2.2) show that, when occupied with nitrite, initial reduction of the ccNiR active site occurs by a concerted 2-electron process, which thus generates an  $\{\text{FeNO}\}^7$  moiety (Scheme 2.2). The stoichiometry of the reduction was independently verified in a time-resolved UV/Vis spectroscopy experiment that tracked reduction of the nitrite-loaded heme 1 active site by the weak reductant TMPD, which generates blue  $\text{TMPD}^+$  upon oxidation (Figs. 2.3 and 2.4). This experiment clearly showed that two equivalents of TMPD were oxidized for every equivalent of nitrite-loaded ccNiR that was reduced. The TMPD experiment, together with other experiments that used ferrocyanide and  $\text{Ru}(\text{NH}_3)_6^{2+}$  electron donors (Chapter 3), also showed that ccNiR catalyzes nitrite reduction to nitric oxide when weak reductants are used. However,  $\text{NO}\cdot$  formation is very slow when compared to the initial 2-electron reduction of  $\text{Fe}_{\text{H1}}^{\text{III}}(\text{NO}_2^-)$  to  $\{\text{Fe}_{\text{H1}}\text{NO}\}^7$ , so the two processes are readily deconvoluted (Figs. 2.3 and 2.4).

EPR characterization of the 2-electron reduced nitrite-loaded active site subsequently showed it to possess a novel spectral signature that is different from those normally observed for  $\{\text{FeNO}\}^7$  hemes (Fig. 2.5). Such hemes are typically low-spin  $S = 1/2$ , with spin density mainly on the nitrogen. They have very characteristic features in the  $g \sim 2.0 - g \sim 2.1$  range, which usually display at least some degree of hyperfine interaction with the  $^{14}\text{NO}$  or  $^{15}\text{NO}$  nitrogen.<sup>22-27</sup> The spectra for reduced ccNiR in Fig 2.5 show prominent features in the  $g \sim 2.0 - g \sim 2.2$  range, but these look different from the usual low-spin  $\{\text{FeNO}\}^7$  heme features, and are not affected by isotopic exchange from  $^{14}\text{N}$  to  $^{15}\text{N}$ . The features have the right intensities to arise from the low-spin  $\{\text{Fe}_{\text{H1}}\text{NO}\}^7$  active site interacting magnetically with nearby hemes (Appendix A), and this

makes a plausible working hypothesis that has a precedent.<sup>28</sup> Further testing of this hypothesis will require extensive EPR studies of nitrite-loaded reduced ccNiR at varying temperatures and applied frequencies, possibly buttressed by computational analysis and application of other spectroscopic techniques such as Mössbauer. Such studies are beyond the scope of this report, but are planned for the future.

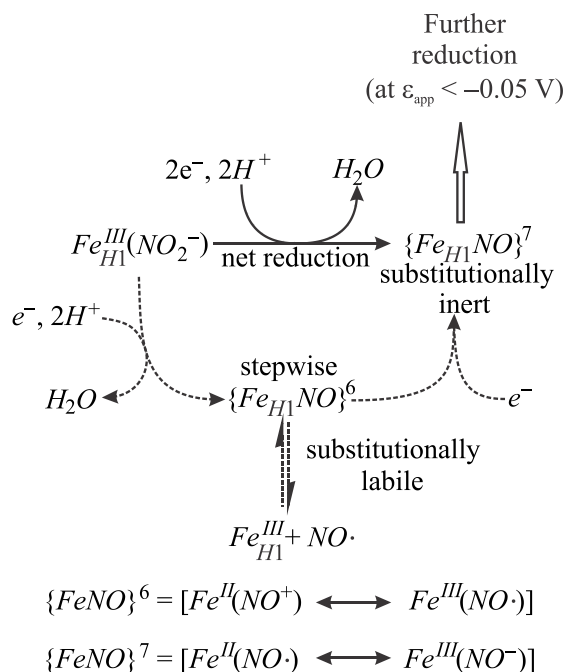
The EPR spectrum of 2-electron reduced nitrite-loaded ccNiR also revealed signals characteristic of a high-spin  $S = 3/2$  {FeNO}<sup>7</sup> species. The signal has an intensity approximately 20% that of ccNiR heme 2 (Appendix A) and might be dismissed as arising from non-heme impurities, except that such an explanation seems inconsistent with the high purity of the samples used in the EPR experiments. SDS-PAGE showed that non-ccNiR protein contaminants were less than 5%, and spin quantitation of the protein-free reaction medium showed that the adventitious iron concentration was similarly low (Appendix A). Based on these considerations we don't yet discount the possibility that the high-spin  $S = 3/2$  {FeNO}<sup>7</sup> signal actually arises from a small fraction of the ccNiR population in which the active sites have a slightly different heme environment from that of the majority. An  $S = 3/2$  {FeNO}<sup>7</sup> heme would be unprecedented in heme chemistry, and more studies will be needed to explore this possibility. However, there is some independent evidence that 2-electron reduced nitrite-loaded ccNiR can exist in a variety of forms, depending on conditions, as will now be explained.

The earliest spectropotentiometric investigation of nitrite-loaded ccNiR performed in the Pacheco laboratory gave results quite different from those obtained ever since. In this initial single study reduction of nitrite-loaded ccNiR still took place in a concerted 2-electron step, but the observed midpoint potential was 20 mV vs SHE instead of 246 mV.<sup>6</sup> Furthermore, the EPR spectrum of the reduced protein also looked different.<sup>6</sup> This spectrum showed a peak feature at

$g = 2.08$  and a broad trough with  $g \sim 1.9 - 2.04$ , which together are much more like a typical  $S = \frac{1}{2} \{FeNO\}^7$  signal than the features seen ever since for the *S. oneidensis* ccNiR. There was only one immediately identifiable difference between the preliminary experiment and all subsequent ones. The ccNiR used in the early experiment was purified by the method of Youngblut et al, in which the final chromatographic step was hydrophobic interaction chromatography with a high-performance column at pH 7.<sup>5</sup> In every experiment since then the ccNiR was purified as described in the *Experimental Procedures* section, whereby the final step involved cation exchange chromatography at pH 6.5. The ccNiR purified by the two methods was otherwise indistinguishable in its properties. In particular both methods yielded ccNiR whose electrochemical properties were comparable in the presence of the strong-field ligand cyanide, and that had comparable  $k_{cat}$  and  $K_m$  values in the standard assay (ccNiR-catalyzed reduction of nitrite by methyl viologen monocation radical; Chapter 4). Furthermore, the crystal structure of the enzyme purified by the method described herein shows no obvious differences from the structure obtained with the earlier purification protocol.<sup>5, 6</sup> It thus seems that ccNiR can possibly exist in two very closely related forms that nevertheless exhibit significantly different heme 1 electrochemical properties in the presence of nitrite. To further probe this conjecture a batch of ccNiR was purified using the earlier protocol,<sup>5</sup> in which the protein was never exposed to a pH below 7, to see if the putative alternate form could be re-isolated. However, in this case the ccNiR purified using the earlier protocol exhibited the same electrochemical properties in the presence of excess nitrite that have been observed ever since, namely a midpoint potential of  $\sim 240$  mV vs SHE. Thus, for now, we have no obvious explanation for our one anomalous early result.

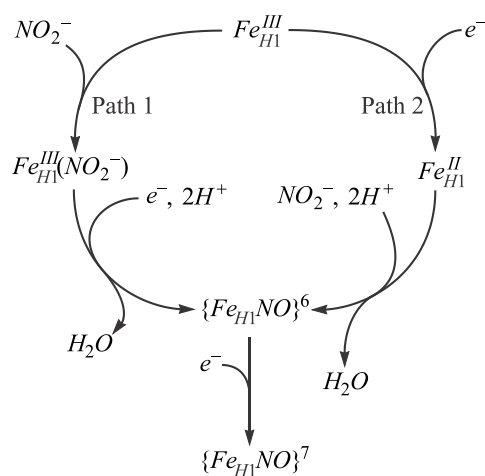
**2.4.2. Implications of the results for the ccNiR reaction mechanism.** Physically, a concerted 2-electron reduction indicates that addition of a second electron to a redox-active center is much more favorable than addition of the first. Under these circumstances, applying a potential low enough to prompt the first reduction step simultaneously initiates the second step as well. In the case of ccNiR, 1-electron reduction of the  $\text{Fe}_{\text{H1}}^{\text{III}}(\text{NO}_2^-)$  active site would yield the species referred to as  $\{\text{Fe}_{\text{H1}}\text{NO}\}^6$ , which represents resonance forms of a moiety that formally has  $\text{NO}\cdot$  bound to  $\text{Fe}^{\text{III}}$ , or  $\text{NO}^+$  bound to  $\text{Fe}^{\text{II}}$  (dashed arrow, Scheme 2.3).<sup>19</sup> Ostensibly 1-electron reduction of the  $\text{Fe}_{\text{H1}}^{\text{III}}(\text{NO}_2^-)$  active site to  $\{\text{Fe}_{\text{H1}}\text{NO}\}^6$  is more thermodynamically difficult than the subsequent reduction of  $\{\text{Fe}_{\text{H1}}\text{NO}\}^6$  to  $\{\text{Fe}_{\text{H1}}\text{NO}\}^7$ , so the intermediate  $\{\text{Fe}_{\text{H1}}\text{NO}\}^6$  doesn't accumulate, and  $\text{Fe}_{\text{H1}}^{\text{III}}(\text{NO}_2^-)$  appears to reduce directly to  $\{\text{Fe}_{\text{H1}}\text{NO}\}^7$  as shown by the solid arrow in Scheme 2.3.

Evolution of ccNiR so that it reduces bound nitrite in a 2-electron process makes sense from a physiological standpoint. Extensive studies with both model and hemoprotein systems have shown that  $\text{NO}\cdot$  typically binds more tightly within  $\{\text{FeNO}\}^7$  species when compared to  $\{\text{FeNO}\}^6$  species.<sup>37-42</sup> Thus, by disfavoring the  $\{\text{FeNO}\}^6$  intermediate, the ccNiR design ensures that release of toxic  $\text{NO}\cdot$  is kept to a minimum during catalytic turnover. The experiment with TMPD (Figs. 2.3 and 2.4), and similar ones that used the weak reductants  $\text{Fe}(\text{CN})_6^{4-}$  or  $\text{Ru}(\text{NH}_3)_6^{2+}$ , highlight this point. With any of these reductants the rate of  $\text{NO}\cdot$  generation was found to be  $\sim 10 - 15 \mu\text{M}/\text{h}$  per  $1 \mu\text{M}$  ccNiR, which is very slow (Chapter 3). For comparison,  $k_{\text{cat}}$  for ccNiR-catalyzed reduction of nitrite to ammonia by methyl viologen monocation radical is  $\sim 800 \text{ s}^{-1}$  in the standard ccNiR assay, which uses picomolar quantities of ccNiR.<sup>5</sup>



**Scheme 2.3.** Here  $Fe_{H1}$  represents the active site heme center in various states of oxidation and ligation. The solid arrows show the net reduction observed experimentally, while the dashed ones show the steps that likely underlie the observed process; see text for details.

The conditions employed in this study, whereby the oxidized active site was first saturated with millimolar concentrations of nitrite and then reduced, are unlikely to prevail under the physiological conditions most favorable for ammonia production. Instead, active site reduction likely precedes nitrite binding *in vivo*.<sup>43, 44</sup> As a strong  $\pi$ -acceptor, nitrite will bind much more strongly to the electron-rich ferrous active site, thus allowing the site to be fully occupied at much lower concentrations. The relative order of nitrite and electron addition, however, will not affect the thermodynamic conclusions made above, as shown in Scheme 2.4. In either case  $NO\cdot$  release from substitutionally labile  $\{Fe_{H1}NO\}^6$  will be minimized if the standard reduction potential for reduction of  $\{Fe_{H1}NO\}^6$  to  $\{Fe_{H1}NO\}^7$  is much higher than that for reduction of  $Fe_{H1}^{III}(NO_2^-)$  to  $\{Fe_{H1}NO\}^6$ , so that the labile species can't accumulate.



**Scheme 2.4.** In the experiments described herein active site reduction in the presence of nitrite appears to proceed via Path 1. Under physiological conditions it will likely proceed via Path 2. In either case free  $NO\cdot$  release from substitutionally labile  $\{Fe_{H1}NO\}^6$  will be minimized if the standard reduction potential for reduction of  $\{Fe_{H1}NO\}^6$  to  $\{Fe_{H1}NO\}^7$  is much higher than that for reduction of  $Fe_{H1}^{III}(NO_2^-)$  to  $\{Fe_{H1}NO\}^6$ .

Computational studies described in previous reports predicted that a  $\{Fe_{H1}NO\}^7$  active site will constitute a thermodynamic minimum in ccNiR.<sup>43, 45, 46</sup> This in turn led to the suggestion that  $\{Fe_{H1}NO\}^7$  constitutes a kinetic trap that sits off of the reaction pathway from nitrite to ammonia, and to suggestions for how the species could be bypassed during catalysis.<sup>43, 45</sup> The present results confirm that  $\{Fe_{H1}NO\}^7$  at the active site constitutes a thermodynamic minimum, but in no way rule out its possible role as a catalytic intermediate, based on the following analysis that is represented schematically in Fig. 2.6. The standard free energy  $\Delta G^\circ$  for reduction of free nitrite to ammonia at pH 7 by a standard hydrogen electrode can be calculated to be a highly favorable  $\sim -200$  kJ/mol (Fig. 2.6).<sup>47, 48</sup> Thus, at an applied potential of 0 mV vs SHE, thermodynamics predict that nitrite reduction to ammonia should be almost quantitative. The results of the present study show that initial nitrite reduction at the active site can occur at applied potentials as high as 240 mV vs SHE, but that at these high potentials only  $\{Fe_{H1}NO\}^7$  is generated. In other preliminary spectropotentiometric studies we have seen no

further reduction of  $\{\text{Fe}_{\text{HI}}\text{NO}\}^7$  until  $\varepsilon_{\text{app}}$  reaches  $\sim -80$  mV vs SHE.<sup>6, 49</sup> Furthermore, protein film voltammetry (PFV) experiments used to probe the catalytic reduction of nitrite to ammonia by electrode-adsorbed *S. oneidensis* ccNiR have shown that no significant catalytic ammonia formation occurs at potentials above  $-120$  mV vs SHE.<sup>50, 51</sup> If an applied potential of  $0$  mV vs SHE is theoretically low enough to reduce free nitrite to ammonia, then the additional  $120$  mV overpotential required for turnover in the PFV experiments could well be needed to extricate  $\{\text{Fe}_{\text{HI}}\text{NO}\}^7$  from its thermodynamically stable hole, as shown schematically in Fig. 2.6.

The stability of  $\{\text{Fe}_{\text{HI}}\text{NO}\}^7$  may not be the only barrier to ultimate formation of ammonia. Earlier rapid-mixing experiments also revealed a kinetic barrier to the final 2-electron reduction of hydroxylamine to ammonia, by demonstrating that ccNiR cannot catalyze the disproportionation of hydroxylamine to ammonia and nitrite.<sup>52</sup> In this disproportionation the reductive half reaction is highly favorable thermodynamically, and should drive the much less favorable oxidative one. Yet in the rapid mixing studies *no* ammonia was ever produced, while the ccNiR hemes could readily accept electrons from hydroxylamine to generate small amounts of nitrite and heme-bound nitrogenous species.<sup>52</sup> It appears that a kinetic barrier to hydroxylamine reduction can only be overcome by applying an overpotential greater than can be supplied by hydroxylamine oxidation, so disproportionation does not occur.<sup>52</sup>

Based on the combined results of the present study, and the earlier rapid-mixing and PFV investigations,<sup>50-52</sup> we propose that the rate-limiting step for ccNiR-catalyzed reduction of nitrite to ammonia is the final 2-electron reduction of hydroxylamine (or a heme-bound hydroxylamine equivalent, Fig. 2.6),<sup>52</sup> and that this step requires a strong reducing agent to overcome it. The hypothesis is consistent with the fact that the  $k_{\text{cat}}$  value, as measured in electrons transferred per

second, is the same for nitrite and hydroxylamine reduction to ammonia, when methyl viologen monocation radical is the electron source.<sup>5</sup>

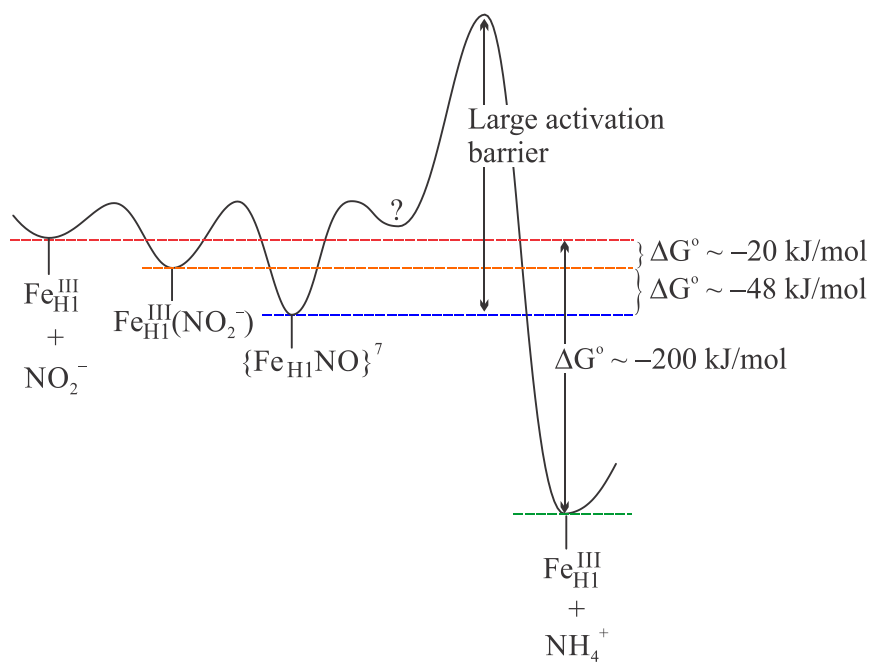


**Figure 2.6.** Cartoon representation of the ccNiR-catalyzed nitrite reduction reaction path, proposed on the basis of the results reported herein. The standard free energies are per mole of product formed, and where applicable, are calculated relative to the standard hydrogen electrode. The question mark denotes an as-yet uncharacterized putative 4-electron reduced intermediate, for which there is some preliminary evidence.<sup>52</sup> We propose that weak reductants can't provide the overpotential necessary to overcome the depicted high activation barrier, thus allowing intermediates to accumulate. Only when a strong reductant such as methyl viologen monocation radical is used does nitrite get reduced directly to ammonia, without accumulation of detectable intermediates.

The hypothesis that the final 2-electron reduction is rate-limiting suggests new considerations for ccNiR design parameters. To begin with, avoiding  $\{Fe_{HI}NO\}^7$  as a thermodynamic trap becomes less important; a reductant strong enough to reduce ccNiR-bound hydroxylamine (or its equivalent) will also be strong enough to reduce the  $\{Fe_{HI}NO\}^7$  intermediate. On the other hand, the hypothesis upends the long-held assumption that ccNiR always catalyzes reduction of nitrite directly to ammonia, without generation of intermediates.

While this may be true in the presence of strong reductants such as methyl viologen monocation radical, it is clearly not true under less strongly reducing conditions, whereby the barrier to hydroxylamine reduction can't be overcome. This is why the  $\{\text{Fe}_{\text{HI}}\text{NO}\}^7$  intermediate could be so readily characterized herein.

CcNiR's ability to capture nitrite as  $\{\text{Fe}_{\text{HI}}\text{NO}\}^7$  under weakly reducing conditions may be physiologically important for facultative anaerobes such as *S. oneidensis*. In such bacteria the periplasm can go from being a reducing environment to being an oxidizing one as the bacteria move from anaerobic to aerobic surroundings.<sup>53</sup> Unlike in *E. coli*, in *S. oneidensis* multi-heme proteins such as ccNiR are expressed under both aerobic and anaerobic conditions, and it's possible that ccNiR has evolved to capture and hold partially reduced nitrite products rather than to release them, when full reduction to ammonia is not possible. For example, as discussed above, the  $\{\text{Fe}_{\text{HI}}\text{NO}\}^7$  moiety would be an effective intermediate for capturing nitrite at high potentials, while minimizing release of  $\text{NO}\cdot$ . Under more reducing conditions that nevertheless fail to provide the overpotential needed for hydroxylamine reduction, other adaptations may help to minimize escape of hydroxylamine or nitrous oxide, two other nitrogenous intermediates that could be generated by ccNiR;<sup>52, 54</sup> future studies to explore this possibility are planned.

**2.4.3. Summary.** Spectropotentiometric and time-resolved UV/Vis experiments have shown that nitrite-loaded *S. oneidensis* ccNiR can be reduced at high applied potential in a concerted 2-electron step to generate an  $\{\text{FeNO}\}^7$  moiety at the heme 1 active site. EPR spectropotentiometry subsequently revealed that the  $\{\text{Fe}_{\text{HI}}\text{NO}\}^7$  moiety possesses an unusual spectral signature that is different from those normally observed for  $\{\text{FeNO}\}^7$  hemes, and may indicate magnetic interaction of the active site with nearby hemes. The simplest hypothesis

consistent with the results presented herein is that an  $\{\text{Fe}_{\text{HI}}\text{NO}\}^7$  moiety is a catalytic intermediate in the ccNiR-mediated reduction of nitrite to ammonia (Fig. 2.6), whose degree of accumulation depends exclusively on the applied potential. At low potentials the species is rapidly reduced and doesn't accumulate, while at higher potentials it is trapped, thus stalling catalytic ammonia formation. The  $\{\text{Fe}_{\text{HI}}\text{NO}\}^7$  species may be the first of a number of ccNiR catalytic intermediates that can be isolated simply by tuning the applied potential. Earlier rapid-mixing studies of ccNiR-hydroxylamine mixtures also hinted at various species that are formally four-electron reduced relative to the resting enzyme (represented by a question mark in Fig. 2.6), and that may accumulate at applied potentials between  $-80$  mV and  $-120$  mV.<sup>49, 52</sup> Experiments are under way to further characterize these four-electron reduced species. Future studies will also need to explore the structural basis for the very high midpoint potential of the nitrite-loaded heme 1 active site, as well as for its unusual spectroscopic properties.

Finally it should be noted that, while the present study shows the first step in ccNiR-catalyzed nitrite reduction to be a concerted 2-electron process, earlier PFV experiments that probed electrocatalytic nitrite reduction by electrode-absorbed *S. oneidensis* ccNiR consistently showed the rate-limiting step to be a one-electron event.<sup>50, 51</sup> This apparent discrepancy illustrates the complementary nature of the PFV and spectropotentiometric approaches. While in the former case steady-state electrocatalysis is monitored, here the initial redox events associated with heme spectral changes are examined. Thus, in pre-steady-state conditions, two-electron redox chemistry appears essential to poise the active site, while subsequent one-electron transfer steps may ultimately control the rate of catalytic ammonia formation.

## 2.5. References

- [1] Einsle, O., Messerschmidt, A., Stach, P., Bourenkov, G. P., Bartunik, H. D., Huber, R., and Kroneck, P. M. H. (1999) Structure of cytochrome c nitrite reductase, *Nature* *400*, 476-480.
- [2] Bamford, V. A., Angove, H. C., Seward, H. E., Thomson, A. J., Cole, J. A., Butt, J. N., Hemmings, A. M., and Richardson, D. J. (2002) Structure and spectroscopy of the periplasmic cytochrome c nitrite reductase from *Escherichia coli*, *Biochemistry* *41*, 2921-2931.
- [3] Drago, R. S., and Paulik, F. E. (1960) The Reaction of Nitrogen (II) Oxide with Diethylamine, *J. Am. Chem. Soc.* *82*, 96-98.
- [4] Maragos, C. M., Morley, D., Wink, D. A., Dunams, T. M., Saavedra, J. E., Hoffman, A., Bove, A. A., Isaac, L., Hrabie, J. A., and Keefer, L. K. (1991) Complexes of NO with Nucleophiles as Agents for the Controlled Biological Release of Nitric-Oxide - Vasorelaxant Effects, *J. Med. Chem.* *34*, 3242-3247.
- [5] Youngblut, M., Judd, E. T., Srajer, V., Sayyed, B., Goelzer, T., Elliott, S. J., Schmidt, M., and Pacheco, A. A. (2012) Laue crystal structure of *Shewanella oneidensis* cytochrome c nitrite reductase from a high-yield expression system, *J. Biol. Inorg. Chem.* *17*, 647-662.
- [6] Ali, M., Stein, N., Mao, Y., Shahid, S., Schmidt, M., Bennett, B., and Pacheco, A. A. (2019) Trapping of a putative intermediate in the cytochrome c nitrite reductase (ccNiR)-catalyzed reduction of nitrite: implications for the ccNiR reaction mechanism *J. Am. Chem. Soc.* *141*, 13358-13371.
- [7] Watanabe, T., and Honda, K. (1982) Measurement of the extinction coefficient of the methyl viologen cation radical and the efficiency of its formation by semiconductor photocatalysis, *J. Phys. Chem.* *86*, 2617-2619.
- [8] Heineman, W. R., Norris, B. J., and Goelz, J. F. (1975) Measurement of enzyme  $E^0$  values by optically transparent thin layer electrochemical cells, *Anal. Chem.* *47*, 79-84.
- [9] Pilkington, M. B. G., Coles, B. A., and Compton, R. G. (1989) Construction of an optically transparent thin layer electrode cell for use with oxygen-sensitive species in aqueous and non-aqueous solvents, *Anal. Chem.* *61*, 1787-1789.
- [10] To clarify: the concentration of ccNiR protomers is reported herein; the concentration of the full enzyme dimer will be half of the reported protomer concentration.

- [11] Koebke, K. J., Pauly, D. J., Lerner, L., Liu, X., and Pacheco, A. A. (2013) Does the oxidation of nitric oxide by oxymyoglobin share an intermediate with the metmyoglobin-catalyzed isomerization of peroxynitrite?, *Inorg. Chem.* 52, 7623-7632.
- [12] Koebke, K. J., Waletzko, M. T., and Pacheco, A. A. (2016) Direct monitoring of the reaction between photochemically generated nitric oxide and *Mycobacterium tuberculosis* truncated hemoglobin N wild type and variant forms: an assessment of computational mechanistic predictions, *Biochemistry* 55, 686-696.
- [13] Stirring the solution while applying a potential promoted release of nitric oxide from the active site, as evidenced by the persistence of a high background current ( $> 100 \mu\text{A}$ ), and low accumulation of reduced ccNiR as monitored by UV/Vis spectroscopy. CcNiR's ability to catalyze slow reduction of nitrite to nitric oxide under weakly reducing conditions is briefly discussed herein, and will be more extensively covered in a separate article.
- [14] Arciero, D. M., Collins, M. J., Haladjian, J., Bianco, P., and Hooper, A. B. (1991) Resolution of the 4 Hemes of Cytochrome-C554 from *Nitrosomonas-Europaea* by Redox Potentiometry and Optical Spectroscopy, *Biochemistry* 30, 11459-11465.
- [15] Marritt, S. J., Kemp, G. L., Xiaoe, L., Durrant, J. R., Cheesman, M. R., and Butt, J. N. (2008) Spectroelectrochemical characterization of a pentaheme cytochrome in solution and as electrocatalytically active films on nanocrystalline metal-oxide electrodes, *J. Am. Chem. Soc.* 130, 8588-8589.
- [16] Stein, N., Love, D., Judd, E. T., Elliott, S. J., Bennett, B., and Pacheco, A. A. (2015) Correlations between the electronic properties of *Shewanella oneidensis* cytochrome *c* nitrite reductase (ccNiR) and its structure: effects of heme oxidation state and active site ligation, *Biochemistry* 54, 3749-3758.
- [17] Press, W. H., Teukolsky, S. A., Vetterling, W. T., and Flannery, B. P. (2007) Numerical Recipes the art of scientific computing, 3rd ed., pp 65-75, Cambridge University Press, New York, NY.
- [18] Henry, E. R., and Hofrichter, J. (1992) Singular Value Decomposition: Application to Analysis of Experimental Data, In *Meth. Enzymol.* (Brand, L., and Johnson, M. L., Eds.), pp 129-192, Academic Press, San Diego.

- [19] Enemark, J. H., and Feltham, R. D. (1974) Principles of Structure, Bonding and Reactivity for Metal Nitrosyl Complexes, *Coord. Chem. Rev.* *13*, 339-406.
- [20] Lockwood, C. W. J., Burlat, B., Cheesman, M. R., Kern, M., Simon, J., Clarke, T., Richardson, D. J., and Butt, J. N. (2015) Resolution of key roles for the distal pocket histidine in cytochrome *c* nitrite reductases, *J. Am. Chem. Soc.* *137*, 3059-3068.
- [21] Albrecht, A. C., and Simpson, W. T. (1955) Spectroscopic study of Wurster's Blue and tetramethyl-*p*-phenylenediamine with assignments of electronic transitions, *J. Am. Chem. Soc.* *77*, 4454-4461.
- [22] Westcott, B. L., and Enemark, J. H. (1999) Transition Metal Nitrosyls, In *Inorganic Electronic Structure and Spectroscopy* (Solomon, E. I., and Lever, A. B. P., Eds.), pp 435-439, John Wiley and Sons, Inc., New York, NY.
- [23] Nasri, H., Ellison, M. K., Chen, S., Huynh, B. H., and Scheidt, W. R. (1997) Sharing the  $\pi$ -bonding. An iron porphyrin derivative with trans  $\pi$ -accepting axial ligands. Synthesis, EPR and Mossbauer spectra, and molecular structure of two forms of the complex nitronitrosyl( $\alpha,\alpha,\alpha,\alpha$ -tetrakis(*o*-pivalamidophenyl)-porphinato)ferrate(II), *J. Am. Chem. Soc.* *119*, 6274-6283.
- [24] Wayland, B. B., and Olson, L. W. (1974) Spectroscopic studies and bonding model for nitric oxide complexes of iron porphyrins, *J. Am. Chem. Soc.* *96*, 6037-6041.
- [25] Stach, P., Einsle, O., Schumacher, W., Kurun, E., and Kroneck, P. M. H. (2000) Bacterial cytochrome *c* nitrite reductase: new structural and functional aspects, *J. Inorg. Biochem.* *79*, 381-385.
- [26] Hendrich, M. P., Upadhyay, A. K., Riga, J., Arciero, D. M., and Hooper, A. B. (2002) Spectroscopic characterization of the NO adduct of hydroxylamine oxidoreductase, *Biochemistry* *41*, 4603-4611.
- [27] Amanullah, S., Saha, P., Saha, R., and Dey, A. (2019) Synthetic iron porphyrins for probing the differences in the electronic structures of heme *a*<sub>3</sub>, heme *d*, and heme *d*<sub>1</sub> *Inorg. Chem.* *58*, 152-164.
- [28] Upadhyay, A. K., Hooper, A. B., and Hendrich, M. P. (2006) NO reductase activity of the tetraheme cytochrome *c*(554) of *Nitrosomonas europaea*, *J. Am. Chem. Soc.* *128*, 4330-4337.

- [29] Clarke, T. A., Kemp, G. L., Van Wonderen, J. H., Doyle, R. A. S., Cole, J. A., Tovell, N., Cheesman, M. R., Butt, J. N., Richardson, D. J., and Hemmings, A. M. (2008) Role of a conserved glutamine residue in tuning the catalytic activity of *Escherichia coli* Cytochrome *c* nitrite reductase, *Biochemistry* 47, 3789-3799.
- [30] Kemp, G. L., Clarke, T. A., Marritt, S. J., Lockwood, C., Poock, S. R., Hemmings, A. M., Richardson, D. J., Cheesman, M. R., and Butt, J. N. (2010) Kinetic and thermodynamic resolution of the interactions between sulfite and the pentahaem cytochrome NrfA from *Escherichia coli*, *Biochem. J.* 431, 73-80.
- [31]  $g'$  is the experimentally-observed resonance position where  $g' = h\nu/\mu_B B_0$ , and is distinct from  $g$ , the spin-Hamiltonian spectroscopic parameter.
- [32] Brown, G. C. (1995) Reversible Binding and Inhibition of Catalase by Nitric-Oxide, *Eur. J. Biochem.* 232, 188-191.
- [33] Jackson, T. A., Yikilmaz, E., Miller, A.-F., and Brunold, T. C. (2003) Spectroscopic and computational study of a non-heme iron  $\{\text{FeNO}\}^7$  system: exploring geometric and electronic structures of the nitrosyl adduct of iron superoxide dismutase, *J. Am. Chem. Soc.* 125, 8348-8363.
- [34] Berto, T. C., Praneeth, V. K. K., Goodrich, L. E., and Lehnert, N. (2009) Iron-porphyrin NO complexes with covalently attached N-donor ligands: formation of a stable six-coordinate species in solution, *J. Am. Chem. Soc.* 131, 17116-17126.
- [35] Berto, T. C., Xu, N., Lee, S. R., McNeil, A. J., Alp, E. E., Zhao, J., Richter-Addo, G. B., and Lehnert, N. (2014) Characterization of the bridged hyponitrite complex  $\{[\text{Fe}(\text{OEP})]_2(\mu\text{-N}_2\text{O}_2)\}$ : reactivity of hyponitrite complexes and biological relevance, *Inorg. Chem.* 53, 6398-6414.
- [36] Smith, A. T., Pazicni, S., Marvin, K. A., Stevens, D. J., Paulsen, K. M., and Burstyn, J. N. (2015) Functional divergence of heme thiolate proteins: a classification based on spectroscopic attributes, *Chem. Rev.* 115, 2532-2558.
- [37] Hunt, A. P., and Lehnert, N. (2015) Heme nitrosyls: electronic structure implications for function in biology, *Acc. Chem. Res.* 48, 2117-2125.
- [38] Hoshino, M., Ozawa, K., Seki, H., and Ford, P. C. (1993) Photochemistry of Nitric-Oxide Adducts of Water-Soluble Iron(III) Porphyrin and Ferrihemoproteins Studied by Nanosecond Laser Photolysis, *J. Am. Chem. Soc.* 115, 9568-9575.

- [39] Bohle, S. D., and Hung, C.-H. (1995) Ligand-promoted rapid nitric oxide dissociation from ferrous porphyrin nitrosyls, *J. Am. Chem. Soc.* *117*, 9584-9585.
- [40] Ellison, M. K., and Scheidt, W. R. (1999) Synthesis, molecular structures, and properties of six-coordinate [Fe(OEP)(L)(NO)]<sup>+</sup> derivatives: Elusive nitrosyl ferric porphyrins, *J. Am. Chem. Soc.* *121*, 5210-5219.
- [41] Ford, P. C., and Lorkovic, I. M. (2002) Mechanistic aspects of the reactions of nitric oxide with transition-metal complexes, *Chem. Rev.* *102*, 993-1017.
- [42] Praneeth, V. K. K., Paulat, F., Berto, T. C., De Beer George, S., Nather, C., Sulok, C. D., and Lehnert, N. (2008) Electronic structure of six-coordinate iron(III) - porphyrin NO adducts: the elusive iron (III) - NO(radical) state and its influence on the properties of these complexes, *J. Am. Chem. Soc.* *130*, 15288-15303.
- [43] Einsle, O., Messerschmidt, A., Huber, R., Kroneck, P. M. H., and Neese, F. (2002) Mechanism of the six-electron reduction of nitrite to ammonia by cytochrome c nitrite reductase, *J. Am. Chem. Soc.* *124*, 11737-11745.
- [44] Bykov, D., and Neese, F. (2011) Substrate binding and activation in the active site of cytochrome *c* nitrite reductase: a density functional study, *J. Biol. Inorg. Chem* *16*, 417-430.
- [45] Bykov, D., and Neese, F. (2012) Reductive activation of the heme iron-nitrosyl intermediate in the reaction mechanism of cytochrome *c* nitrite reductase: a theoretical study, *J. Biol. Inorg. Chem.* *17*, 741-760.
- [46] Bykov, D., and Neese, F. (2015) Six-electron reduction of nitrite to ammonia by cytochrome *c* nitrite reductase: insights from density functional theory studies, *Inorg. Chem.* *54*, 9303-9316.
- [47] Atkins, P., Overton, T., Rourke, J., Weller, M., Armstrong, F., and Hagerman, M. (2010) Shriver & Atkins' Inorganic Chemistry, 5th ed., pp 147-178, W. H. Freeman and Co., New York, NY.
- [48] Kostera, J., McGarry, J. M., and Pacheco, A. A. (2010) Enzymatic Interconversion of Ammonia and Nitrite: the Right Tool for the Job, *Biochemistry* *49*, 8546-8553.
- [49] Stein, N. (2014) Spectroscopic and electrochemical studies of *Shewanella oneidensis* cytochrome *c* nitrite reductase, and improving *c*-heme expression systems, In *Chemistry*

*and Biochemistry*, University of Wisconsin-Milwaukee, Dept. of Chemistry and Biochemistry, Milwaukee, WI.

- [50] Judd, E. T., Youngblut, M., Pacheco, A. A., and Elliott, S. J. (2012) Direct Electrochemistry of *Shewanella oneidensis* Cytochrome *c* Nitrite Reductase: Evidence of Interactions across the Dimeric Interface, *Biochemistry* 51, 10175-10185.
- [51] Judd, E. T., Stein, N., Pacheco, A. A., and Elliott, S. J. (2014) Hydrogen bonding networks tune proton-coupled redox steps during the enzymatic six-electron conversion of nitrite to ammonia, *Biochemistry* 53, 5638-5646.
- [52] Youngblut, M., Pauly, D. J., Stein, N., Walters, D., Conrad, J. A., Moran, G. R., Bennett, B., and Pacheco, A. A. (2014) *Shewanella oneidensis* cytochrome *c* nitrite reductase (ccNiR) does not disproportionate hydroxylamine to ammonia and nitrite, despite a strongly favorable driving force., *Biochemistry* 53, 2136-2144.
- [53] Nicholls, D. G., and Ferguson, S. J. (2002) Bioenergetics 3, In *Bioenergetics 3*, pp 134-154, Academic Press, San Diego, CA.
- [54] Caranto, J. D., Vilbert, A. C., and Lancaster, K. M. (2016) *Nitrosomonas europaea* cytochrome P460 is a direct link between nitrification and nitrous oxide emission, *PNAS* 113, 14704-14709.

## Chapter 3

# A Mechanistic Study of CcNiR-catalyzed Reduction of Nitrite by Ferrocyanide

### 3.1. Overview

As was seen in Chapter 2, under weakly reducing conditions ccNiR is incapable of catalyzing nitrite reduction all the way to ammonia. Instead, at applied potentials greater than 0 V vs SHE one traps a catalytic intermediate that has an {FeNO}<sup>7</sup> active site.<sup>1</sup> Chapter 2 also mentioned in passing that ccNiR does catalyze very slow reduction of nitrite to nitric oxide by the weak reductant *N,N,N',N'*-tetramethyl-*p*-phenylenediamine. We have found that ccNiR will also catalyze 1-electron reduction of nitrite to nitric oxide by other weak reductants such as ferrocyanide and hexaamineruthenium(II). This chapter presents a kinetic study of ccNiR-catalyzed reduction of nitrite to nitric oxide by ferrocyanide (Scheme 3.1).



**Scheme 3.1.** CcNiR-catalyzed reduction of nitrite to NO· by ferrocyanide.

### 3.2. Experimental procedures

**3.2.1. General materials.** Sodium nitrite, potassium ferrocyanide (II) trihydrate, TrisHCl (99% extra pure) and BisTris (ultra-pure) were purchased from Acros Organics; Ammonium sulfate (AS) and HEPES free acid and sodium salt were obtained from fisher

scientific; EDTA disodium salt was bought from Sigma-Aldrich, Argon (high purity grade) from AirGas and liquid nitrogen. Wild type *S. oneidensis* ccNiR was purified as described in Chapter 2 and stored in aliquots at  $-80^{\circ}\text{C}$ .

**3.2.2. Catalase purification and handling.** Bovine liver catalase, originally purchased from Sigma-Aldrich, was purified by a previously described method,<sup>2</sup> then concentrated to 200  $\mu\text{M}$ . Catalase denatures upon freezing, so the following procedure was used to pass it into the glovebox. Purified catalase (0.5 mL) was placed in an open Eppendorf tube, which in turn was placed in a wide-mouth glass test tube. The test tube was sealed with a rubber septum through which two needles were inserted (caution- the septum must be firmly secured to the test tube so that it doesn't pop out when placed in the glovebox antechamber). One needle was connected to an argon line that supplied water-saturated argon and the second to a bubbler that opened to the atmosphere. To completely degas the catalase wet argon was run very gently over the solution for two hours. The degassed catalase was then brought into the glovebox and kept at  $4^{\circ}\text{C}$  in mini refrigerator.

**3.2.3. Buffer and stock solution preparation.** Buffers (50 mM) were prepared at pH intervals of 0.2 in the range from 6.2 – 8.8; all buffers contained 1 mM EDTA to act as a protease inhibitor. Buffers with pH 6.2 – 6.8 were prepared with Bis-Tris, those with pH 7.0 – 7.8 with HEPES, and those with pH 8.0 – 8.8 with Tris-HCl. Stock solutions of the appropriate buffer were prepared in 100 mL batches and then split into 25 mL aliquots, each of which was adjusted to a different pH by addition of HCl or NaOH: HCl was used for Bis-Tris, NaOH for HEPES and Tris-HCl. Each buffer was degassed by purging with argon for one hour, after which it was rapidly frozen with liquid nitrogen and brought through the antechamber frozen into

the glovebox. Once in the glovebox the buffer was allowed to thaw and come to room temperature before being used.

Stock solutions of 80  $\mu\text{M}$  of ccNiR were made in 50 mM HEPES buffer pH 7 that contained 1 mM EDTA. 1 M sodium nitrite, 1 M ammonium sulfate and 1 M potassium ferrocyanide were made by bringing an appropriate amount of the solid into the glovebox and then dissolving in the desired degassed buffer.

**3.2.4. Data Collection.** Time-resolved UV/Vis data were collected with a CARY Bio 50 UV-Vis spectrophotometer that was housed in an anaerobic glovebox (oxygen level  $<0.1$  ppm). All the reagents for a given experiment were thoroughly mixed in appropriate amounts in an Eppendorf tube, and then transferred into a 1 cm path length quartz cuvette as quickly as possible. The cuvette was then placed in the cuvette holder of the spectrophotometer and spectral data collection initiated. It typically took less than 1 minute from the start of mixing to the start of data collection. After data collection had been initiated the cuvette was stoppered to prevent  $\text{NO}\cdot$  escape and to keep diffusion of residual oxygen from the glovebox to a minimum. For each experiment UV-Vis spectra were collected every 15 seconds for an hour; in this time a total of 240 spectra were collected. The data sets were analyzed using programs written within the commercially available software packages Mathcad 15 (PTC Software) and Origin 9.1. Data analysis broadly followed the methodologies used previously by this group;<sup>3-7</sup> details specific to this work are provided in the Results section.

### 3.3. Results

**3.3.1. NO $\cdot$  trapping experiments.** The blue traces in Fig. 3.1a show the UV/Vis spectral changes with time that were observed in a pH 7 solution that initially contained 75 nM ccNiR, 4  $\mu$ M catalase, 2 mM nitrite, and 20 mM ferrocyanide. Spectra were collected every 15s for an hour, but for clarity Fig. 3.1a shows spectra only at 500s intervals. The blue trace in Fig. 3.1b shows an absorbance change vs time slice of the Fig. 3.1a spectra, obtained at 433 nm. Singular value decomposition (SVD) analysis,<sup>8,9</sup> and the presence of a well-defined isosbestic point at 418 nm, showed that a single spectral component was contributing to the changes. The SVD-treated data were fit to the empirical 2-exponential equation 3.1 (red traces, Fig 3.1), in which  $\Delta A_{\lambda,t}$  is the absorbance change seen at wavelength  $\lambda$  and time  $t$ ,  $A_{\lambda}$  is the limiting absorbance at wavelength  $\lambda$  that would be seen after infinite time,  $k_1$  and  $k_2$  are rate constants, and *frac* is a parameter with a value between zero and one. In Eq. 3.1  $\Delta A_{\lambda,t}$  and  $t$  are the dependent and independent variables, respectively, and  $k_1$ ,  $k_2$ , *frac* and  $A_{\lambda}$  are adjustable parameters obtained by a combination of linear and non-linear least-squares fitting of the Fig 3.1 data set.<sup>4-6</sup>

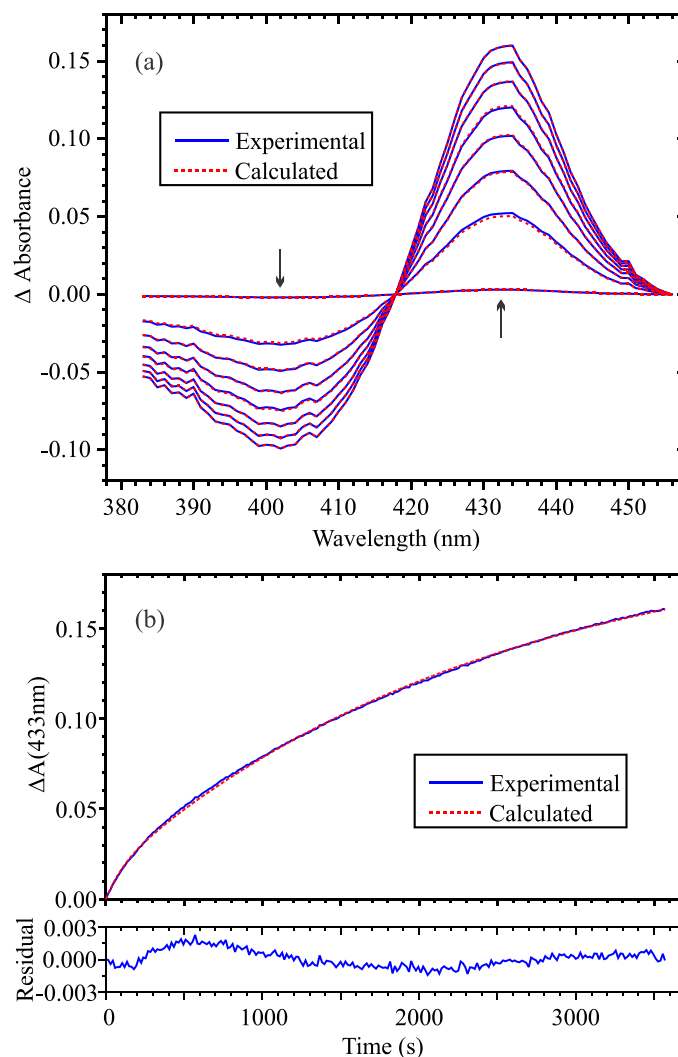


**Figure 3.1.** (a) Blue traces: spectral changes observed at 500 s intervals in a pH 7.0 solution initially containing 75 nM ccNiR, 4  $\mu$ M catalase, 2 mM nitrite and 20 mM ferrocyanide. Dashed red traces: least-squares best fits obtained using Eq. 3.1. (b) Absorbance vs time slice from the spectra in (a), obtained at 433 nm.

The blue trace in Fig. 3.2 shows the spectral component  $\Lambda$  obtained from fitting the Fig. 3.1 spectra to Eq. 3.1. This component was in turn fit with the independently obtained extinction coefficient difference spectrum  $\Delta\epsilon_{\text{CatNO}} = \epsilon_{\text{CatNO}} - \epsilon_{\text{Cat}}$ , where  $\epsilon_{\text{Cat}}$  and  $\epsilon_{\text{CatNO}}$  are the extinction coefficient spectra for catalase and nitrosylated catalase, respectively (red trace, Fig 3.2).<sup>2</sup> The excellent fit in Fig. 3.2 shows that the only contribution to the spectral changes seen in Fig. 3.1

came from nitrosylation of catalase. Catalase binds  $\text{NO}\cdot$  rapidly and tightly ( $k_{on} = 1.3 \times 10^7 \text{ M}^{-1}\text{s}^{-1}$ ,  $K = 8.7 \times 10^6 \text{ M}^{-1}$ ),<sup>2</sup> so the appearance of CatNO in the Fig 3.1 difference spectra tracks the generation of  $\text{NO}\cdot$  from nitrite in the reaction mixture. The initial rate of  $\text{NO}\cdot$  formation was determined from the value of the Eq. 3.1 derivative at time zero (Eq. 3.2). The value of the initial rate showed first-order dependence on catalase concentration, at least within the narrow range of catalase concentrations tested (0.7 – 5  $\mu\text{M}$ ; data not shown).

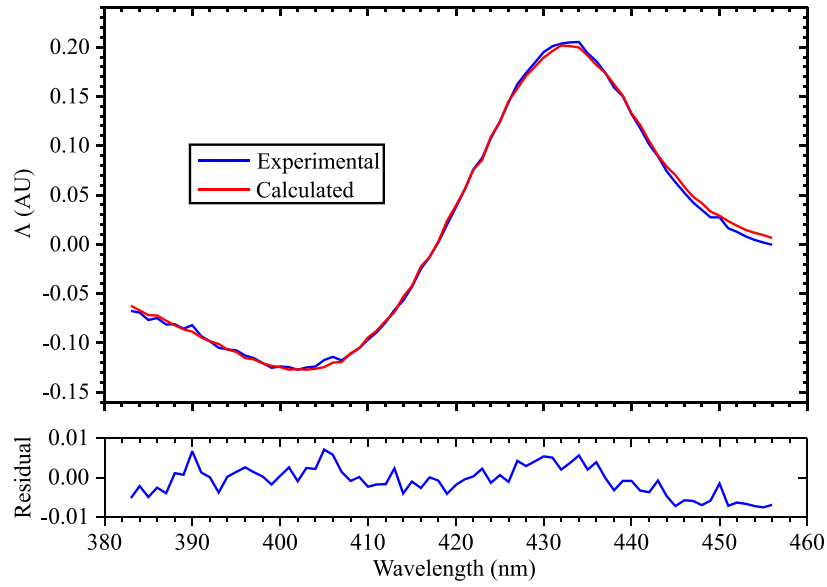


**Figure 3.2.** Spectral component  $\Lambda$  generated by fitting the SVD-processed Fig. 3.1 data to Eq. 3.1 (blue trace).  $\Lambda$  was in turn fit with the extinction coefficient difference spectrum  $\Delta\epsilon_{\text{CatNO}} = \epsilon_{\text{CatNO}} - \epsilon_{\text{Cat}}$ , where  $\epsilon_{\text{Cat}}$  and  $\epsilon_{\text{CatNO}}$  are the independently known extinction coefficient spectra for catalase and nitrosylated catalase, respectively.

$$\Delta A_{\lambda,t} = \Lambda_{\lambda} \cdot [1 - \text{frac} \cdot \exp(-k_1 t) - (1 - \text{frac}) \cdot \exp(-k_2 t)] \quad \text{Eq. 3.1}$$

$$\left. \frac{d\Delta A_{\lambda,t}}{dt} \right|_{t=0} = \Lambda_{\lambda} \cdot [\text{frac} \cdot k_1 + (1 - \text{frac}) \cdot k_2] \quad \text{Eq. 3.2}$$

Figure 3.3 shows how the quotient of the initial rate and catalase concentration varies with added ccNiR concentration in solutions initially containing 2 mM nitrite, 20 mM ferrocyanide, 4  $\mu$ M catalase and varying amounts of ccNiR. The blue circles show the experimentally obtained data, while the red line is a linear least-squares fit of the data. The initial rate of NO $\cdot$  release is seen to be directly proportional to the concentration of ccNiR. The slope of the line is an apparent second-order rate constant  $k_{app}$  with a value of  $(2.0 \pm 0.1) \times 10^4$  M $^{-1}$ s $^{-1}$ , and it provides a measure of ccNiR's ability to catalyze NO $\cdot$  formation under the given conditions. Note that the line has a non-zero intercept of  $(1.2 \pm 0.7) \times 10^{-4}$  s $^{-1}$ , which indicates that a small amount of NO $\cdot$  was generated even in the absence of ccNiR. Importantly, the values of both the slope and the non-zero intercept were found to vary with pH, so for the pH-dependence study described next it was necessary to assess the dependence of the slope  $k_{app}$  on pH in order to eliminate the contribution of the uncatalyzed catalase nitrosylation. Thus, plots such as that shown in Fig. 3.3 had to be generated at every pH that was investigated. Studies described later in this section, which assessed the initial nitrosylation rate dependence on nitrite, ferrocyanide and ammonium sulfate concentration were all carried out at a fixed pH 7.0 using the single ccNiR concentration of 100 nM. For those experiments no correction was made for the presumably minor and constant uncatalyzed contribution.

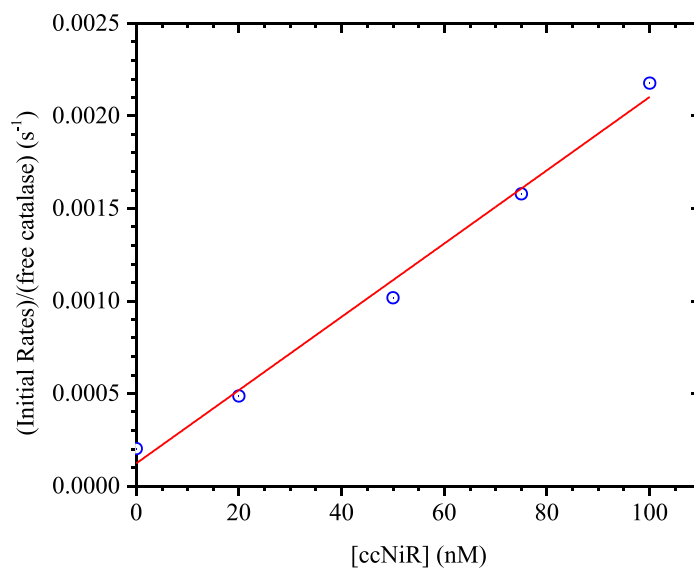


**Figure 3.3.** Initial rate of NO $\cdot$  release is directly proportional to the concentration of ccNiR. Small blue circles are the experimentally observed initial rates at the corresponding ccNiR concentration. The red line is the linear least-squares best fit to the data. This data set was collected at pH 7.0, with a nitrite concentration of 2 mM, a ferrocyanide concentration of 20 mM and a catalase concentration 4  $\mu$ M. The slope of the line gives an apparent second-order rate constant,  $k_{app} = (2.0 \pm 0.1) \times 10^4 \text{ M}^{-1} \text{ s}^{-1}$ . The intercept of  $(1.2 \pm 0.7) \times 10^{-4} \text{ s}^{-1}$  indicates that some NO $\cdot$  was generated without any ccNiR.

Figure 3.4 shows how the value of  $k_{app}$  varies with pH for a series of experiments carried out in the presence of fixed catalase, nitrite and ferrocyanide concentrations (4  $\mu$ M, 2 mM and 20 mM, respectively). The blue circles are the experimentally obtained values while the red curve is a least-squares fit of the data to the sigmoidal equation 3.3. In this equation  $k_{max}$  is the highest possible value of  $k_{app}$ , which is attained at sufficiently low pH, while  $pK_a$  may be the  $pK_a$  value of an amino acid that must remain protonated for catalysis to take place. This point will be returned to in the Discussion section 3.4. The  $pK_a$  value obtained from the least-squares fit of the Fig. 3.4 data was  $6.9 \pm 0.1$ . Note that the Fig. 3.4 data collected under more acidic conditions

have substantially larger error bars associated with them. There are two possible explanations for this observation. First, ccNiR becomes somewhat less stable at pHs below pH 6.5. Second, the contribution from the uncatalyzed rate of catalase nitrosylation becomes appreciably higher at the lower pHs. The second factor is likely to be more important because, in our experience, the uncatalyzed reaction is quite sensitive to the exact reaction conditions. Thus, repeated experiments with catalase, nitrite and ferrocyanide carried out at pH 6.5 in the absence of ccNiR showed a fair bit of scatter in the quotient of the initial rate and catalase concentration.

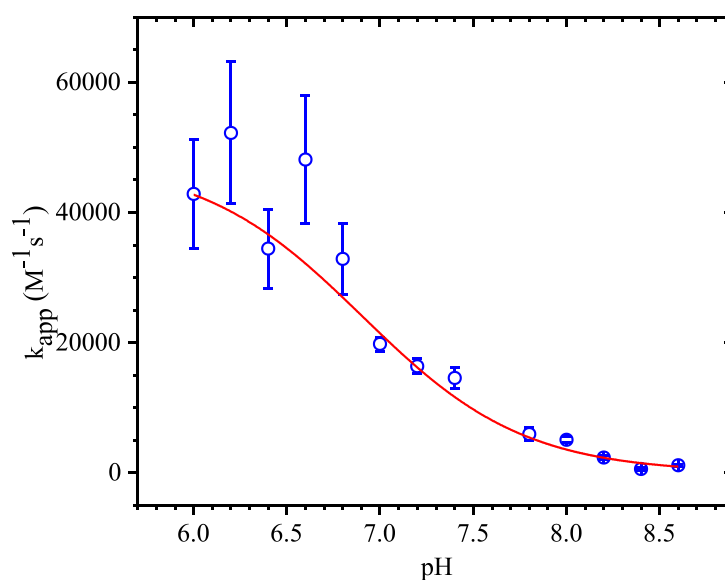


**Figure 3.4.** Dependence on pH of the parameter  $k_{app}$  obtained from (initial rate/free catalase) vs [ccNiR] plots (e.g. Fig 3.3). For all the experiments nitrite, ferrocyanide and catalase were held constant at 2 mM, 20 mM and 4  $\mu$ M, respectively. Blue circles: experimentally obtained values at each pH; red line: least-squares best fit to the sigmoidal equation 3.3. The fit yielded a  $pK_a$  value of  $6.9 \pm 0.1$ .

$$k_{app} = \frac{k_{max}}{1 + 10^{pH - pK_a}} \quad \text{Eq. 3.3}$$

Figure 3.5 shows how the quotient of the initial rate and catalase concentration varies with added nitrite concentration in solutions initially containing 100 nM ccNiR, 10 mM ferrocyanide, 4  $\mu$ M catalase and varying amounts of nitrite at pH 7.0. The blue circles show the experimentally obtained data, while the red curve is a least-squares fit of the data to a rectangular hyperbola (Eq. 3.4). Under these conditions, values of  $(4.5 \pm 0.9) \times 10^{-4}$  M and  $(2.02 \pm 0.08) \times 10^{-3}$  s<sup>-1</sup> were obtained for  $K_{mI}$  and  $M_I$ , respectively.

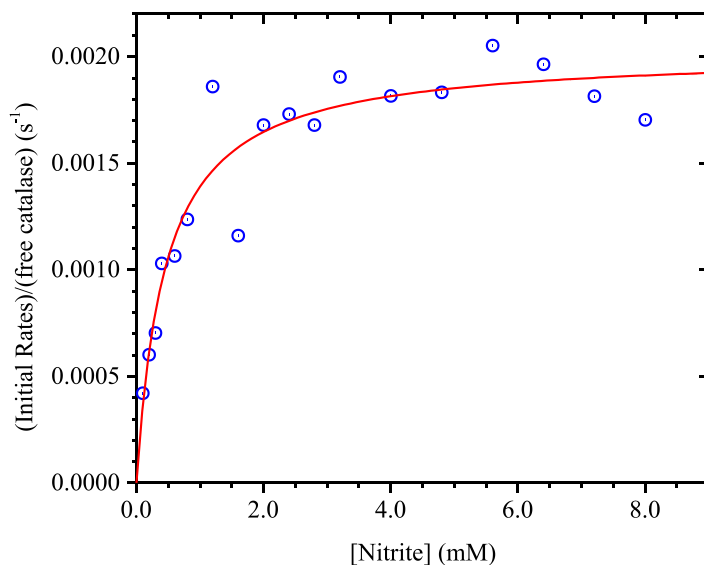


**Figure 3.5.** Dependence of initial rate of NO $\cdot$  release on nitrite concentration. Blue circles are the experimentally obtained values at each nitrite concentration, while the red curve is the least-squares fit of the data to the rectangular hyperbola, Eq. 3.4. This set of experiments was performed at pH 7.0 in the presence of 100 nM ccNiR, 4  $\mu$ M catalase, 10 mM ferrocyanide and varying nitrite concentration. The least-squares fit yielded the parameter values  $K_{mI} = (4.5 \pm 0.9) \times 10^{-4}$  M and  $M_I = (2.0 \pm 0.1) \times 10^{-3}$  s<sup>-1</sup>.

$$\frac{V_0}{[\text{Cat}]} = \frac{M_1[\text{NO}_2^-]}{K_{m1} + [\text{NO}_2^-]} \quad \text{Eq. 3.4}$$

Figure 3.6 shows how the quotient of the initial rate and catalase concentration varies with added ferrocyanide concentration in solutions initially containing 100 nM ccNiR, 8 mM nitrite, 4  $\mu\text{M}$  catalase and varying amounts of ferrocyanide at pH 7.0. The blue circles show the experimentally obtained data, while the red curve is a least-squares fit of the data to the rectangular hyperbola of Eq. 3.5. Under these conditions, values of  $(7 \pm 2) \times 10^{-4} \text{ M}$  and  $(1.9 \pm 0.1) \times 10^{-3} \text{ s}^{-1}$  were obtained for  $K_{m2}$  and  $M_2$ , respectively.

$$\frac{V_0}{[\text{Cat}]} = \frac{M_2[\text{Fe}(\text{CN})_6^{4-}]}{K_{m2} + [\text{Fe}(\text{CN})_6^{4-}]} \quad \text{Eq. 3.5}$$

Figure 3.7 shows how ammonium sulfate affects the rate of  $\text{NO}\cdot$  formation. Four sets of experiments were carried out in the presence of 0, 10, 20 and 100 mM of ammonium sulfate, respectively. In each set of the initial concentrations of ccNiR, ferrocyanide and catalase were the same, 100 nM ccNiR, 20 mM ferrocyanide and 4  $\mu\text{M}$  catalase, respectively, but the concentrations of nitrite were varied. One can see from Fig. 3.7 that ammonium sulfate is a mixed inhibitor of ccNiR's catalytic  $\text{NO}\cdot$  generation activity, affecting both  $K_m$  and the maximal rate in rectangular hyperbolic plots of initial rate vs. nitrite concentration.

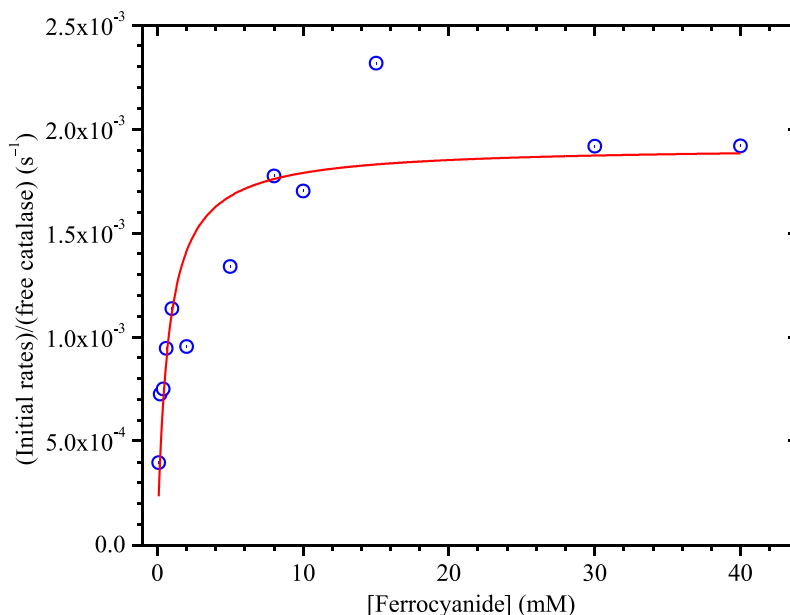


**Figure 3.6.** Dependence of initial rate of  $\text{NO}\cdot$  release on ferrocyanide concentration. Blue circles are the experimentally obtained values at each ferrocyanide concentration, while the red curve is the least-squares fit of the data to the rectangular hyperbola, Eq. 3.5. This set of experiments was performed at pH 7.0 in the presence of 100 nM ccNiR, 4  $\mu\text{M}$  catalase, 8 mM nitrite and varying ferrocyanide concentration. The least-squares fit yielded the parameter values  $K_{m2} = (7 \pm 2) \times 10^{-4}$  M and  $M_2 = (1.9 \pm 0.1) \times 10^{-3}$  s $^{-1}$ .

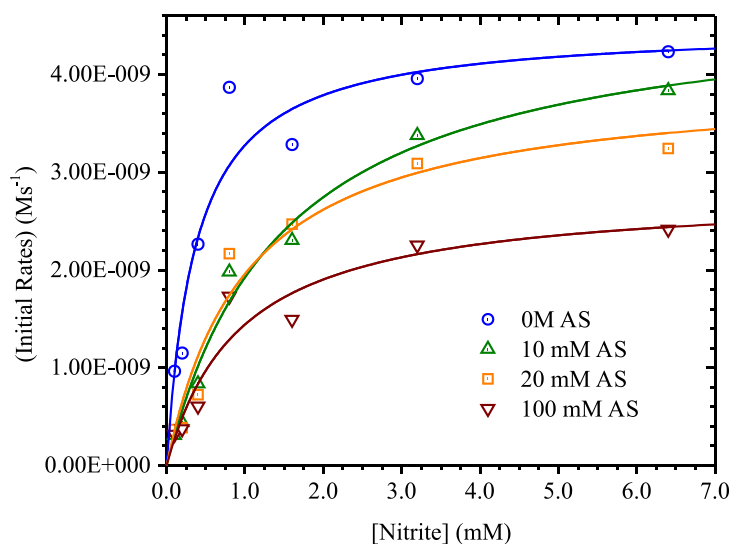


**Figure 3.7.** Effect of varying ammonium sulfate concentrations on ccNiR-catalyzed reduction of nitrite to nitric oxide by ferrocyanide. The concentrations of ccNiR, catalase and ferrocyanide were 100 nM, 4  $\mu\text{M}$  and 20 mM, respectively in all experiments. Symbols: experimentally derived initial rate values; lines: least-squares fits to rectangular hyperbolas of initial rate vs  $[\text{NO}_2^-]$  plots for the varying ammonium sulfate concentrations.

**3.3.2. Detection of ferrocyanide oxidation at higher ccNiR concentrations.** The experiments presented in Section 3.3.1 were carried out at ccNiR concentrations of 100 nM or less, and under those conditions at most 1 – 2  $\mu\text{M}$   $\text{NO}\cdot$  were generated during an hour-long experiment. This section describes a series of experiments carried out in the presence of micromolar concentrations of ccNiR. At these higher concentrations the UV/Vis spectrum of ccNiR could be monitored directly, as could the appearance of ferricyanide that accompanied  $\text{NO}\cdot$  formation.

The blue traces in Fig. 3.8 show the spectral changes observed in a pH 7.0 solution initially containing 1  $\mu\text{M}$  ccNiR, 8 mM nitrite and 20 mM ferrocyanide. For clarity only selected traces are shown, but spectra were collected at 15s intervals over the course of one hour. SVD analysis<sup>8,9</sup> showed that only two components are needed to faithfully reconstruct a noise-reduced absorbance matrix. The SVD-treated data were then fit to Eq. 3.6 using a global fitting routine (red traces, Fig. 3.8).<sup>4-6</sup> In Eq. 3.6  $\Delta A_{\lambda,t}$  is the absorbance change observed at wavelength  $\lambda$  after time  $t$ , the spectral component  $\Lambda_1$  grows in exponentially with  $k_{obs} = 0.0056 \text{ s}^{-1}$ , while  $\Lambda_2$  grows in linearly.

$$\Delta A_{\lambda,t} = \Lambda_{1(\lambda)} [1 - \exp(-k_{obs} \cdot t)] + \Lambda_{2(\lambda)} \cdot t \quad \text{Eq. 3.6}$$

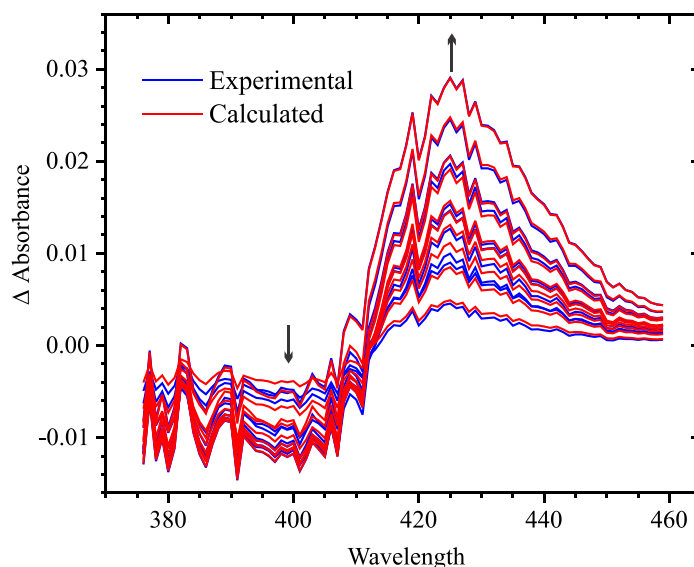


**Figure 3.8.** Blue traces: SVD-treated spectral changes observed at selected time intervals over the course of one hour in a pH 7.0 solution initially containing 1  $\mu\text{M}$  ccNiR, 8 mM nitrite and 20 mM ferrocyanide. Red traces: least-squares best fit to Eq. 3.6. The first six spectra are at 60 s intervals starting at 60 s, the next two are at 360 s intervals, and the final two at 1000 s intervals.

Figure 3.9 shows the spectral components obtained from the fitting process.  $\Lambda_1$  was in turn fit with the independently obtained extinction coefficient difference spectrum associated with 2-electron reduction of nitrite-loaded ccNiR ( $\text{Fe}_{\text{H1}}^{\text{III}}(\text{NO}_2^-)$ ) to  $\{\text{Fe}_{\text{H1}}\text{NO}\}^7$ .<sup>7</sup> The fit showed that 0.42  $\mu\text{M}$  out of the total 1  $\mu\text{M}$  ccNiR present in solution was reduced in the exponential process governed by  $k_{\text{obs}}$ . However, analysis of the spectrum obtained immediately after mixing all the reagents (within 30 s) showed that the remaining 0.58  $\mu\text{M}$  had already reduced within the dead time of the experiment (data not shown). Thus, under the reaction conditions all the available ccNiR was reduced to the  $\{\text{Fe}_{\text{H1}}\text{NO}\}^7$  form within about 10 minutes. The component  $\Lambda_2$  that grew in linearly was fit with both the independently known extinction coefficient spectrum of ferricyanide and the extinction coefficient difference spectrum associated with 2-electron reduction of nitrite-loaded ccNiR ( $\text{Fe}_{\text{H1}}^{\text{III}}(\text{NO}_2^-)$ ) to  $\{\text{Fe}_{\text{H1}}\text{NO}\}^7$  (ferrocyanide didn't

contribute significantly to the changes observed in this spectral region). The major contribution to  $\Lambda_2$  came from ferricyanide, and showed that ferricyanide was generated at a rate of  $3.2 \times 10^{-9}$  M/s, or 11.5  $\mu$ M/h. The contribution from ccNiR reduction was only  $1.1 \times 10^{-11}$  M/s ( $4 \times 10^{-8}$  M/h) which would seem to be too low to measure; however, the fit was noticeably worse if the ccNiR contribution was left out.

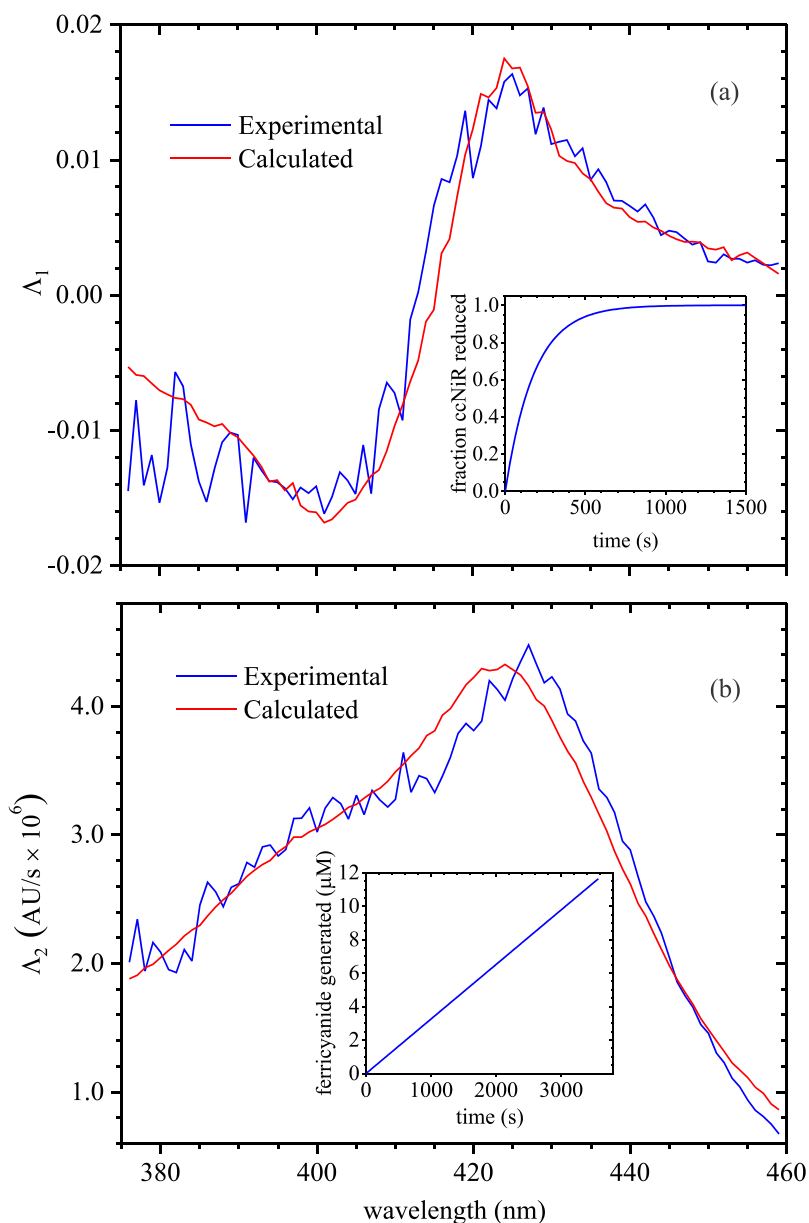


**Figure 3.9.** Spectral components (a)  $\Delta_1$  and (b)  $\Delta_2$  generated by fitting the SVD-processed Fig. 3.8 data to Eq. 3.6 (blue traces). The two components were in turn fit with the independently obtained extinction coefficient spectra for  $\Delta\epsilon_{\text{ccNiR}} = \epsilon(\{\text{Fe}_{\text{HI}}\text{NO}\}^7) - \epsilon[\text{Fe}_{\text{HI}}^{\text{III}}(\text{NO}_2^-)]$  and for ferricyanide (spectral changes due to ferrocyanide were negligible in the region analyzed). The insets show that the first component grows exponentially over approximately 10 minutes, whereas the second increases linearly with time; roughly 12  $\mu\text{M}$  ferricyanide and an equivalent amount of  $\text{NO}\cdot$  are generated over the course of one hour, and the ccNiR is completely reduced to the  $\{\text{Fe}_{\text{HI}}\text{NO}\}^7$  form.

Figure 3.10 shows how the initial rate of ferricyanide generation, adjusted for slight variations in ccNiR concentration, varied with ferrocyanide concentration. The blue circles show the experimentally obtained data, while the red curve is a least-squares fit of the data with a rectangular hyperbola (Eq. 3.7), which in this case represents a classic Michaelis-Menten plot that provides both a  $K_m$  value and  $k_{cat}$ . For these experiments the ccNiR concentration was nominally about 0.8  $\mu\text{M}$  and nitrite 8 mM. Under these conditions, values of  $(7 \pm 2) \times 10^{-4}$  M and  $(1.9 \pm 0.1) \times 10^{-3} \text{ s}^{-1}$  were obtained for  $K_{m3}$  and  $k_{cat1}$ , respectively.

$$\frac{V_0}{[\text{ccNiR}]} = \frac{k_{cat1}[\text{Fe}(\text{CN}_6)^{4-}]}{K_{m3} + [\text{Fe}(\text{CN}_6)^{4-}]} \quad \text{Eq. 3.7}$$

The  $K_{m3}$  value matches  $K_{m2}$  obtained from the experiments of Fig. 3.6 which tracked the dependence of  $\text{NO}\cdot$  formation on ferrocyanide concentration, confirming the direct relationship between  $\text{NO}\cdot$  formation and ferrocyanide oxidation. Importantly the value of  $k_{cat1}$  obtained from the Fig. 3.10 experiments correlates directly with ferricyanide or  $\text{NO}\cdot$  formation; the corresponding value obtained from the Fig. 3.6 experiments correlates with CatNO formation, which is an indirect measure of  $\text{NO}\cdot$  formation that depends also on catalase concentration.

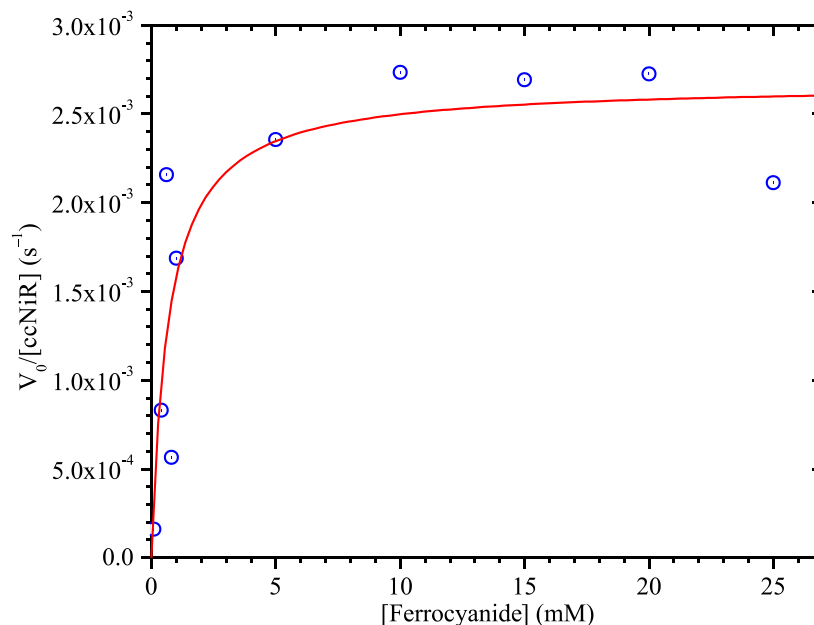


**Figure 3.10.** Dependence of initial rate of ferrocyanide oxidation, adjusted for ccNiR concentration, on ferrocyanide concentration. Blue circles are the experimentally obtained values at each ferrocyanide concentration, while the red curve is the least-squares fit of the data to the rectangular hyperbola Eq. 3.7. This set of experiments was performed at pH 7.0 in the presence of approximately 0.8  $\mu\text{M}$  ccNiR, 8 mM nitrite and varying ferrocyanide concentration. The least-squares fit yielded the parameter values  $K_{m3} = (7 \pm 3) \times 10^{-4}$  M and  $k_{cat} = (2.7 \pm 0.3) \times 10^{-3}$   $\text{s}^{-1}$ .

### 3.4. Discussion

The experiments that used catalase as a trapping agent demonstrated that ccNiR can catalyze the reduction of nitrite to nitric oxide by the weak reductant ferrocyanide (Scheme 3.1). The rate of  $\text{NO}\cdot$  formation shows first-order dependence on ccNiR concentration and hyperbolic dependence on nitrite and ferrocyanide concentrations. Significantly, it also shows sigmoidal dependence on pH (Eq. 3.3, Fig. 3.4), which suggests the presence of an active site amino acid residue with a  $\text{pK}_a$  of 6.9 that must be protonated for reduction to take place at the nitrite-loaded heme 1. The most likely candidate amino acid in the *S. oneidensis* enzyme is His 257 (Fig. 1.3), whose importance has already been predicted in computational studies.<sup>10</sup> As shown in Scheme 2.3 the first step in nitrite reduction requires concomitant diprotonation of one nitrite oxygen, which then leaves as water. Based on computational analysis Bykov and Neese proposed that

the equivalent of His 257 (Fig. 1.3) in *E. coli* ccNiR is essential for carrying out this diprotonation efficiently.<sup>10</sup> His 257 could well have a pK<sub>a</sub> of 6.9, and so be the essential amino acid whose deprotonation leads to loss of activity at high pH in Fig. 3.4.

The NO· trapping experiments of Section 3.2.1 measure the rate of catalase nitrosylation. This will be lower than the actual rate of ccNiR-catalyzed NO· formation because the catalase nitrosylation rate displays first-order dependence on catalase concentration under the conditions employed in these experiments. Fortunately, the absolute rate of ferrocyanide oxidation, and thus of NO· formation (Scheme 3.1), can be monitored directly by UV/Vis spectroscopy at sufficiently high ccNiR concentrations (Section 3.2.2). Comparison of the  $K_m$  values obtained for initial rate dependence on ferrocyanide concentration in the NO· trapping and ferricyanide monitoring experiments showed these to be equivalent (Figs. 3.6 and 3.10), providing confidence that ferricyanide and NO· formation were directly correlated. From the Fig. 3.10 analysis a true  $k_{cat}$  value of  $(2.7 \pm 0.3) \times 10^{-3} \text{ s}^{-1}$  was obtained for the ferrocyanide dependence in the presence of 8 mM nitrite. Given the  $K_{mI}$  value of  $(4.5 \pm 0.9) \times 10^{-4} \text{ M}$  obtained for the nitrite dependence of NO· generation (Eq. 3.4, Fig. 3.5) the measured  $k_{cat}$  value is about 95% of the absolute  $k_{cat}$  value that would be obtained at limiting ferrocyanide *and* nitrite concentrations,  $(2.9 \pm 0.3) \times 10^{-3} \text{ s}^{-1}$ . This value is miniscule compared to the  $k_{cat}$  associated with *S. oneidensis* ccNiR-catalyzed reduction of nitrite to ammonia by methyl viologen monocation radical (800 electrons transferred per second).<sup>3</sup> As discussed in Chapter 2 ccNiR appears to be designed to minimize NO· by greatly stabilizing the substitutionally inert  $\{\text{Fe}_{\text{HI}}\text{NO}\}^7$  moiety relative to the substitutionally more labile  $\{\text{Fe}_{\text{HI}}\text{NO}\}^6$ , with the result that  $\{\text{Fe}_{\text{HI}}\text{NO}\}^6$  never accumulates appreciably.

### 3.5. References

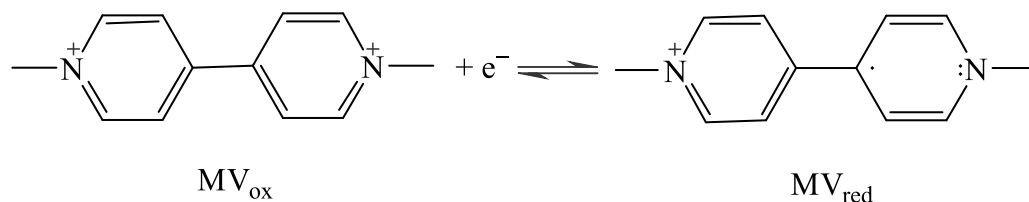
- [1] Enemark, J. H., and Feltham, R. D. (1974) Principles of Structure, Bonding and Reactivity for Metal Nitrosyl Complexes, *Coord. Chem. Rev.* 13, 339-406.
- [2] Purwar, N., McGarry, J. M., Kostera, J., Pacheco, A. A., and Schmidt, M. (2011) Interaction of nitric oxide with catalase: structural and kinetic analysis, *Biochemistry* 50, 4491-4503.
- [3] Youngblut, M., Judd, E. T., Srajer, V., Sayyed, B., Goelzer, T., Elliott, S. J., Schmidt, M., and Pacheco, A. A. (2012) Laue crystal structure of *Shewanella oneidensis* cytochrome *c* nitrite reductase from a high-yield expression system, *J. Biol. Inorg. Chem.* 17, 647-662.
- [4] Koebke, K. J., Pauly, D. J., Lerner, L., Liu, X., and Pacheco, A. A. (2013) Does the oxidation of nitric oxide by oxymyoglobin share an intermediate with the metmyoglobin-catalyzed isomerization of peroxynitrite?, *Inorg. Chem.* 52, 7623-7632.
- [5] Koebke, K. J., Waletzko, M. T., and Pacheco, A. A. (2016) Direct monitoring of the reaction between photochemically generated nitric oxide and *Mycobacterium tuberculosis* truncated hemoglobin N wild type and variant forms: an assessment of computational mechanistic predictions, *Biochemistry* 55, 686-696.
- [6] McGarry, J. M., and Pacheco, A. A. (2018) Upon further analysis, neither cytochrome *c*<sub>554</sub> from *Nitrosomonas europaea* nor its F156A variant display NO reductase activity, though both proteins bind nitric oxide reversibly, *J. Biol. Inorg. Chem.* 23, 861-878.
- [7] Ali, M., Stein, N., Mao, Y., Shahid, S., Schmidt, M., Bennett, B., and Pacheco, A. A. (2019) Trapping of a putative intermediate in the cytochrome *c* nitrite reductase (ccNiR)-catalyzed reduction of nitrite: implications for the ccNiR reaction mechanism *J. Am. Chem. Soc.* 141, 13358-13371.
- [8] Press, W. H., Teukolsky, S. A., Vetterling, W. T., and Flannery, B. P. (2007) Numerical Recipes the art of scientific computing, 3rd ed., pp 65-75, Cambridge University Press, New York, NY.
- [9] Henry, E. R., and Hofrichter, J. (1992) Singular Value Decomposition: Application to Analysis of Experimental Data, In *Meth. Enzymol.* (Brand, L., and Johnson, M. L., Eds.), pp 129-192, Academic Press, San Diego.
- [10] Bykov, D., and Neese, F. (2011) Substrate binding and activation in the active site of cytochrome *c* nitrite reductase: a density functional study, *J. Biol. Inorg. Chem.* 16, 417-430.

## Chapter 4

### Determination of the equilibrium constant for methyl viologen monocation radical dimerization

#### 4.1. Overview

As mentioned in Chapter 1 the standard assay for ccNiR activity uses the methyl viologen monocation radical ( $MV_{red}$ ), a powerful reductant, as the electron donor (Scheme 4.1). It has long been known that  $MV_{red}$  exists in equilibrium with its dimer,<sup>1-3</sup> but this fact is generally ignored when using the radical in enzymological assays.



**Scheme 4.1.** Methyl viologen accepts an electron to produce  $MV_{red}$ , a powerful reductant.

For routine assays that use total reduced methyl viologen concentrations of 100  $\mu M$  or less it is reasonable to neglect the monomer-dimer equilibrium because the dimer concentration at any given moment will be low.<sup>1</sup> However, the Pacheco group anticipates doing future experiments with ccNiR that will require high concentrations of reduced methyl viologen, perhaps even concentrations greater than 1 mM. To prepare for such experiments this chapter

describes an analysis of the equilibrium process for methyl viologen monocation radical dimerization, which also yielded extinction coefficient spectra for  $MV_{\text{red}}$  and its dimer. As will be demonstrated these spectra can be used to track the monomer-dimer equilibrium in a solution in which the amount of reduced methyl viologen is changing with time, thereby greatly increasing the potential scope of  $MV_{\text{red}}$ -based assays.

## 4.2. Experimental methods

**4.2.1. General materials and instrumentation.** Reagents were obtained from Fisher Scientific, Acros Organics or Sigma-Aldrich, unless specified otherwise, and used without additional purification. Controlled potential electrolyses of methyl viologen solutions containing varying total concentrations of the species were performed in an optically transparent thin-layer electrode cell similar to one used in earlier work by this group,<sup>4</sup> and elsewhere.<sup>5, 6</sup> An Ag/AgCl electrode was used as a reference (BASi model RE-5B), and was periodically standardized in cyclic voltammetry experiments by comparison with the methyl viologen couple ( $\epsilon_m^o = -0.449$  V vs. the standard hydrogen electrode, SHE).<sup>1</sup> A BASi Epsilon EC potentiostat was used to set the potential, and a UV/Vis spectrophotometer housed in an anaerobic glovebox-housed was used to obtain the spectra of the reduced methyl viologen solutions.

**4.2.2. Data collection and processing.** In each of the experiments a solution containing a nominal concentration of oxidized methyl viologen ( $MV_{\text{ox}}$ , Scheme 4.1), in 0.4 M NaCl and buffered at pH 7.0 with 50 mM HEPES buffer containing 1 mM EDTA, was put into the spectropotentiometric cuvette (pathlength 0.021 cm), and its UV/Vis spectrum was recorded. The solution was then subjected to an applied potential of  $-603$  mV vs SHE for 8 minutes, after which a second UV/Vis spectrum was collected. The chosen applied potential was low enough

to completely reduce the dication by one electron, but high enough to avoid two-electron reduction.<sup>1</sup> A total of seven solutions were analyzed, ranging in nominal MV<sub>ox</sub> concentration from 150 μM to 2.5 mM. The exact methyl viologen concentration of each solution was determined from the UV/Vis spectrum of the MV<sub>ox</sub> prior to applying a potential, using the independently obtained extinction coefficient spectrum of the dication. The monomer-dimer equilibrium in the fully reduced samples was analyzed as described in the following section using a global fitting routine written within the commercially available software package Mathcad 15 (PTC Software).

**4.2.3. Equilibrium expression derivation.** Let  $C_{mono}$  be the MV<sub>red</sub> equilibrium concentration,  $C_{dim}$  the corresponding MV<sub>red</sub> dimer equilibrium concentration, and  $C_T$  the total concentration of 1-electron reduced methyl viologen. With these abbreviations Scheme 4.2 shows the  $C_{mono}$  -  $C_{dim}$  equilibrium, Eq. 4.1 shows the relationship between  $C_{mono}$ ,  $C_{dim}$  and  $C_T$ , and Eq. 4.2 gives the equilibrium expression.



**Scheme 4.2.** Monomer-dimer equilibrium of methyl viologen

$$C_T = C_{mono} + 2C_{dim} \tag{Eq. 4.1}$$

$$K_{eq} = \frac{C_{dim}}{C_{mono}^2} = \frac{C_{dim}}{(C_T - 2C_{dim})^2} \tag{Eq. 4.2}$$

Equation 4.2 is a quadratic that can be readily solved for  $C_{dim}$ . This was done using the Mathcad 15 symbolic evaluation package and gave two roots, of which the one shown in Eq. 4.3 was found to represent physical reality.

$$C_{dim} = \frac{4C_T K_{eq} - \sqrt{8C_T K_{eq} + 1} + 1}{8K_{eq}} \quad \text{Eq. 4.3}$$

### 4.3. Results

**4.3.1. Spectral changes as a function of  $C_T$ .** The blue trace in Fig. 4.1 shows the UV/Vis spectrum of a solution nominally containing 1.5 mM of  $MV_{ox}$ , while the overlaid red trace is the least-squares best fit using the independently obtained  $MV_{ox}$  extinction coefficient spectrum and a baseline correction. From this fit the true methyl viologen concentration in the solution ( $C_T$ ) was determined to be 1.21 mM. Other samples were similarly found to contain less methyl viologen than expected. The commercially obtained methyl viologen solid from which the solutions were made was nominally 98% pure; however, the UV/Vis spectral analysis shows that the solid was only about 80%  $MV_{ox}$ . Most likely the commercially obtained solid was simply more hydrated than its label suggested; the good fit seen in Fig. 4.1 indicates that the solution contained no spectrally detectable impurities.

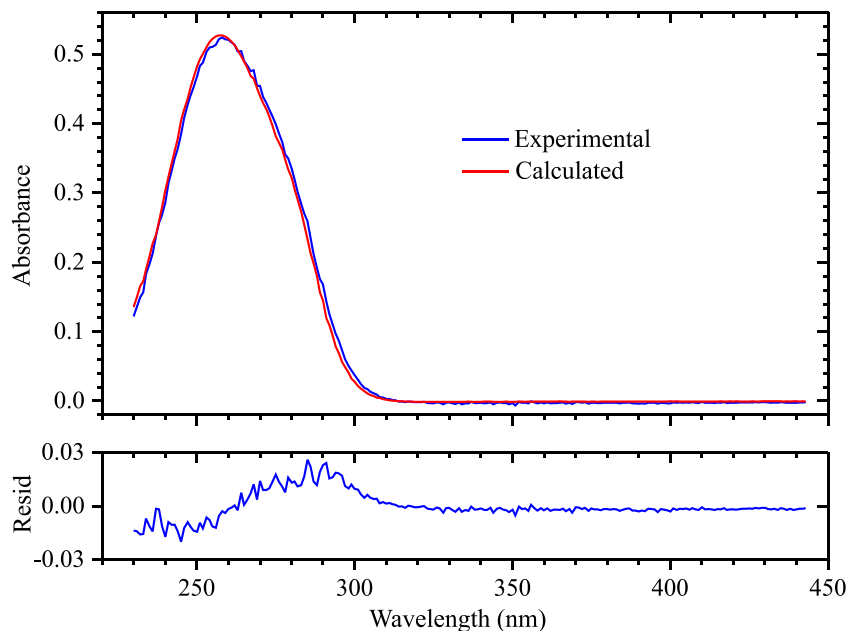


**Figure 4.1.** Example of an  $MV_{ox}$  spectrum fit, using the independently obtained extinction coefficient spectrum to calculate the  $MV_{ox}$  concentration. For this sample the  $MV_{ox}$  concentration was determined to be 1.21 mM. Oxidized methyl viologen has no absorbance above 350 nm.

Figure 4.2a shows the UV/Vis spectrum of the methyl viologen sample from Fig. 4.1 after it was reduced by applying a potential of  $-603$  mV vs SHE. An apparent extinction coefficient spectrum (Fig. 4.2b) for this sample was obtained by dividing spectrum 4.2a by the total methyl viologen concentration obtained from analysis of the oxidized spectrum (Fig. 4.1). The Fig. 4.2b spectrum is not a true extinction coefficient spectrum because it varies with total methyl viologen concentration  $C_T$ , as shown in Fig. 4.3. Notice that as  $C_T$  is increased from  $\sim 100$   $\mu\text{M}$  to  $\sim 2$  mM absorbance maxima at 396 nm and 605 nm decrease in intensity, whereas maxima at 366 nm and 552 nm grow in. In addition, the absorbance in the far-red region of the spectrum increases steadily. This is because, as  $C_T$  is increased, The Scheme 4.2 monomer-dimer equilibrium shifts to the right, so signals arising from the dimer gain prominence.

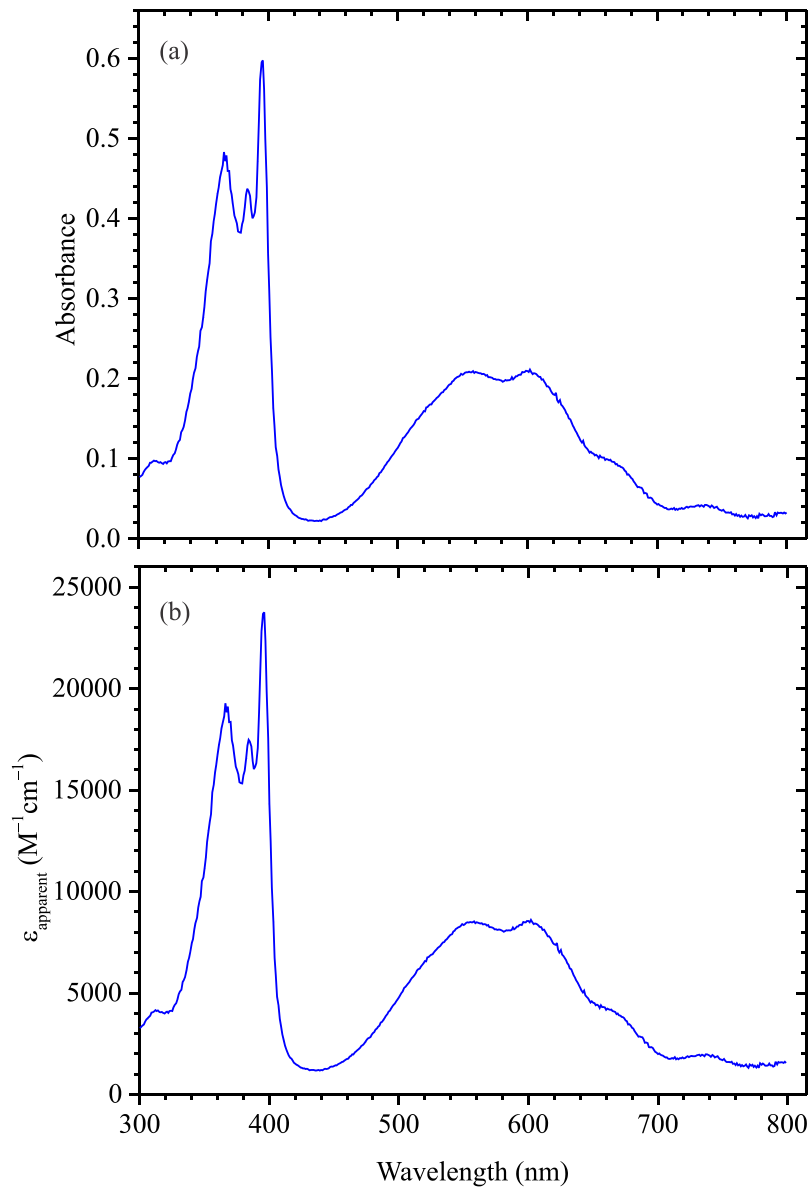


**Figure 4.2.** (a) UV/Vis spectrum of the methyl viologen sample from Fig. 4.1 after complete reduction at an applied potential of  $-603$  mV vs SHE. (b) Apparent extinction coefficient spectrum calculated by dividing spectrum 4.2a by the total methyl viologen concentration obtained from analysis of the oxidized spectrum (Fig. 4.1).

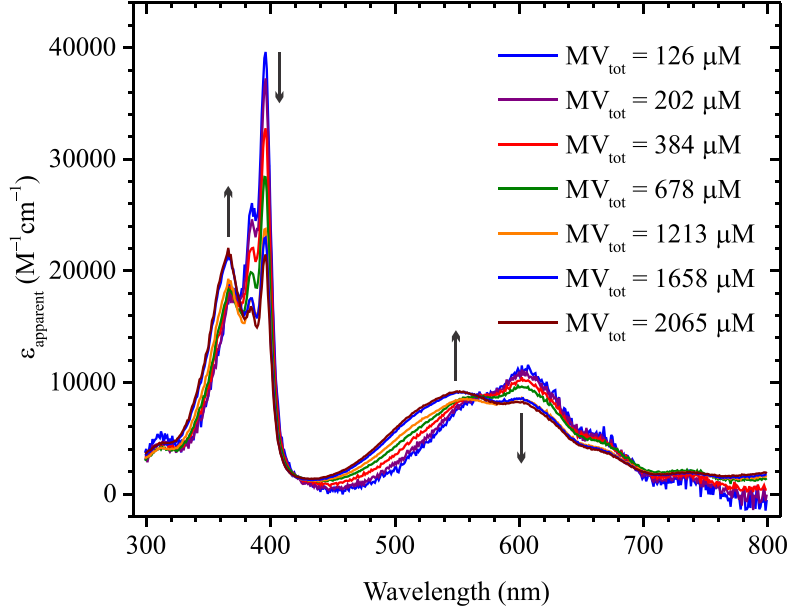


**Figure 4.3.** Apparent extinction coefficient spectra obtained at varying concentrations of total reduced methyl viologen,  $C_T$ . The arrows show how key features change as  $C_T$  increases. The data set was first subjected to singular value decomposition (SVD) to reduce noise.<sup>9, 10</sup> The SVD process also verified that only two spectral components contribute the collection of spectra, presumably those of the monomer and dimer.

### 4.3.2. Extraction of $K_{eq}$ and of the extinction coefficient spectra for reduced methyl viologen

**monomer and dimer from the matrix of reduced spectra.** Equation 4.4 is the Beer's law

expression at a given wavelength  $\lambda$  and total reduced MV concentration  $C_T$  for a mixture of

monomer and dimer. Equation 4.5 was obtained by dividing both sides of Eq. 4.4 by  $C_T l$ ; this

equation defines an apparent extinction coefficient  $\epsilon_{\lambda, C_T}$  as a function of  $\lambda$  and  $C_T$ . Equation 4.6

is a streamlined version of Eq. 4.5, which was conveniently used to fit the SVD-processed data

from Fig. 4.3 using a Mathcad program that works as described in the following paragraph.

$$A_{\lambda, C_T} = (\epsilon_{mono})_{\lambda} l (C_{mono})_{C_T} + (\epsilon_{dim})_{\lambda} l (C_{dim})_{C_T} \quad \text{Eq. 4.4}$$

$$\epsilon_{\lambda, C_T} = \frac{(\epsilon_{mono})_{\lambda} (C_{mono})_{C_T}}{C_T} + \frac{(\epsilon_{dim})_{\lambda} (C_{dim})_{C_T}}{C_T} \quad \text{Eq. 4.5}$$

$$\varepsilon_{\lambda, C_T} = (\varepsilon_{mono})_{\lambda} \cdot \text{Frac}_{MVred} + (\varepsilon_{dim})_{\lambda} \cdot \text{Frac}_{MV2} \quad \text{Eq. 4.6}$$

where

$$\text{Frac}_{MVred} = \frac{(C_{mono})_{C_T}}{C_T}$$

$$\text{Frac}_{MV2} = \frac{(C_{dim})_{C_T}}{C_T}$$

The user of the Mathcad program provides a trial value of  $K_{eq}$  and then the program uses the trial  $K_{eq}$  to generate values of  $C_{mono}$  and  $C_{dim}$  for each value of the independent variable  $C_T$  using Eqs. 4.1 and 4.3. The  $C_{mono}$  and  $C_{dim}$  values, scaled with  $C_T$  as shown in Eq. 4.6, are used to populate a matrix **Frac**. The corresponding extinction coefficient spectrum matrix is then calculated using Eq. 4.7.<sup>7, 8</sup> In this equation  $\varepsilon_{tot}$  is the SVD-processed matrix of experimentally obtained apparent extinction coefficients from the Fig. 4.3 spectra, and  $\varepsilon_{frac}$  is the trial matrix of extinction coefficient spectra for the monomeric and dimeric reduced MV species, respectively ( $\varepsilon_{mono}$  is in column 1 and  $\varepsilon_{dim}$  in column 2).

The matrix product to the right of  $\epsilon_{\text{tot}}$  is the right pseudo-inverse of the matrix **Frac**,\* which is composed of  $\text{Frac}_{\text{mono}}$  and  $\text{Frac}_{\text{Dim}}$  values as defined in Eq. 4.6. Now a matrix  $\epsilon_{\text{calc}}$  is calculated using Eq. 4.8, and this matrix is compared to  $\epsilon_{\text{tot}}$  in a least-squares sense. The value of  $K_{\text{eq}}$  is manually adjusted within the Mathcad program until the difference between  $\epsilon_{\text{tot}}$  and  $\epsilon_{\text{calc}}$  is minimized.

$$\epsilon_{\text{frac}} = \epsilon_{\text{tot}} \cdot \mathbf{Frac} \cdot (\mathbf{Frac}^T \cdot \mathbf{Frac})^{-1} \quad \text{Eq. 4.7}$$

$$\epsilon_{\text{calc}} = \epsilon_{\text{frac}} \cdot \mathbf{Frac}^T \quad \text{Eq. 4.8}$$

For the Fig. 4.3 data the best value of  $K_{\text{eq}}$  was found to be  $784 \pm 17$ . The corresponding extinction coefficient spectra of the methyl viologen monomer and dimer are shown in Fig. 4.4. The best fits to the spectra are given in Fig. 4.5a, while a fitted  $\epsilon_{\text{tot}}$  vs  $C_T$  slice at 600 nm is shown in Fig 4.5b.

---

\* The right pseudoinverse of a matrix **M** is conventionally defined as  $\mathbf{M}^T \cdot (\mathbf{M} \cdot \mathbf{M}^T)^{-1}$ . [7] Malinowski, E. R. (1991) *Factor analysis in chemistry, 2<sup>nd</sup> ed.*, John Wiley & Sons, Inc. However, this assumes that **M** is composed of row vectors, while in our programs **Frac** is defined as a 2-column vector, where  $C_{\text{mono}}$  is in column 1 and  $C_{\text{dim}}$  in column 2. Our pseudoinverse therefore transposes each component of the conventional one.

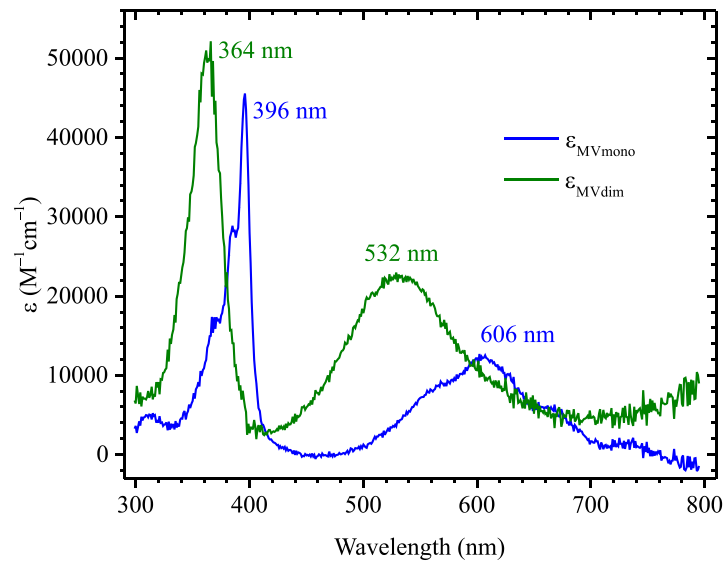


**Figure 4.4.** Extinction coefficient spectra for the reduced methyl viologen monomer and dimer species, as calculated by least-squares fit of the Fig. 4.3 data set with Eq. 4.6.

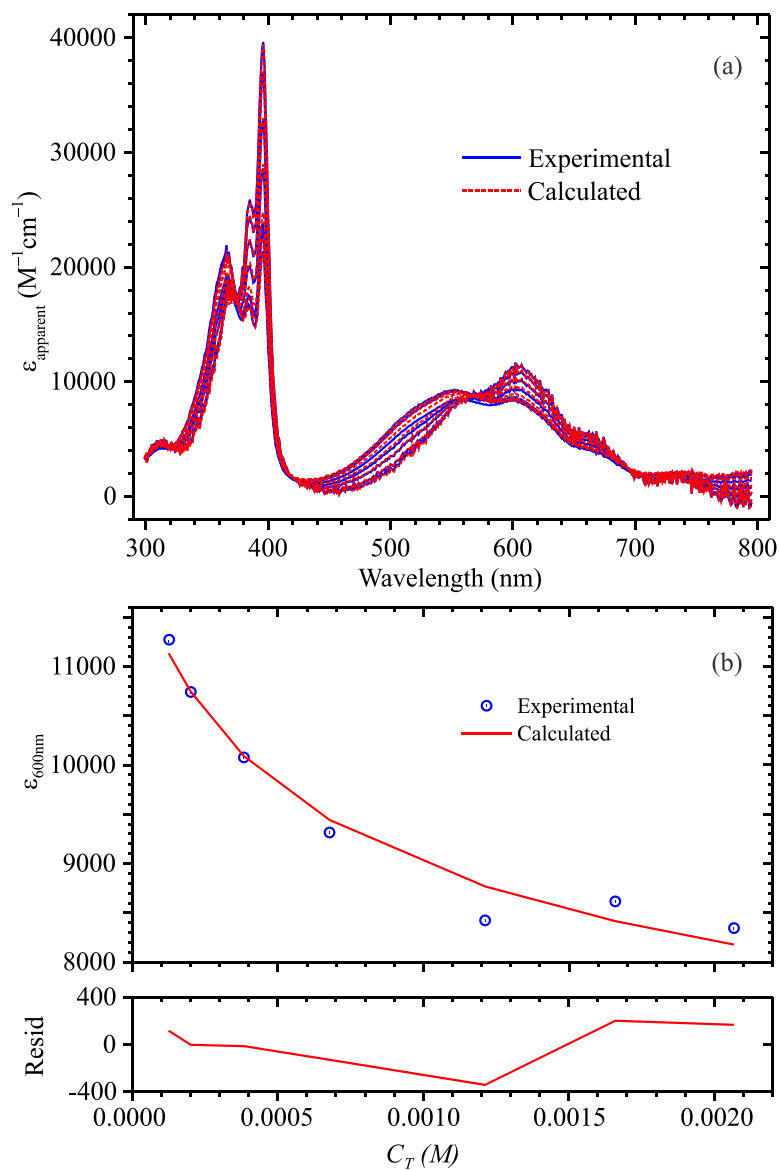


**Figure 4.5.** (a) Least-squares fit of the SVD-processed apparent extinction coefficient spectra of reduced methyl viologen at varying  $C_T$ . (b) Change in apparent extinction coefficient with  $C_T$  at 600 nm.

#### 4.4. Discussion

The results presented in this chapter open the door to using the standard ccNiR assay over a much broader range than it has been used in the past, and may also expand its usefulness in other ways. Currently in the standard assay one takes care to ensure that  $C_T$  falls in a narrow range of 80 – 100  $\mu\text{M}$ , then measures spectral changes with time at 600 nm. Under these conditions the apparent extinction coefficient we obtain at 600 nm is very close to the value reported by Watanabe and Honda,  $13,700 \text{ M}^{-1}\text{cm}^{-1}$  (Figs. 4.3 and 4.5).<sup>1</sup> The extinction coefficient spectra obtained for the reduced methyl viologen monomer and dimer (Fig 4.4) allow one to fit spectral changes over a range of wavelengths to determine the individual concentrations of  $C_{mono}$  and  $C_{dim}$ , as well as the total reduced methyl viologen concentration  $C_T$  (Eq. 4.1). As an example, Fig. 4.6 presents results from a ccNiR assay obtained under fairly typical conditions, but monitoring the spectral range from 540 nm to 700 nm instead of a single wavelength. The spectral changes with time were analyzed using the extinction coefficient spectra of Fig. 4.4, and from the analysis the values of  $C_{mono}$ ,  $C_{dim}$  and  $C_T$  were obtained.

The Fig. 4.6 results show that within the range of the typical assay conditions  $C_{dim}$  remains low and very nearly constant over the time monitored, which justifies use of the typical single-wavelength assay providing that it is performed using this narrow range of conditions. However, a multi-wavelength analysis will allow ccNiR-catalyzed reduction of nitrite by reduced methyl viologen to be meaningfully investigated over a much wider range of  $C_T$ .

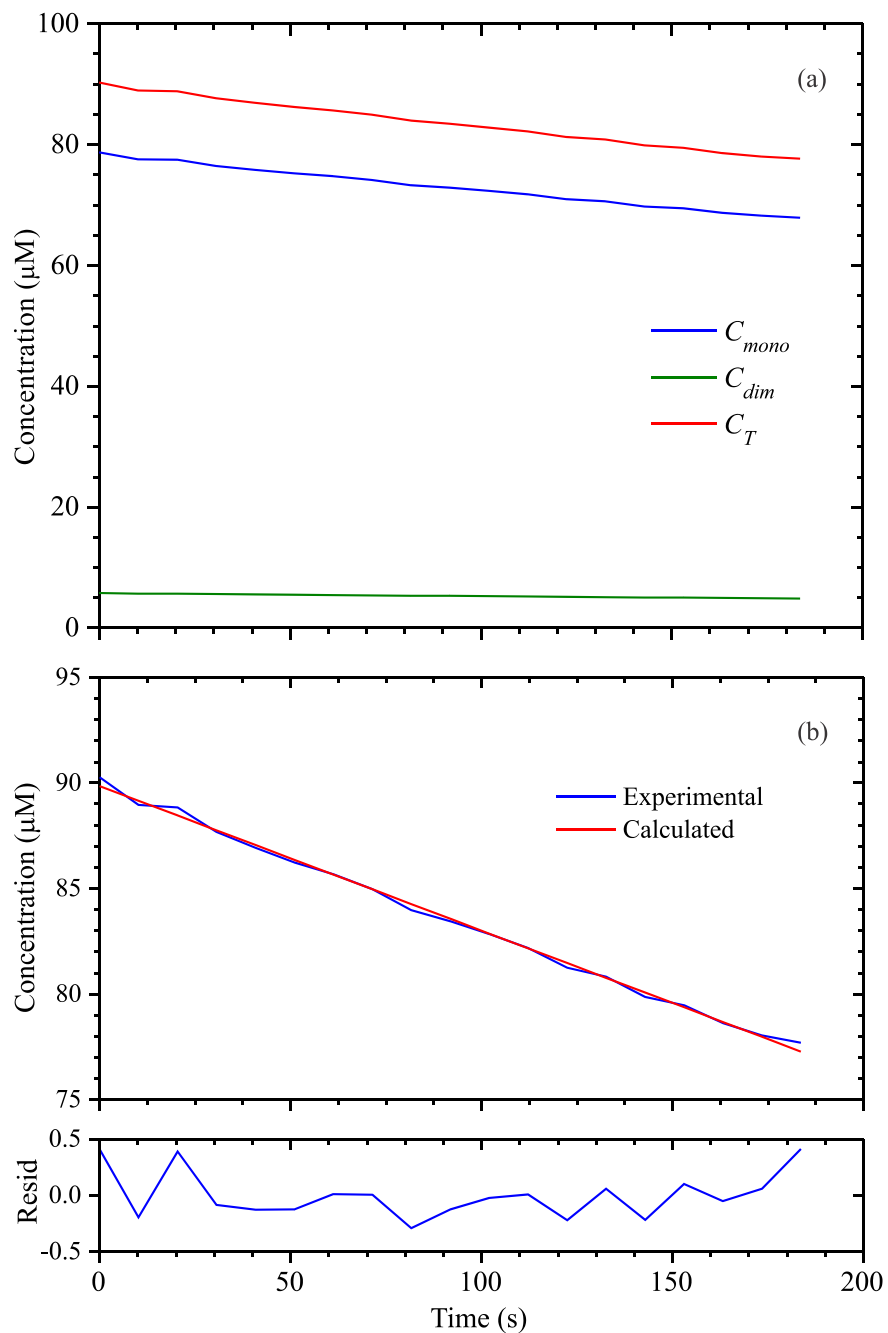


**Figure 4.6.** (a) Typical results of a ccNiR assay analyzed using the extinction coefficient spectra of Fig. 4.4. The spectral changes with time were monitored in the range from 540 nm to 700 nm as reduced methyl viologen reacted with nitrite; the calculated values of  $C_{mono}$ ,  $C_{dim}$  and  $C_T$  are shown. (b) Linear least-squares fit of the  $C_T$  vs time curve.

Preliminary experiments show that ccNiR-catalyzed reduction of nitrite by reduced methyl viologen exhibits first-order dependence on  $C_T$  in the  $C_T$  range from 0 – 100  $\mu\text{M}$  (data not shown). In future the Pacheco group would like to investigate whether the reaction rate exhibits saturation behavior at sufficiently high  $C_T$ , which would conceivably allow catalytic intermediates to accumulate even when using  $\text{MV}_{\text{red}}$  as the electron donor. For such experiments it will be essential to independently monitor  $C_{\text{mono}}$ , and  $C_{\text{dim}}$  as well as  $C_T$ , as the reaction rates might well show different dependencies on each parameter.

## 4.5. References

- [1] Watanabe, T., and Honda, K. (1982) Measurement of the extinction coefficient of the methyl viologen cation radical and the efficiency of its formation by semiconductor photocatalysis, *J. Phys. Chem.* 86, 2617-2619.
- [2] Bird, C. L., and Kuhn, A. T. (1981) Electrochemistry of the viologens, *Chem. Soc. Rev.* 10, 49-82.
- [3] Kosower, E. M., and Cotter, J. L. (1964) Stable free radicals. II. The reduction of 1-methyl-4-cyanopyridinium ion to methylviologen cation radical, *J. Am. Chem. Soc.* 86, 5524-5527.
- [4] Youngblut, M., Judd, E. T., Srajer, V., Sayyed, B., Goelzer, T., Elliott, S. J., Schmidt, M., and Pacheco, A. A. (2012) Laue crystal structure of *Shewanella oneidensis* cytochrome c nitrite reductase from a high-yield expression system, *J. Biol. Inorg. Chem.* 17, 647-662.
- [5] Heineman, W. R., Norris, B. J., and Goelz, J. F. (1975) Measurement of enzyme  $E^0$  values by optically transparent thin layer electrochemical cells, *Anal. Chem.* 47, 79-84.
- [6] Pilkington, M. B. G., Coles, B. A., and Compton, R. G. (1989) Construction of an optically transparent thin layer electrode cell for use with oxygen-sensitive species in aqueous and non-aqueous solvents, *Anal. Chem.* 61, 1787-1789.
- [7] Malinowski, E. R. (1991) *Factor analysis in chemistry*, 2<sup>nd</sup> ed., John Wiley & Sons, Inc.
- [8] Press, W. H., Teukolsky, S. A., Vetterling, W. T., and Flannery, B. P. (2007) *Numerical Recipes the art of scientific computing*, 3rd ed., pp 773-839, Cambridge University Press, New York, NY.
- [9] Press, W. H., Teukolsky, S. A., Vetterling, W. T., and Flannery, B. P. (2007) *Numerical Recipes the art of scientific computing*, 3rd ed., pp 65-75, Cambridge University Press, New York, NY.
- [10] Henry, E. R., and Hofrichter, J. (1992) Singular Value Decomposition: Application to Analysis of Experimental Data, In *Meth. Enzymol.* (Brand, L., and Johnson, M. L., Eds.), pp 129-192, Academic Press, San Diego.

## Appendix A

### Supplementary materials for chapter 2

#### A.1. Verification of ccNiR purity by SDS-PAGE

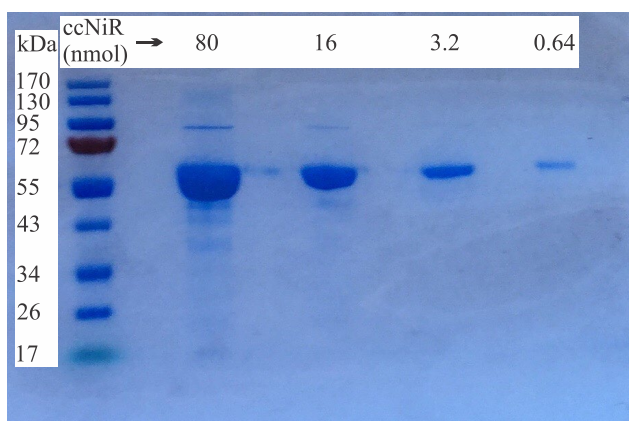


**Figure A.1.** Typical SDS-PAGE for pure ccNiR samples used in the experiments described herein.

#### A.2. Mediators used for spectropotentiometric experiments

**Table A.1.** Mediators used for spectropotentiometry

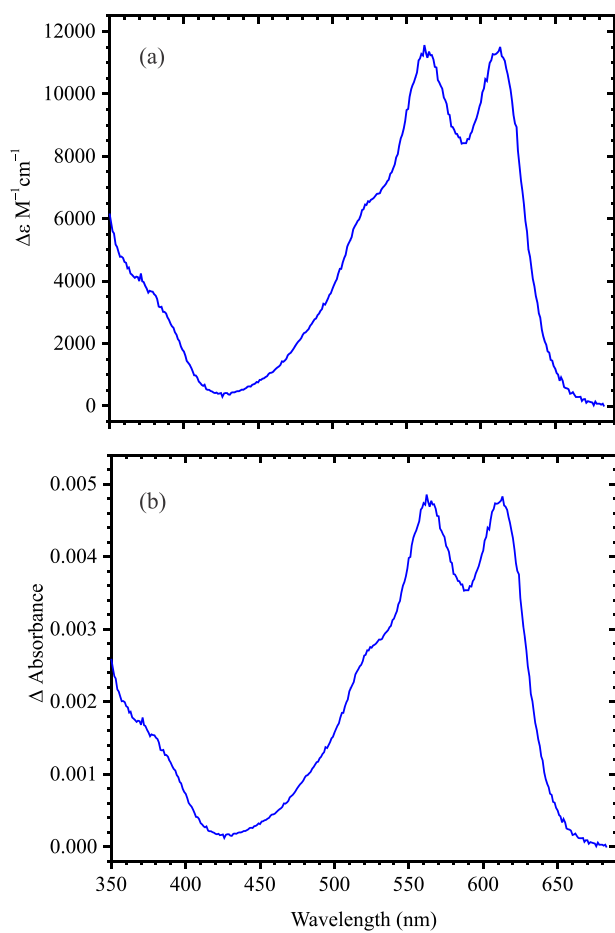
Mediator	$\epsilon_{0.5}$ (V vs SHE)	Used for	Concentration ( $\mu\text{M}$ )
<i>N,N,N',N'</i> -tetramethyl- <i>p</i> -phenylenediamine	0.26 <sup>a,b</sup>	UV/Vis	25
1,2-naphthoquinone-4-sulfonic acid	0.168 <sup>a</sup>	UV/Vis, EPR	100
Phenazine methosulfate	0.08 <sup>b</sup>	UV/Vis	25
Hexaammineruthenium(III) chloride	-0.02 <sup>a</sup>	UV/Vis	100

<sup>a</sup> These midpoint potentials were obtained or verified in-house, at pH 7, using UV/Vis spectropotentiometry or cyclic voltammetry

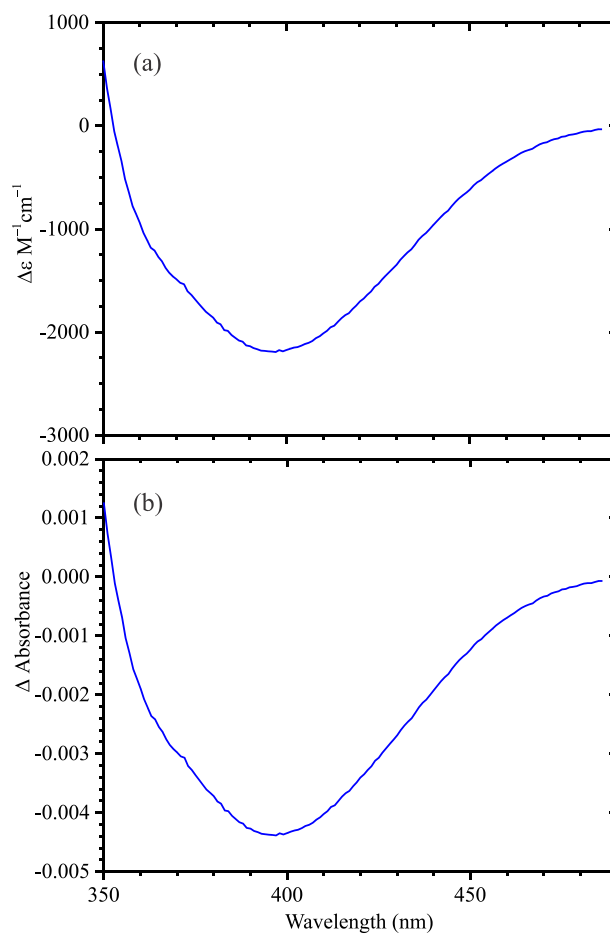
<sup>b</sup> Obtained from ref. 1

Table A.1. lists all of the mediators that were used to investigate the electrochemical properties of nitrite-loaded ccNiR. In practice most of these were used only in preliminary studies, when we had yet to determine even the approximate value of the  $Fe_{H1}^{III}(NO_2^-)$  midpoint potential. Once the midpoint potential range was established, the mediator soup was trimmed to two components: *N,N,N',N'*-tetramethyl-*p*-phenylenediamine (TMPD) and 1,2-naphthoquinone-4-sulfonic acid. For all the experiments reported in the main body of the paper the soup was further trimmed to the single mediator 1,2-naphthoquinone-4-sulfonic acid. This didn't significantly affect the measured midpoint potential, and was convenient because at 100  $\mu\text{M}$  in a 0.02 cm path cell 1,2-naphthoquinone-4-sulfonic acid reduction is

accompanied by very small absorbance changes above 350 nm. Figure A.3. shows the extinction coefficient difference spectrum associated with 1,2-naphthoquinone-4-sulfonic acid reduction (Fig. A.3.a), and the absorbance change expected upon reduction of 100  $\mu\text{M}$  of the mediator (Fig. A.3.b). The difference spectrum has no sharp features, and the biggest change (at 400 nm) is less than 5 mAU. Spectral changes associated with TMPD oxidation were also small (about 5 mAU at both 563 nm and 612 nm, Fig. A.2.), but the  $\text{TMPD}^+$  spectral features are a lot sharper and more distinct. Consequently the  $\text{TMPD}^+$  spectral contribution, though minor, was typically subtracted at each applied potential (reduced TMPD itself doesn't absorb in the visible range). Similarly the spectral contributions from phenazine methosulfate, which were substantially higher than those of either  $\text{TMPD}^+$  or 1,2-naphthoquinone-4-sulfonic acid, and also displayed a sharp feature in the Soret region (Fig. A.4.), were always subtracted at each applied potential. Neither oxidized nor reduced hexaamineruthenium chloride absorb appreciably above 350 nm.



**Figure A.2.** (a) Extinction coefficient difference spectrum for reduced – oxidized *N,N,N',N'*-tetramethyl-*p*-phenylenediamine ( $\Delta$ TMPD; only the oxidized form absorbs in the region from 350 nm – 800 nm) . (b) Spectral contribution expected from 25  $\mu$ M  $\Delta$ TMPD, contained in a 0.02 cm pathlength cuvette.



**Figure A.3.** (a) Extinction coefficient difference spectrum for reduced – oxidized 1,2-naphthoquinone – 2-sulfonic acid ( $\Delta$ NPSA; only the oxidized form absorbs in the region from 350 nm – 500 nm, neither form absorbs above 500 nm). (b) Spectral contribution expected from 100  $\mu$ M  $\Delta$ NPSA, contained in a 0.02 cm pathlength cuvette.

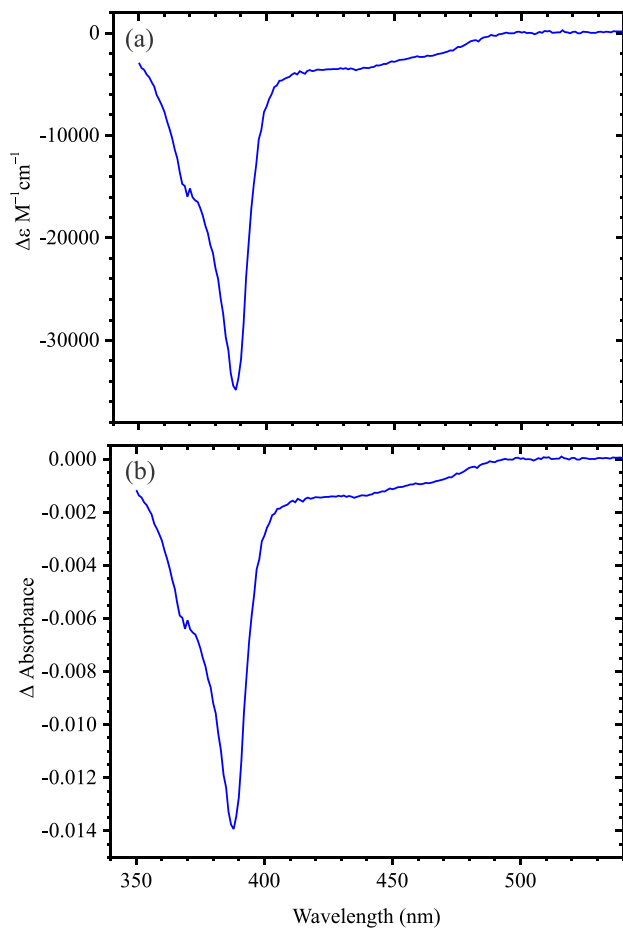
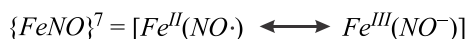
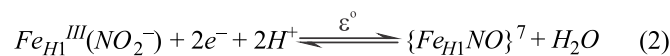
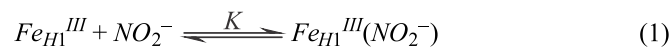


**Figure A.4.** (a) Extinction coefficient difference spectrum for reduced – oxidized Phenazine methosulfate ( $\Delta$ PMS; only the oxidized form absorbs in the region from 350 nm – 500 nm, and neither form absorbs above 500 nm). (b) Spectral contribution expected from 25  $\mu\text{M}$   $\Delta$ PMS, contained in a 0.02 cm pathlength cuvette.

### A.3. Equilibrium expression for nitrite binding to the ccNiR active site

The first step in Scheme A1 describes the binding of nitrite to the ferriheme ccNiR active site ( $Fe_{H1}^{III}$ ), and is governed by the binding constant  $K$ , as shown in Eq. A1. This is the topic of this Section. The relationship between nitrite binding and subsequent reduction of  $Fe_{H1}^{III}(NO_2^-)$  will be discussed in Section A.4.



**Scheme A1.** Equilibrium for nitrite binding with ccNiR

$$K = \frac{[Fe_{H1}^{III}(NO_2^-)]}{[Fe_{H1}^{III}][NO_2^-]} \quad A1$$

During a titration of ccNiR by nitrite we will define the total ccNiR concentration as  $Fe_T$ , and the total nitrite concentration at any given titration step as  $N_T$ . Thus, at any given titration step, the distributions of ccNiR and nitrogenous species in solution are given by Eqs. A2 and A3, respectively.

$$Fe_T = [Fe_{H1}^{III}] + [Fe_{H1}^{III}(NO_2^-)] \quad A2$$

$$N_T = [NO_2^-] + [Fe_{H1}^{III}(NO_2^-)] \quad A3$$

Solving Eqs A2 and A3 for  $[Fe_{H1}^{III}]$  and  $[NO_2^-]$ , respectively, and substituting into Eq. A1, yields expression A4. This in turn can be solved for  $[Fe_{H1}^{III}(NO_2^-)]$  to give Eq. A5.

$$K = \frac{[Fe_{H1}^{III}(NO_2^-)]}{\{Fe_T - [Fe_{H1}^{III}(NO_2^-)]\} \{N_T - [Fe_{H1}^{III}(NO_2^-)]\}} \quad A4$$

$$[Fe_{H1}^{III}(NO_2^-)] = \frac{(Fe_T + N_T) \cdot K + 1 - \sqrt{Fe_T^2 \cdot K^2 \cdot N_T + 2Fe_T \cdot K + K^2 \cdot N_T^2 + 2K \cdot N_T + 1}}{2K} \quad A5$$

#### A.4. Dependence of nitrite-loaded ccNiR's electrochemical behavior on pH and nitrite concentration

Equation A6 is the Nernst equation associated with reaction (2) of Scheme A1. In Eq. A6  $\varepsilon_{app}$  is the potential applied during the spectropotentiometric experiment, and  $\varepsilon^o$  is the standard reduction

$$\varepsilon_{app} = \varepsilon^o - \frac{RT}{2F} \ln \frac{\{Fe_{H1}NO\}^7}{[Fe_{H1}^{III}(NO_2^-)][H^+]^2} \quad A6$$

potential. In a buffered solution Eq. A6 can be rearranged to the form A7, which defines the apparent midpoint potentials  $\varepsilon_{pH}^o$  that will be obtained in spectropotentiometric experiments at varying pHs.

$$\varepsilon_{app} = \varepsilon_{pH}^o - \frac{RT}{2F} \ln \frac{\{Fe_{H1}NO\}^7}{[Fe_{H1}^{III}(NO_2^-)]} \quad A7$$

where

$$\varepsilon_{pH}^o = \varepsilon^o - \frac{2.303RT}{F} pH$$

Equation A7 is readily rearranged to the exponential form A8, which is more appropriate for fitting results from experiments in which  $\varepsilon_{app}$  is the independent variable.

$$\frac{\{Fe_{H1}NO\}^7}{[Fe_{H1}^{III}(NO_2^-)]} = \exp \left[ \frac{2F}{RT} (\varepsilon_{pH}^o - \varepsilon_{app}) \right] \quad A8$$

When the nitrite concentration is high, equilibrium 1 in Scheme A1 will lie far to the right, so the concentration of ccNiR without nitrite in the active site ( $[Fe_{H1}^{III}]$ ) will be negligible. The exponential Nernst equation can then be written as Eq. A9.

$$\{Fe_{H1}NO\}^7 = \frac{Fe_T \cdot \exp \left[ \frac{2F}{RT} (\varepsilon_{pH}^o - \varepsilon_{app}) \right]}{1 + \exp \left[ \frac{2F}{RT} (\varepsilon_{pH}^o - \varepsilon_{app}) \right]} \quad A9$$

where

$$Fe_T = [Fe_{H1}^{III}(NO_2^-)] + \{Fe_{H1}NO\}^7$$

In our UV/Vis spectropotentiometric experiments we monitored spectral changes as a function of the applied potential. To relate the Nernst equation with spectral changes at a given applied potential  $\varepsilon_{app}$  we use Beer's law (Eq. A10), in which  $\epsilon_{1\lambda}$  and  $\epsilon_{2\lambda}$  are the extinction coefficients of  $[Fe_{H1}^{III}(NO_2^-)]$  and

$$A_{\lambda, \varepsilon_{app}} = \left( \epsilon_{1\lambda} [Fe_{H1}^{III}(NO_2^-)]_{\varepsilon_{app}} + \epsilon_{2\lambda} \{Fe_{H1}NO\}_{\varepsilon_{app}}^7 \right) \cdot l \quad A10$$

$\{Fe_{H1}NO\}^7$ , respectively, at wavelength  $\lambda$ . For difference spectra Eq. A910 can be recast in the form A11, where  $\Delta\epsilon_{\lambda} = \epsilon_{2\lambda} - \epsilon_{1\lambda}$ , and  $\Delta A_{\lambda, \varepsilon_{app}} = A_{\lambda, \varepsilon_{app}} - A_{\lambda, \varepsilon_{app}^o}$ ;  $A_{\lambda, \varepsilon_{app}^o}$  is the absorbance of the fully oxidized

ccNiR (obtained in the absence of an applied potential). Finally, Eqs. A9 and A11 can be combined to give, after some rearrangement, Eq. A12.

$$\{Fe_{H1}NO\}_{\varepsilon_{app}}^7 = \frac{\Delta A_{\lambda, \varepsilon_{app}}}{\Delta \varepsilon_{\lambda} \cdot l} \quad A11$$

$$\Delta A_{\lambda, \varepsilon_{app}} = \frac{Fe_T \cdot \Delta \varepsilon_{\lambda} \cdot l \cdot \exp\left[\frac{2F}{RT}(\varepsilon_{pH}^o - \varepsilon_{app})\right]}{1 + \exp\left[\frac{2F}{RT}(\varepsilon_{pH}^o - \varepsilon_{app})\right]} \quad A12$$

Equation A12 is identical in form to Eq. 2.1 from the main text, and at limiting nitrite concentrations the empirical parameter  $\varepsilon_m^o$  of Eq. 2.1 can be interpreted to be  $\varepsilon_{pH}^o$  as defined in Eq. A7. Also,  $\Delta A_{max(\lambda)}$  of Eq. 2.1 will correspond with the product  $Fe_T \cdot \Delta \varepsilon_{\lambda} \cdot l$  of Eq. A12. Since the pathlength and total ccNiR concentration  $Fe_T$  were known for all experiments, an extinction coefficient difference spectrum corresponding to reduction of the oxidized protein to the 2-electron reduced  $\{Fe_{H1}NO\}^7$  form was obtained from experiments carried out in the presence of high nitrite concentrations (Fig. A.5.). This difference spectrum could then be used to determine the extent of ccNiR reduction under conditions when full reduction was not necessarily achieved (see below and main text). Finally, the extinction coefficient difference spectrum of Fig. A.5., together with the independently obtained extinction coefficient spectrum of fully oxidized ccNiR, could be used to obtain the absolute spectrum of  $\{Fe_{H1}NO\}^7$  ccNiR. This spectrum is shown in Fig. A.6.; the spectrum of the oxidized species is shown for comparison. The  $\{Fe_{H1}NO\}^7$  ccNiR extinction coefficient spectrum was used to fit the data.

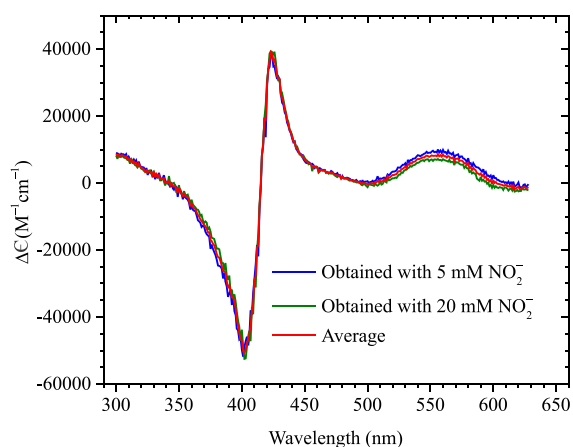


**Figure A.5.** Extinction coefficient difference spectra obtained by fitting data collected in the presence of 5 mM (blue trace) and 20 mM (green trace) to Eq. A12. The red trace is the average of the other two, and was used to determine the extent of ccNiR reduction in experiments where this was not known a priori.

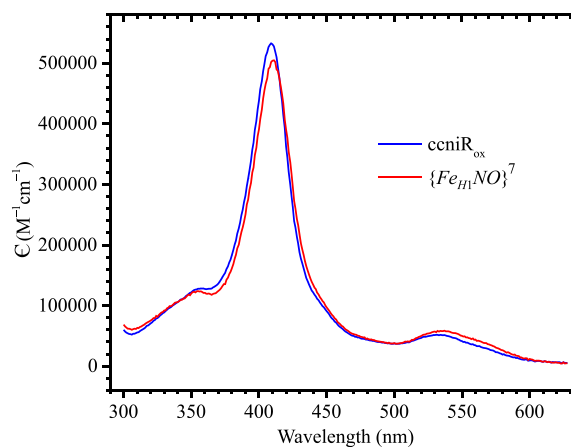


**Figure A.6.** Red trace: extinction coefficient spectrum of  $\{Fe_{H1}NO\}^7$  ccNiR. Blue trace: spectrum of fully oxidized ccNiR.

Equation 2.1 from the main text, an empirical Nernst equation in exponential form, was found to effectively model spectropotentiometric data sets collected for ccNiR in the presence of nitrite concentrations ranging from 20 mM, all the way down to 30  $\mu$ M, which was sub-stoichiometric compared to the ccNiR concentration. However, the empirical parameter  $\varepsilon_m^o$  of Eq. 2.1 can only be correlated with  $\varepsilon_{pH}^o$  as defined in Eq. A7 under conditions in which ccNiR was saturated with nitrite. At lower nitrite concentrations Equilibrium (1) of Scheme A1 must be accounted for, as will be described next.

When ccNiR can exist in both nitrite-loaded and nitrite-free forms, the total ccNiR concentration will be given by Eq. A13. Equation A8 is still valid under these conditions, and it can be combined with Eq. A13 to eliminate the reduced species from the expression. This gives Eq. A14. At sufficiently low nitrite concentrations we also need to consider that an appreciable fraction of the nitrite added to the

$$Fe_T = [Fe_{H1}^{III}] + [Fe_{H1}^{III}(NO_2^-)] + \{Fe_{H1}NO\}^7 \quad A13$$

$$Fe_T = [Fe_{H1}^{III}] + [Fe_{H1}^{III}(NO_2^-)](1 + E1) \quad A14$$

where

$$E1 = \exp\left[\frac{2F}{RT}(\varepsilon_{pH}^o - \varepsilon_{app})\right]$$

solution will end up bound to ccNiR. With this in mind we define  $N_T$  as the total concentration of nitrite that is initially added to the reaction mixture. Thus, at any given moment, the distribution of nitrogenous species will be given by Eq. A15. As with the expression for  $Fe_T$  above, Eqs. A15 and A8 can be combined to eliminate  $\{Fe_{H1}NO\}^7$  from the expression (Eq. A16).

$$N_T = [NO_2^-] + [Fe_{H1}^{III}(NO_2^-)] + \{Fe_{H1}NO\}^7 \quad A15$$

$$N_T = [NO_2^-] + [Fe_{H1}^{III}(NO_2^-)](1 + E1) \quad A16$$

Combining Eqs. A1, A14 and A16 gives equilibrium expression A17, in which the variable at a given  $\varepsilon_{app}$  is  $[Fe_{H1}^{III}(NO_2^-)]$ . Equation A17 is a quadratic, and can be solved for  $[Fe_{H1}^{III}(NO_2^-)]$  (Eq. A18).

$$K = \frac{[Fe_{H1}^{III}(NO_2^-)]}{\{Fe_T - [Fe_{H1}^{III}(NO_2^-)] \cdot (1 + E1)\} \{N_T - [Fe_{H1}^{III}(NO_2^-)] \cdot (1 + E1)\}} \quad A17$$

$$[Fe_{H1}^{III}(NO_2^-)] = \frac{Fe_T \cdot K(1 + E1) - \sqrt{Fe_T^2 \cdot K^2(1 + E1)^2 - 2Fe_T \cdot K^2 \cdot N_T(1 + E1)^2 + 2Fe_T \cdot K(1 + E1) + K^2 \cdot N_T^2(1 + E1)^2 + 2K \cdot N_T(1 + E1) + K \cdot N_T(1 + E1) + 1}}{2K(1 + E1)^2}$$

A18

Once  $[Fe_{H1}^{III}(NO_2^-)]$  has been obtained from Eq. A18, the corresponding concentration of  $\{Fe_{H1}NO\}^7$  can be obtained straightforwardly with Eq. A19.

$$\{Fe_{H1}NO\}^7 = [Fe_{H1}^{III}(NO_2^-)] \cdot E1$$

A19

In Eq. A18 the independent variable is the applied potential  $\varepsilon_{app}$  incorporated in  $E1$  (Eq. A14). To use the equation  $\varepsilon_{pH}^o$  (hidden in  $E1$ ) was fixed at 0.246 V, the value obtained from spectropotentiometric titrations at pH 7 and saturating concentrations of nitrite (5 mM or higher), and the exact value of  $Fe_T$  was determined in each experiment from the UV/Vis spectrum of the fully oxidized ccNiR prior to applying any potential.  $K$  was treated as an adjustable parameter, as described in the main text. For each trial  $K$

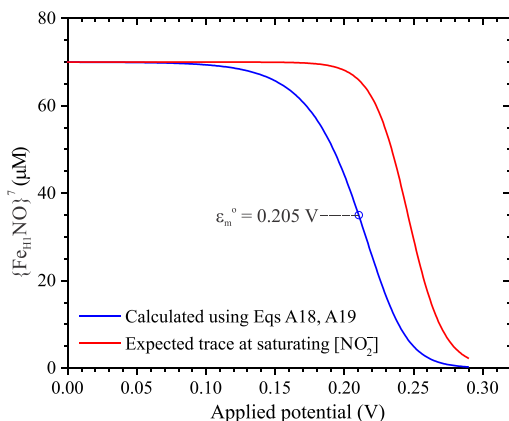


**Figure A.7.** Blue trace: plot of  $\{Fe_{H1}NO\}^7$  vs  $\varepsilon_{app}$  calculated using Eqs A18 and A19, when  $Fe_T$  and  $N_T$  are both 70  $\mu\text{M}$ . The midpoint potential is taken as the value of  $\varepsilon_{app}$  at which 50% of  $Fe_T$  has been reduced. Red trace: plot obtained with  $N_T = 5$  mM, when virtually all ccNiR is nitrite-loaded.

value Eqs. A18 and A19 were used to generate  $[Fe_{H1}^{III}(NO_2^-)]$  and  $\{Fe_{H1}NO\}^7$  vs.  $\varepsilon_{app}$  traces for the set of  $N_T$  values in Fig. 2.2 of the main text. The  $\varepsilon_m^o$  value at each  $N_T$  was then calculated as the value of  $\varepsilon_{app}$  at which  $\{Fe_{H1}NO\}^7 = 0.5Fe_T$ . Finally, the set of  $\varepsilon_m^o$  values obtained with Eqs. A18 and A19 were compared in a least-squares sense with those obtained using the empirical Eq. 2.1 from the main text, and  $K$  was adjusted to minimize the least-squares.

Figure A7 gives an example of a  $\{Fe_{H1}NO\}^7$  vs  $\varepsilon_{app}$  trace generated with  $Fe_T = N_T = 70$   $\mu\text{M}$ ; the trace that would be expected at saturating nitrite concentrations is also provided for comparison. The midpoint potential for the  $\{Fe_{H1}NO\}^7$  vs  $\varepsilon_{app}$  trace is the point at which half the  $Fe_T$  (35  $\mu\text{M}$ ) has been reduced to  $\{Fe_{H1}NO\}^7$ ; these are the calculated  $\varepsilon_m^o$  values plotted in Fig. 2.2 of the main text. Though the shapes of the plots obtained with Eqs A18, A19 at low  $N_T$  are not quite the same as the shapes generated by the empirical Nernst

equation (Eq. 2.1, main text), the midpoint potentials obtained by fitting low  $N_T$  experimental data with the empirical equation tracked the ones calculated with Eqs A18 and A19 reasonably well (Fig. 2.2, main text).

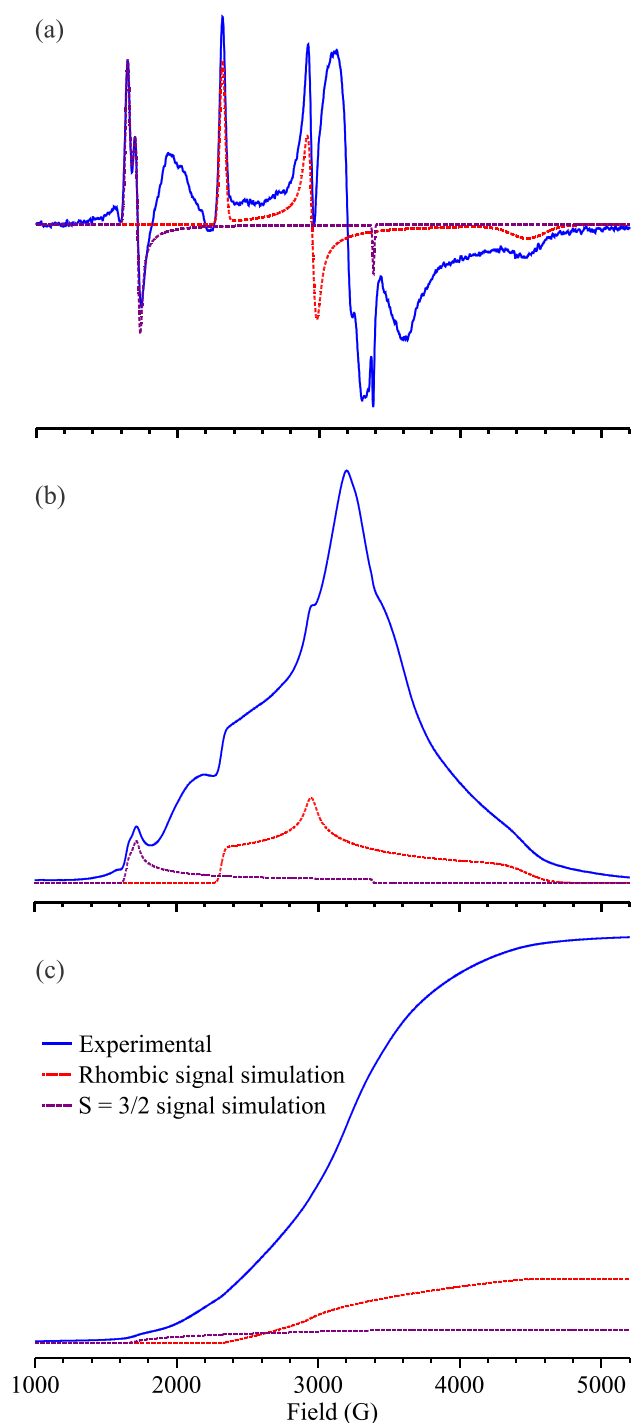


**Figure A.8.** (a) Solid blue trace: X-band EPR spectrum of the nitrite-loaded ccNiR solution from Fig. 8 after reduction at  $\varepsilon_{app} = 160$  mV vs SHE; dashed red trace: simulated spectrum of the rhombic signal arising from ccNiR heme 2; purple trace: simulation of the  $S = 3/2 \{FeNO\}^7$  signal. (b) Integration of the signals from (a). (c) Double integration.

### A.5. Spin quantitation of the nitrite-loaded ccNiR EPR spectrum after reduction

The blue trace in Figure A.8.a shows the X-band EPR spectrum obtained for the solution from Fig. 2.5 of the main paper that initially contained  $64 \mu\text{M}$  of fully oxidized ccNiR and  $500 \mu\text{M}$   $^{14}\text{NO}_2^-$ , after it was exposed to an applied potential of 160 mV vs SHE. The red dashed trace is a simulation of the rhombic signal previously assigned to ccNiR heme 2, while the purple dashed trace is a simulation of the  $S = 3/2 \{FeNO\}^7$  signal that appears as ccNiR is reduced. Figures A.8.b and A.8.c show the integrals and double integrals, respectively, of the Fig. A.8.a traces. The integrations show that the  $S = 3/2 \{FeNO\}^7$  signal has about 20% of heme 2's intensity. For the  $64 \mu\text{M}$  ccNiR solution this would put the concentration of  $S = 3/2 \{FeNO\}^7$  at  $\sim 13 \mu\text{M}$ . The heme 2 signal in turn accounts for about 16% of the total spin envelope.

## A.6. Quantitation of adventitious iron in the EPR spectra

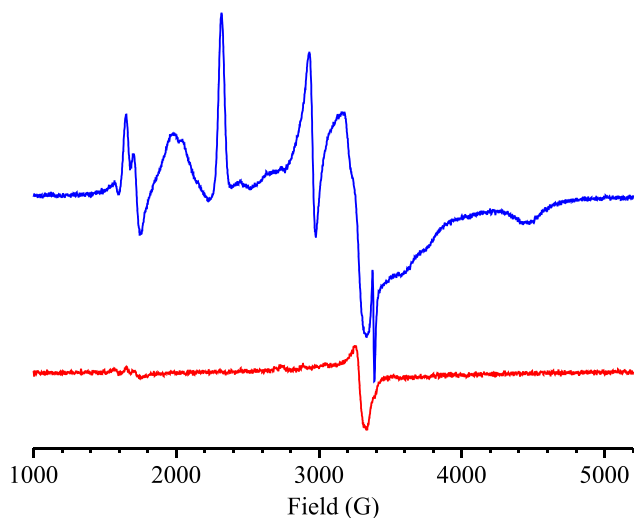


**Figure A.9.** Blue trace: X-band EPR spectrum of the nitrite-loaded ccNiR solution from Fig. 8 after reduction at  $\epsilon_{app} = 160$  mV vs SHE; Red trace: filtrate from ultrafiltration of a solution that initially contained the same species as those of Fig. 8, plus  $25 \mu\text{M } \text{Cu}^{2+}$ , after adding approximately  $60 \mu\text{M } \text{NO}^-$ , and subjecting it to an applied potential of 160 mV vs SHE.

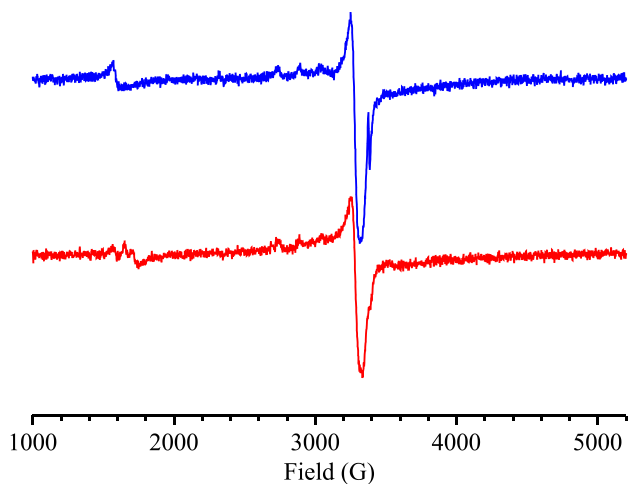


**Figure A.10.** Blue trace: filtrate from ultrafiltration of a solution that initially contained the same components as those of Fig. 8, plus  $25 \mu\text{M } \text{Cu}^{2+}$ , after adding approximately  $60 \mu\text{M } \text{NO}^-$ , but before subjecting to a reducing potential. Red trace: same as red trace in Fig. A.9.

The blue trace in Figure A.9. shows the same EPR spectrum of reduced ccNiR as Fig. A.8. and Fig. 2.5. from the main text. The red trace shows a spectrum for the filtrate from ultrafiltration of a solution that initially contained the same species as those that engendered the blue trace, plus  $25 \mu\text{M } \text{Cu}^{2+}$  and  $60 \mu\text{M } \text{NO}^-$ , and that was then subjected to an applied potential of 160 mV vs SHE. Spin quantitation of the red trace signals showed that the  $S = 3/2 \{FeNO\}^7$  signal's intensity was 0.75% that of the  $\text{Cu}^{2+}$ , which would amount to  $\sim 0.2 \mu\text{M } \{FeNO\}^7$ . For comparison, from the integration shown in Fig. A.8. we estimated that the  $S = 3/2 \{FeNO\}^7$  signal was  $\sim 20\%$  of heme 2 in a  $64 \mu\text{M}$  ccNiR solution, which would come to  $\sim 13 \mu\text{M } \{FeNO\}^7$ .

Figure A.10. compares the filtrate from ultrafiltration of the solution described for Fig. A.9., before (blue trace) and after (red trace) subjecting it to the applied potential of 160 mV vs SHE. The rhombic ferric iron signal's intensity was found to be about 0.65% that of  $\text{Cu}^{2+}$  in the oxidized spectrum, which would amount to  $\sim 0.16 \mu\text{M}$  rhombic ferric iron, comparable to the concentration of  $S = 3/2 \{FeNO\}^7$  present after reduction (red trace); no  $S = 3/2$  signal was detectable in the filtrate prior to electrochemical reduction.

## A.7. Absorbance changes upon reduction of nitrite-loaded ccNiR

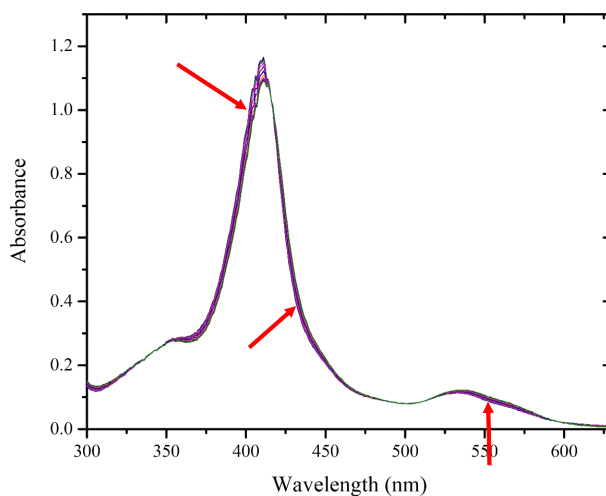


**Figure A.11.** UV/Vis spectra obtained upon exposing a solution initially containing 76  $\mu\text{M}$  of fully oxidized ccNiR, 100  $\mu\text{M}$  1,2-naphthoquinone-4-sulfonic acid and 5 mM nitrite to progressively lower potentials.

Figure A.11. shows the full spectra associated with reduction of nitrite-loaded ccNiR. Initially a spectrum of fully oxidized solution of 76  $\mu\text{M}$  ccNiR, 100  $\mu\text{M}$  1,2-naphthoquinone-4-sulfonic acid and 5 mM nitrite was obtained. Then spectropotentiometric studies was performed from 300 mV vs SHE to 160 mV vs SHE with 10 mV increment. Maximum changes were observed at 402, 432 and 550 nm that indicate the typical *c* heme reduction.

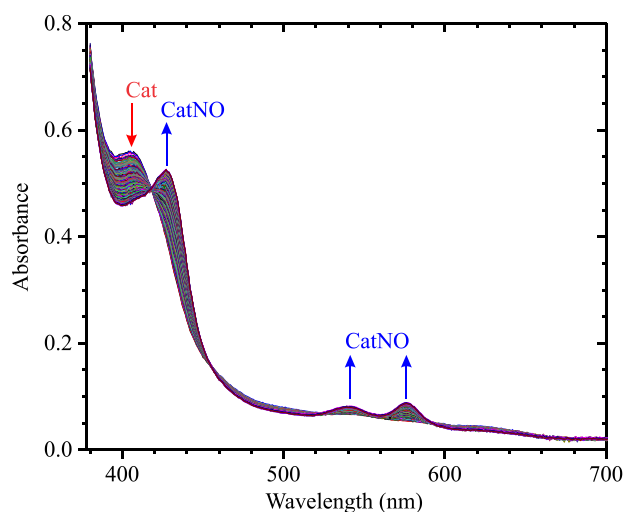
## A.8. References

- (1) Fultz, M. L.; Durst, R. A. Mediator compounds for the electrochemical study of biological redox systems: a compilation *Anal. Chim. Acta* **1982**, *140*, 1-18.

## Appendix B

### Supplementary materials for chapter 3

#### B.1. Absorbance changes upon releasing of nitric oxide (NO $\cdot$ ) from the reduction of nitrite.



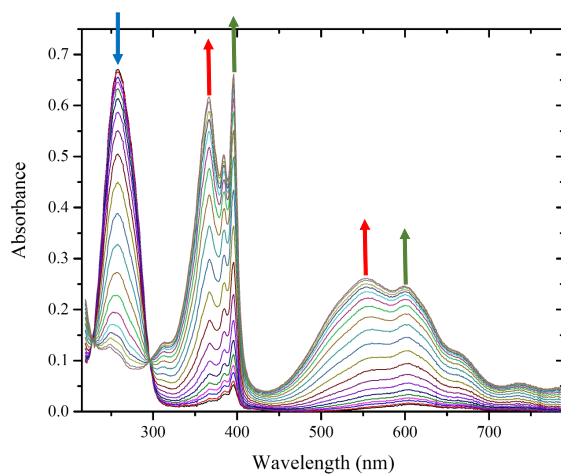
**Figure B.1.** UV/Vis spectral changes obtained from NO $\cdot$  binding with catalase. A solution containing 75 nM ccNiR, 20 mM ferrocyanide, 2 mM nitrite and 4  $\mu$ M catalase at pH 7.0 was taken to run the steady state reaction for 1 hour. ccNiR catalyzed the reduction of nitrite by 1-electron to NO $\cdot$  by the weak reducing agent ferrocyanide.

Figure B.1. shows the spectral change for steady state reaction at the condition of 75 nM ccNiR, 20 mM ferrocyanide, 2 mM nitrite and 4  $\mu$ M catalase at pH 7.0. Initially at time zero, the spectrum of total 4  $\mu$ M of catalase was observed. As the reduction proceeds, NO $\cdot$  generated by the reduction of nitrite binds with catalase and gives characteristic NO-bound catalase (CatNO) spectra. Therefore a decrease of absorbance of catalase at 402 nm and increase of absorbance of CatNO were observed.

## Appendix C

### Supplementary materials for chapter 4

#### C.1. UV/Vis spectropotentiometric studies of methyl viologen (MV) monomer-dimer equilibrium.



**Figure C.1.** The spectral change obtained when  $MV_{ox}$  was reduced to  $MV_{red}$  by applying progressively lower potential

## Curriculum Vitae of Mahbbat Ali

### EDUCATION

---

***Doctor of Philosophy (Ph.D.) in Chemistry (Bioinorganic enzymology)*** **2019**  
University of Wisconsin-Milwaukee, Milwaukee, Wisconsin

*Dissertation:* Probing the early steps in the catalytic reduction of nitrite to ammonia, catalyzed by Cytochrome *c* nitrite reductase.

*Advisor:* Professor A. Andrew Pacheco

***Masters of Science (M.S.) in Chemistry (Physical/Analytical)*** **2010**  
University of Dhaka, Bangladesh

*Thesis:* Decolorization of wastewater by continuous column adsorption using low cost adsorbent.

*Advisor:* Professor Tajmeri S. A. Islam, Ph.D.

***Bachelor of Science (B.S.) in Chemistry*** **2009**  
University of Dhaka, Bangladesh

*Research Project:* Comparative study of the adsorption of methylene blue on low cost adsorbent by column process.

*Advisor:* Professor Tajmeri S. A. Islam, Ph.D.

### RESEARCH EXPERIENCE

---

#### PhD Graduate research

*University of Wisconsin-Milwaukee*

*January 2014-Present*

#### **1. Trapping putative intermediates in nitrite reduction to ammonia catalyzed by ccNiR**

- Designed and executed extensive UV-Vis and EPR spectropotentiometric experiments to characterize cytochrome *c* nitrite reductase (ccNiR), and to trap putative intermediates of ccNiR-catalyzed nitrite reduction.
- Investigated ccNiR-catalyzed nitrite reduction by weak reducing agents such as ferrocyanide, hexaammineruthenium(II) and *N,N,N',N'*-tetramethyl-*p*-phenylenediamine (TMPD) using time-resolved UV-Vis spectroscopy

## **2. Steady state kinetics analysis of one electron reduction of nitrite to nitric oxide catalyzed by ccNiR**

- Carried out stopped-flow experiments to understand the pre-steady-state kinetics in the mechanism of ccNiR-catalyzed nitrite reduction
- Performed time resolved UV-Vis spectroscopy to understand the steady-state kinetics of reduction of nitrite under mild reducing environment.

## **3. Microbial bacteria culture, protein expression and purification**

- Improved the protocol for culturing *Shewanella oneidensis* on a 50 L scale, and for purifying ccNiR from these large-scale cultures.
- Grew macro crystals of ccNiR using the hanging drop method and micro crystals using vortex method.

## **M.S. Graduate research**

*University of Dhaka, Bangladesh*

*July2008-January 2010*

### **1. Investigation of adsorption capability of low-cost adsorbent**

- Designed and prepared a continuous column method to characterize methylene blue (MB) in wastewater.

### **2. Construction of a low-cost chromatographic column**

- Gained hands-on experience preparing low-cost chromatographic columns and flow meters.

## **SKILLS**

---

### **Specialized instrumental proficiencies**

- HPLC, FPLC instrumentation
- UV-Vis and EPR-spectropotentiometry for characterizing redox-active enzymes
- LASER-initiated time-resolved UV-Vis spectroscopy for monitoring fast reactions
- Stopped-flow time-resolved UV-Vis spectroscopy for monitoring fast reactions
- Use of oxygen-free gloveboxes for handling air-sensitive enzymes and running reactions under anaerobic conditions
- Use of inert atmosphere manifolds for preparing and handling air-sensitive materials
- Ultra-and high-speed centrifuges
- Vacuum gas manifold

### **General biochemical skills**

- Polymerase chain reaction (PCR)
- Large-scale protein purification using a variety of chromatographic techniques
- Enzyme assay development
- SDS-PAGE
- ccNiR Macro and mirco crystal growing

### **Computation skills**

- Data analysis using Origin, Mathcad 15, and Excel
- Electronic documentation using Lab archive and Electronic notebook
- Chromatography using the Unicorn<sup>TM</sup> 7 software

### **Adaptability and communication**

- Strong ability to work in collaborative research environments.
- Efficient in learning new methods and skills
- Proven record in organizational and leadership skills.

## **TEACHING EXPERIENCE**

---

### *University of Wisconsin – Milwaukee*

**Graduate Teaching Assistant** (September 2013- December 2015 & January 2019 – December 2019)

- Taught undergraduate chemistry courses, including general chemistry (both discussion and laboratory classes) for pre-medical and pre-nursing majors. Graded quizzes, exams and laboratory reports

**Mentoring** (January 2015- December 2018)

- Mentored five undergraduate researchers in the Pacheco laboratory. One of these, Ms. Yingxi Mao, is a co-author on a publication (see below)

## **AWARD AND PRIZES**

---

- Chancellor's graduate fellowship from the department of Chemistry and Biochemistry; UWM; September 2013 to December 2015
- Best poster presentation for the 'Nitrogen Unfixation Symposium' held at 255<sup>th</sup> ACS national meeting and exposition. March, 2018.

## PUBLICATIONS

---

1. **Mahbbat Ali**, et al. “Steady-state investigations of Cytochrome *c* Nitrite Reductase (ccNiR)-catalyzed reduction of nitrite to NO by weak reducing agents”. *J. Biol. Inorg. Chem.* **2020** (anticipated), *Manuscript in preparation*.
2. **Mahbbat Ali**, Natalia Stein, Yingxi Mao, Shahid Shahid, Marius Schmidt, Brian Bennett, A. Andrew Pacheco. “Trapping of a putative intermediate in the *Shewanella oneidensis* cytochrome *c* nitrite reductase (ccNiR) - catalyzed reduction of nitrite: implications for the ccNiR reaction mechanism.” *J. Am. Chem. Soc.* **2019**, 141, 34, 13358-13371.
3. Mohammad A. Hossain, **Mahbbat Ali**, Tajmeri SA Islam. “Comparative Adsorption of Methylene Blue on Different Low Cost Adsorbents by Continuous Column Process”. *Int. Letters of Chem. Ph. And Ast.* **2018**, 77, 26-34.
4. YeakubZaker, Mohammad A. Hossain, **Mahbbat Ali**, and Tajmeri SA Islam. “Characterization of sand fractioned from Bijoypur soil, Bangladesh and its application as an adsorbent”. *Res. J. of Chem. Sci.* **2013**, 3(11), 90-94.

## SELECTED POSTERS

---

1. Mahbbat Ali, Yingxi Mao and A. Andrew Pacheco. “Trapping intermediates in the Cytochrome *c* Nitrite Reductase (ccNiR) catalyzed reduction of nitrite to ammonia”. Midwest Enzyme Chemistry Conference, Illinois Institute of Technology, October 2019.
2. Mahbbat Ali, Natalia Stein, Yingxi Mao and A. Andrew Pacheco. “Probing putative intermediates in the catalytic reduction of nitrite to ammonia, catalyzed by *S. Oneidensis* Cytochrome *c* Nitrite Reductase (ccNiR)”. Gordon Research Seminar (GRS), Bioinorganic Chemistry. January, 2019.
3. Mahbbat Ali, Desiree Legaspi-Humiston, Nick Robinson, Kaleb Keefe, Dan Pauly, and A. Andrew Pacheco. “Cytochrome *c* Nitrite Reductase (ccNiR)-catalyzed reduction of nitrite by weak reducing agent” 2<sup>nd</sup> Medical College of Wisconsin Redox Biology Symposium. April 2018
4. Mahbbat Ali and A. Andrew Pacheco. “A mechanistic view of Cytochrome *c* nitrite reductase (ccNiR) catalyzed reduction of nitrite to nitric oxide- a partial reduction of six electron reduction of nitrite to ammonia” 255<sup>th</sup> ACS National Meeting and Exposition, March 2018.
5. Mahbbat Ali, Natalia Stein, Desiree Legaspi-Humiston, Nick Robinson, Kaleb Keefe, and A. Andrew Pacheco. “Cytochrome *c* Nitrite Reductase (ccNiR)-catalyzed reduction of nitrite by ferrocyanide”. Gordon Research Conference (GRC), Metals in Biology. January, 2018
6. Mahbbat Ali, Natalia Stein, Desiree Legaspi-Humiston, Dan Pauly and A. Andrew Pacheco. “Cytochrome *c* Nitrite Reductase (ccNiR)-catalyzed one electron reduction of Nitrite under mild reducing condition”. Chemistry Department Symposium, UWM, May 2017